12-1995

Design and Fabrication of a Micromechanical Gyroscope

Richard M. Kuhns

DESIGN AND FABRICATION OF A MICROMECHANICAL GYROSCOPE

THESIS

Richard Michael Kuhns
Second Lieutenant, USAF

AFIT/GE/ENG/95D-10

DEPARTMENT OF THE AIR FORCE
AIR UNIVERSITY
AIR FORCE INSTITUTE OF TECHNOLOGY

Wright-Patterson Air Force Base, Ohio

AFIT/GE/ENG/95D-10

DESIGN AND FABRICATION OF A MICROMECHANICAL GYROSCOPE

THESIS

Richard Michael Kuhns
Second Lieutenant, USAF

AFIT/GE/ENG/95D-10

The views expressed in this thesis are those of the author and do not reflect the official policy or position of the Department of Defense or the U. S. Government.

AFIT/GE/ENG/95D-10

DESIGN AND FABRICATION OF A MICROMECHANICAL GYROSCOPE

THESIS

Presented to the Faculty of the School of Engineering

of the Air Force Institute of Technology

Air University

In Partial Fulfillment of the

Requirements for the Degree of

Master of Science in Electrical Engineering

Richard Michael Kuhns, B.S.E.E.

Second Lieutenant, USAF

December, 1995

Table of Contents

List of Figures

List of Tables

List of Symbols

List of Abbreviations

Abstract

Both size and cost of mechanical and optical inertial navigation systems (INS) have prevented their use in many applications. By developing a micromachined gyroscope and combining it with existing micromachined accelerometer designs to form a low sensitivity INS, the cost would be reduced by a factor of 10 or more. The lower per unit cost would open new areas for INS use. A second advantage of the micromachined INS would be its size. A micromachined INS would weigh only a few ounces and take significantly less space. This would allow more room for electronics and the weight reduction would lead to longer mission times.

In this thesis three micromachined gyroscopes were developed and fabricated: a micromachined comb-drive vibrating gyroscope, a planar gimballed gyroscope, and a vibrating ring gyroscope. The micromachined gyroscopes were fabricated using the Multi User MEMS (Micro Electro Mechanical Systems) Process (MUMPS). These devices were then tested in AFIT's microelectronics laboratories.

DESIGN AND FABRICATION OF A MICROMECHANICAL GYROSCOPE

I. Introduction

In order to calculate the position of a moving body accurately, it is necessary for navigation systems to measure both the motion and orientation of the body. An inertial navigation system (INS) can be used to provide the necessary information to calculate position. An INS typically consists of three orthogonally oriented accelerometers and three gyroscopes, also orthogonally oriented. Accelerometer outputs are used to calculate acceleration, while gyroscope outputs are used to calculate angular orientation of the body. Errors in calculating angular orientation cause the INS calculated position to drift with time, making it necessary to update the INS with the correct position or to develop a means of modeling the drift rate in order to maintain accurate position data. The impact of the drift rate on positional accuracy makes it necessary to have highly accurate gyroscopes. Sensitivity constraints of devices currently used make them costly and thus unsuitable for many applications. It has been shown that by integrating position information from the Global Positioning System (GPS) with a medium accuracy INS, accurate long-term position calculations can be made [3–6]. The GPS system provides highly accurate long term position information. On the other hand, high frequency maneuvers, poor satellite coverage, and the time necessary to calculate position causes the GPS system, as currently implemented, difficulty in tracking highly dynamic movements. However, when accompanied by an INS capable of calculating accurate short-term positions, the resulting

integrated navigation system can provide not only accurate short-term position calculations (INS) but also accurate long-term positions (GPS). The accurate long-term characteristics of GPS make it possible for an inexpensive, moderately precise (rather than high-precision high-cost) INS to be integrated with GPS to provide an INS capable of aerospace navigation. One example of an integrated system is the integration of the Litton LR-80 attitude heading and referencing system (AHARS) with GPS. The LR-80 is a 10 nmi/hr system in the 0.5 degree heading category, a poor INS. However, when it is integrated with GPS, the overall system accuracy is 20 m absolute position error and 0.25 degree heading error [3].

Both size and cost of mechanical and optical inertial navigation systems have prevented their use in many applications. By developing a micro machined gyroscope and combining it with existing micromachined accelerometer designs to form a low sensitivity INS, the cost would be reduced by a factor of 10 or more. The lower per unit cost would open new areas for INS use. A second advantage of the micromachined INS would be its size. The Litton LN94, currently used in the F15 navigation system, weighs over 45 lbs and is mounted in a 14 in x 14 in x 7 in case. A micromachined INS would weigh only a few ounces with a size closer to 3 in x 3 in x 0.5 in. The size reduction would allow more room for electronics and the weight reduction would lead to longer mission times. The micromachined INS may also be integrated with the work currently being accomplished at the Air Force Institute of Technology (AFIT) to build a completely jamming/spoofing-resistant GPS receiver on a printed circuit board (PCB). The resulting integrated system would possess both the size and cost advantages mentioned above and maintain the accuracies required for many aerospace applications.

Micromachined gyroscope designs have been constructed using vibrating rings [7], vibrating combs [8], and planar vibratory rate gyroscopes [9]. These designs are implemented using costly custom fabrication processes. If a standard fabrication procedure could be used to implement a design, the per-unit cost would decrease dramatically. This thesis research will be limited to the development of a micromachined silicon-based gyroscope fabricated using the Multi User MEMS (Micro Electro Mechanical Systems) Process (MUMPS) and sensing circuitry developed using the Metal Oxide Semiconductor Implementation System (MOSIS) process.

Development of a micromechanical gyroscope capable of being integrated into an INS would reduce the size and cost of current inertial navigation systems. By using a commercial polycrystalline silicon (polysilicon) micromachining process, availability would be increased and cost of functional devices would be further reduced. The goal of this research is to develop, fabricate and test a micro mechanical gyroscope using a commercially available fabrication process, capable of sensing an angular rotation of $1 deg/sec$ with a range of $\pm 500 deg/sec$.

Three designs are investigated: a micromachined comb-drive vibrating gyroscope, a planar gimballed gyroscope, and a vibrating ring gyroscope. Each of the designs is fabricated and tested for functionality and sensitivity. All three of the designs are implemented using the MUMPS process. Sense circuitry is fabricated using the MOSIS process. In this thesis, fabricated devices are compared to the Charles Stark Draper Laboratories tuning fork gyroscope [9] and the University of Michigan resonating shell gyroscope [7,10]. Devices fabricated were first tested at atmospheric pressure and then in a near vacuum. Resonant frequencies were established using the network analyzer available in AFIT's microelec-

tronics laboratory. Device layouts for surface micromachined MEMS are completed using Cadence software and are fabricated by MCNC corporation of North Carolina (MCNC). Circuit layouts were completed using Magic software and fabricated using the MOSIS process.

II. Background

2.1 Vibrating Gyroscopes

In 1851 a French scientist named Leon Focault studied the earth's rotation through the use of a large pendulum [11]. Focault noted that as the earth rotated the plane in which the pendulum was oscillating precessed about its central axis. Focault correctly reasoned that the precession of the plane of oscillation was caused by the Coriolis effect. The following example is intended to explain the Coriolis effect in greater detail.

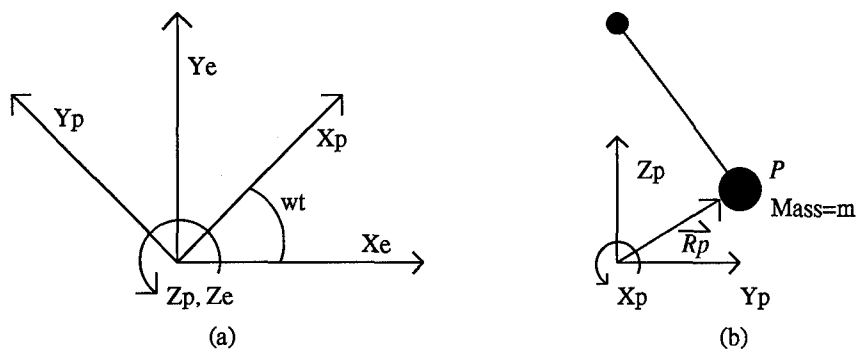

Figure 2.1 (a) Declaration of the e and p frames, (b) location of the pendulum in the p frame.

2.1.1 Example: Coriolis effect. A snapshot of a swinging pendulum is shown in Figure 2.1(b). The position vector to the pendulum is defined as $\vec{R}_p$ and the p reference frame is rotating at a constant angular velocity $\vec{\omega}$ with respect to the e frame. Given the definitions below, the acceleration of the pendulum with respect to the e frame expressed

in the p frame ${}^{e}\vec{A}^{p}$ will be derived.

$$\vec{R}_p = \begin{bmatrix} x_p \\ y_p \\ z_p \end{bmatrix} \tag{2.1}$$

$$\vec{\omega} = \begin{bmatrix} 0 \\ 0 \\ \omega_z \end{bmatrix} \tag{2.2}$$

The velocity of point P with respect to the e frame, coordinatized in the p frame ${}^{e}\vec{V}^{p}$, is:

$${}^{e}\vec{V}^{p} = \frac{{}^{p}d}{dt}\vec{R}_p + \vec{\omega} \times \vec{R}_p \tag{2.3}$$

The acceleration of point P with respect to the e frame, coordinatized in the p frame ${}^{e}\vec{A}^{p}$, is:

$${}^{e}\vec{A}^{p} = \frac{{}^{p}d}{dt}{}^{e}\vec{V}^{p} + \vec{\omega} \times {}^{e}\vec{V}^{p} \tag{2.4}$$

$${}^{e}\vec{A}^{p} = \ddot{\vec{R}}_p + \underbrace{2\vec{\omega} \times \dot{\vec{R}}_p}_{Coriolis\,Acceleration} + \vec{\omega} \times \vec{\omega} \times \vec{R}_p + \dot{\vec{\omega}} \times \vec{R}_p \tag{2.5}$$

Where $\dot{\vec{R}}_p$ and $\ddot{\vec{R}}_p$ are the first and second derivatives of $\vec{R}_p$ with respect to time.

Expanding the Coriolis acceleration term yields:

$$2\vec{\omega} \times \dot{\vec{R}}_p = 2 \begin{bmatrix} 0 \\ 0 \\ \omega_z \end{bmatrix} \times \begin{bmatrix} \dot{x_p} \\ \dot{y_p} \\ \dot{z_p} \end{bmatrix} \tag{2.6}$$

$$2\vec{\omega} \times \dot{\vec{R}}_p = \begin{bmatrix} -2\omega_z \dot{y_p} \\ 2\omega_z \dot{x_p} \\ 0 \end{bmatrix} \tag{2.7}$$

Equation (2.7) shows the results of expanding the Coriolis acceleration term for this example. The result is a compound acceleration in the X_p and Y_p directions. The acceleration of the pendulum mass will cause the pendulum's plane of oscillation to precess about the central axis, in this case the Z_p axis. Given two reference frames rotating with respect to each other, when a particle's acceleration is calculated, the Coriolis acceleration will cause a coupling between two vibrational modes in the structure. In this example the pendulum, originally oscillating in the Y_pZ_p plane, begins to rotate about the Z_p axis. Vibrational gyroscopes depend on this coupling between vibrational modes in order to measure angular rates; their sensitivity is directly related to the magnitude of coupling present.

2.1.2 Types of Vibrating Gyroscopes. Some structures other than Focault's pendulum illustrate coupling between vibrational modes when subjected to rotation. Of these structures, vibrating prismatic beams, tuning forks, dual accelerometers, planar gyroscopes and vibrating shells are available either commercially or as research devices [12]. Each of these devices will be discussed, noting their significant strengths and weaknesses.

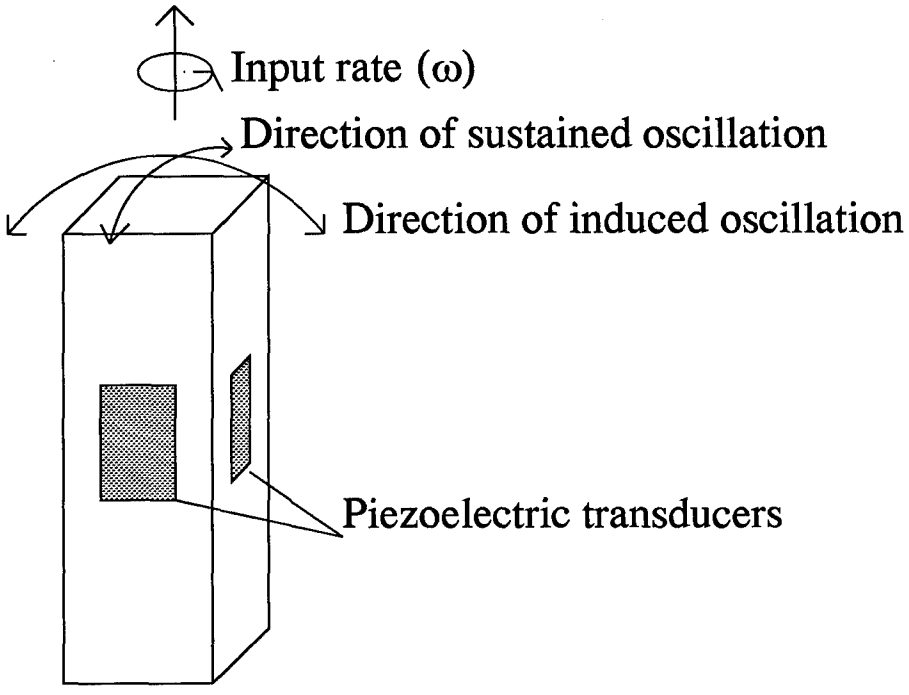

Figure 2.2 Prismatic beam gyroscope.

2.1.2.1 Vibrating Prismatic Beams: Vibrating prismatic beams are similar to the Focault pendulum in operation. Prismatic beams use coupling between two identical vibrating modes to sense rotation. Historically these devices have shown sensitivity to temperature variations and spurious vibrations [13]. Figure 2.2 shows one possible implementation of a vibrating prismatic beam. Because of its sensitivity to off-axis vibrations, the vibrating prismatic beam is not suited for use in an INS.

2.1.2.2 Tuning Forks: As early as 1958, the Sperry Gyroscope company had developed a navigation grade tuning fork gyroscope [14,15]. The Sperry gyrotron was machined from a single block of aluminum on a macroscopic level. The tines of the tuning fork, shown in Figure 2.3, are resonated in anti-phase. When a rotation is input about the central axis, a sinusoidal torque is generated about the support. This causes the support

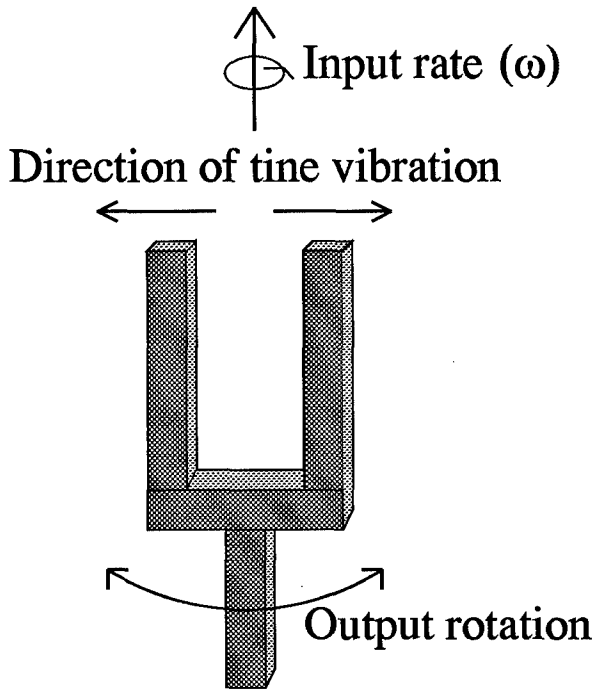

Figure 2.3 Tuning fork gyroscope.

to undergo torsion. By measuring the torsion of the support, the input angular rate may be calculated. In the tuning fork gyroscope, the primary vibrational mode's resonant frequency is not the same as the secondary mode's resonant frequency; this limits sensitivity. Another major difficulty in the tuning fork gyroscope is that, if the mass centers of the tines are slightly off center, a torsion identical to the one caused by the Coriolis effect will be seen on the output. In spite of these difficulties, a micromachined tuning fork gyroscope was successfully developed at Carl Stark Draper Laboratories using a custom fabrication procedure [9]. The gyroscope design was implemented using two micromachining techniques. The first technique used single crystal silicon electrostatically bonded to glass. The second technique used electroformed nickel. The single crystal silicon was bulk micromachined using a reactive ion etch (RIE), and boron was used as an etch stop. The resulting gyro-

scope demonstrated sensitivities of 5000 deg/hr in a 60 Hz bandwidth, and 0.19 deg/sec in a 1 Hz bandwidth. The electroformed nickel gyroscope was patterned in photo resist and plated using nickel. Specific sensitivity data was not provided on the nickel gyroscope. It was, however, stated the single crystal silicon implementation performed better than the nickel implementation [9]. These devices do not have the sensitivities desired, 0.1 deg/sec in a 1 Hz bandwith, for avionics applications.

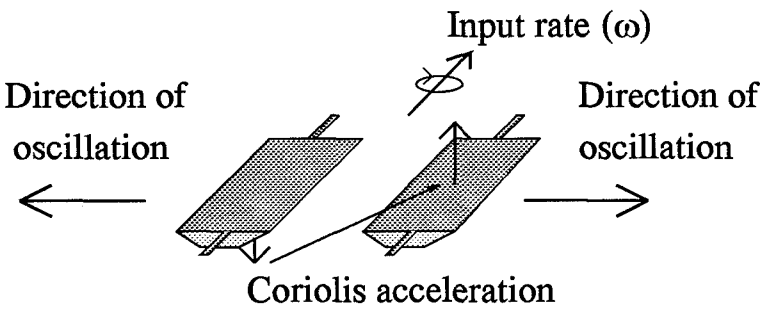

Figure 2.4 Dual accelerometer gyroscope.

2.1.2.3 Dual Accelerometers: Dual accelerometers, illustrated in Figure 2.4, are a variation of the tuning fork concept. Two accelerometers are placed in parallel and vibrated in anti-phase. When the device is subjected to rotation, the Coriolis acceleration acts perpendicular to the plane of vibration [7]. This type of gyroscope is sensitive to mass imbalances and is suseptable to spurious vibrations. The dual accelerometer approach has not been pursued because of its sensitivity to off-axis vibrations.

2.1.2.4 Planar Gyroscopes: A planar gyroscope, illustrated in Figure 2.5, is a two-gimbaled gyroscope. The outer gimbal is subjected to a continuous oscillation. When the device is subjected to rotation, about the sensitive axis, the inner gimbal begins to vibrate. The major drawback to this design is that the drive and sense oscillations are often

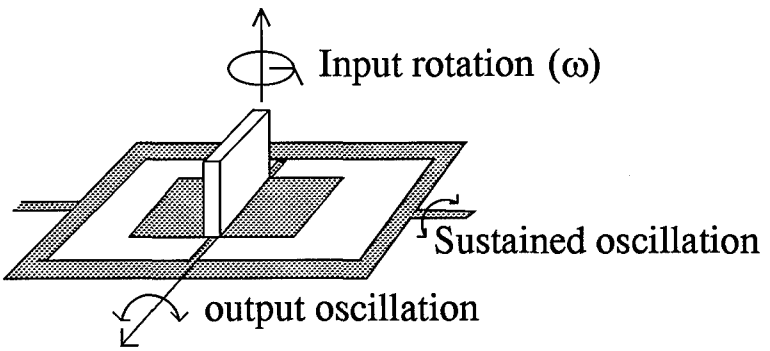

Figure 2.5 Planar gyroscope.

not at resonant frequencies, making it less sensitive. Charles Stark Draper Laboratories has successfully constructed a monolithic silicon planar gyroscope [16–18]. The device is sensitive to angular rates of 10 rad/sec (573 deg/sec); this device is severely limited by its resolution. Device construction was completed by using a bulk micromachining process and then electroforming gold on top of the device. A similar gyroscope design, constructed completely from silicon, formed a silicon pyramid in the center of a thin membrane [19]. The membrane allowed the pyramid to be electrostatically driven to resonance in one direction. An input rotation caused the pyramid oscillation to couple into the identical secondary resonant mode. To date the maximum rate sensed with these devices is 300 deg/sec. If a *perfectly* manufactured device is fabricated the noise equivalent rotation rate would be 0.07 deg/sec. This device currently suffers from the same limitations reported by Charles Stark Draper Laboratories.

2.1.2.5 Vibrating Shells: In 1890 G. H. Bryan found that thin-walled resonators could be used to sense angular rotations [20]. Bryan discovered that the vibratory modes of a ringing wine glass precess when the glass is rotated about its stem. Furthermore, Bryan noted that the precession was due to the Coriolis acceleration and that the

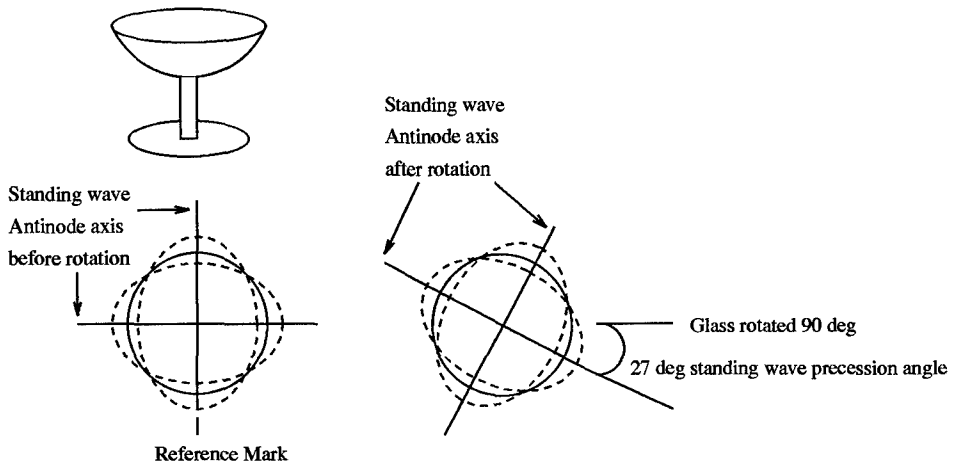

Figure 2.6 Vibrating shell gyroscope [11].

angular gain could be computed based on geometry. Delco Systems Operations developed a Hemispherical Resonating Gyro (HRG) that operates by measuring the precession of the nodes in a vibrating shell. The HRG was machined on a macroscopic level from fused quartz with a metallized surface. The surface was then highly polished to reduce mass imbalances. Delco claims that the HRG is a nearly ideal sensor because of its [11]:

1. Solid state reliability
    - no rotating parts
    - small inertial dissipation
2. Insensitivity to magnetic fields
3. Nuclear ride-through capability
4. Negligible acceleration sensitivity
    - Same performance in the earth's atmosphere, as in space
5. No temperature control necessary

The University of Michigan in coordination with General Motors has experimented with a vibrating ring gyroscope constructed by electro-forming nickel on top of a silicon wafer processed with a standard Metal Oxide Semiconductor (MOS) process [7,10]. The resulting gyroscope demonstrated sensitivities of 0.5 deg/sec in a 10 Hz bandwidth. The gyroscope was electrostaticly balanced to account for mass imbalances and operated at self resonance to allow for drift of the resonant frequency with temperature. The electrostatic balancing must be accomplished on each device, making mass production difficult. The major factor limiting the device sensitivity is the use of nickel as a device material. The nickel device has a resonant Q of 2×10^3, in comparison with polysilicon devices which typically have a resonant Q on the order of 1×10^6 [7].

2.2 Micromachining

Silicon is a mechanical material with diverse properties [2]. Silicon has a similar modulus of elasticity and a greater yield strength than stainless steel, but a density less than that of aluminum. In addition, silicon has almost no mechanical hysteresis, making it ideal as a sensor material. Table 2.1 compares silicon to other materials used in device construction.

Two methods of constructing micro-electro-mechanical systems (MEMS) with a silicon substrate are bulk and surface micro-machining. The following discussion is an overview of these two methods of device fabrication.

Table 2.1 The Mechanical Properties of Silicon [2].

Material	Yield strength $10^9 \frac{N}{m^2}$	Knoop hardness $\frac{Kg}{mm^2}$	Young's modulus $\frac{10^{11}N}{m^2}$	Density $\frac{g}{cm^3}$	Thermal Conductivity $\frac{W}{cm°C}$
Diamond	53	7000	10.35	3.5	20
Silicon carbide	21	2480	7	3.2	3.5
Silicon nitride	14	3486	3.85	3.1	0.19
Iron	12.6	400	1.96	7.8	0.803
Silicon	7	850	1.9	2.3	1.57
Tungsten	4	485	4.1	19.3	1.78
Stainless steel	2.1	660	2	7.9	0.329
Molybdenum	2.1	275	3.43	10.3	1.38
Aluminum	0.17	130	0.7	2.7	2.36

2.2.1 Bulk Micromachining. In the 1950's researchers discovered that certain chemicals etch at faster rates along different crystal planes of silicon [1]. Chemicals such as potassium hydroxide (KOH), ethylenediamine-pyrocatechol (EDP), and cesium hydroxide (CsOH) etch along some silicon crystal planes significantly faster than others. Other chemicals etch at equal rates in all directions. Chemicals that etch selectively are called anisotropic etchants; chemicals that etch at equal rates in all directions are called isotropic (Fig. 2.7). Anisotropic etches are characterized by sharp corners that may be vertical or

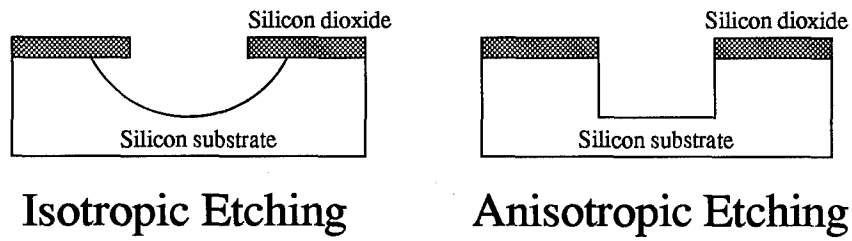

Figure 2.7 Isotropic vs. anisotropic silicon etching [21].

angled depending on crystal plane orientations. Figure 2.8 shows the effects of etching two different silicon wafer surfaces with the same anisotropic etchant. Crystal directions are

shown and the corresponding Miller index is provided [22]. The 54.7^o angle is a result of the orientation of the $< 111 >$ crystal plate with respect to the $< 100 >$. Similarly the 90^o angle is a result of the $< 111 >$ crystal plane's orientation with respect to the $< 110 >$ surface. Structures developed using anisotropic etchants also depend on the shape of the

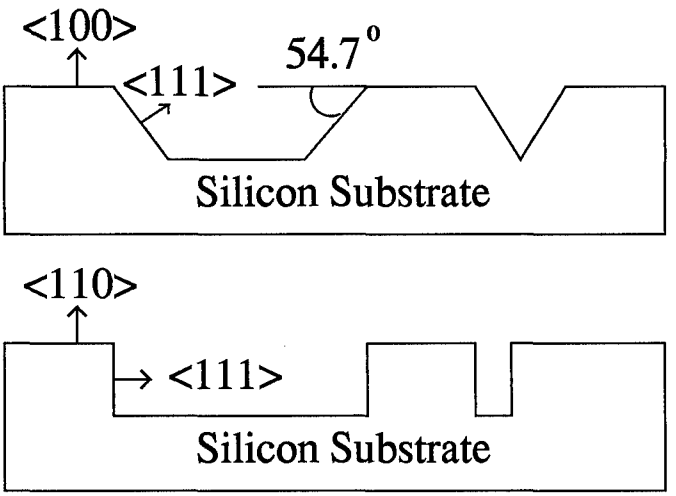

Figure 2.8 Anisotropic etching of two different silicon wafer surfaces [1].

opening in the mask layer. Table 2.2 lists etch results for differently shaped windows exposing a $< 100 >$ surface.

Table 2.2 Window Shape and Etch Results for $< 100 >$ Silicon Surface [1].

Window Shape	Etch Results
Square	Truncated Pyramid
Rectangle	Rectangular Pit
Circle	Pyramidal
Arbitrary poly	Rectangular

Anisotropic etchants may be chosen based not only on the crystal direction that etches faster but also on the etch rate of different materials. For example, if a layer of silicon dioxide (SiO_2) were grown on top of a $< 100 >$ silicon surface, a window were cut

in the SiO_2 with the shape shown in Figure 2.9(a), and the wafer were placed in a KOH solution, then the structure shown in Figure 2.9(b) would result.

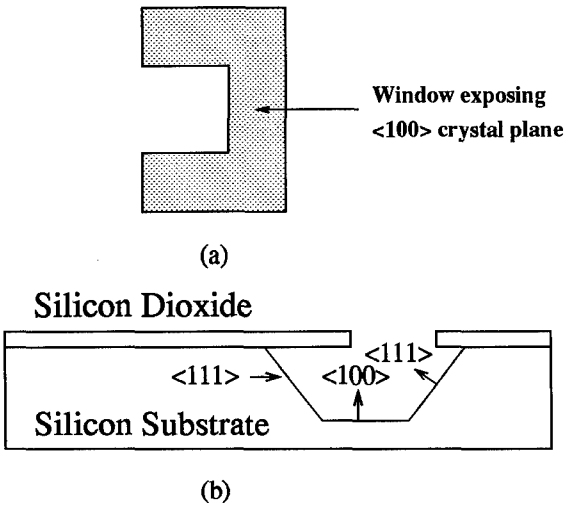

Figure 2.9 (a) Etch window shape exposing the $< 100 >$ crystal plane as seen from above. (b) Resulting structure after anisotropically etching the structure in (a).

Bulk micro-machined structures may also be defined through the use of etch stops. Etch stops are used to slow the etch rate of silicon further when exposed to certain chemicals. Two common types of etch stops are boron doping and electro-chemical. Regions highly doped with boron ($1 \times 10^{20} cm^{-3}$) cause the etch rates to slow by as much as 1,000 times. Electro-chemical etch stops may also be used. One way to implement an electro-chemical etch stop is illustrated in Figure 2.10. The wafer to be etched is suspended in a KOH-water solution. The PN junction shown in Figure 2.10 is reverse biased as long as the P layer remains intact. When the P region is fully etched, current begins to flow and a layer of oxide is formed, stopping the etch. This technique may be used to create diaphragms 2 μm thick [1].

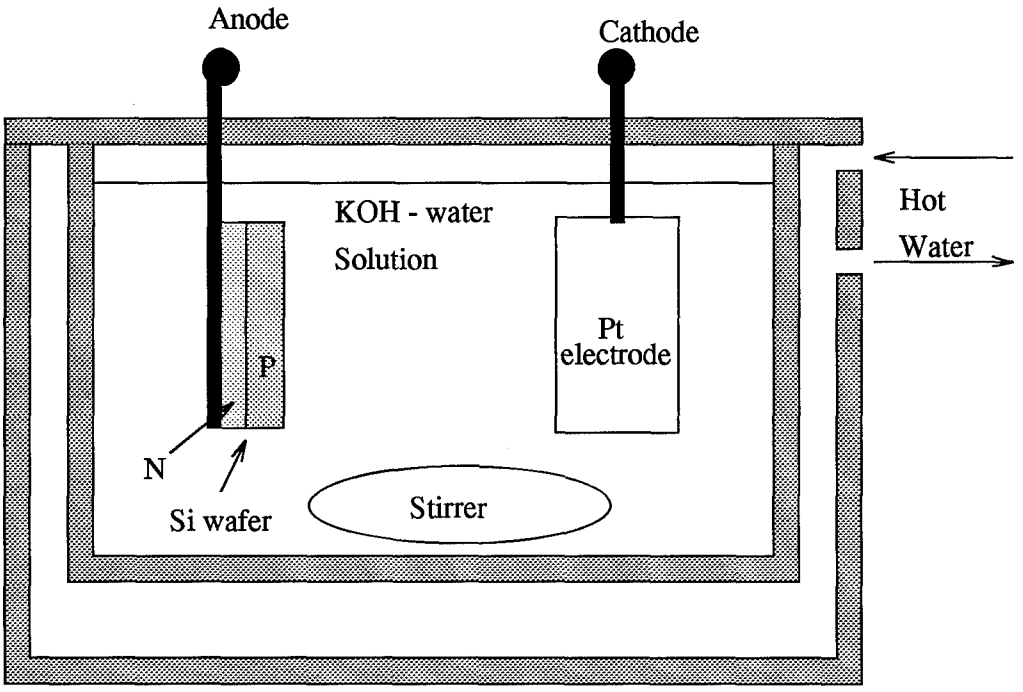

Figure 2.10 Electro-chemical etch stop technique [1].

Through combined use of isotropic and anisotropic etchants, under-cutting of SiO_2 layers, and etch stops, complex structures may be developed. Examples of structures created using bulk micro-machining are accelerometers, micro valves, and hot plates [2,23, 24].

2.2.2 Surface Micromachining. In surface micromachining, structures are developed on top of, not within, the substrate (wafer). A spacer or sacrificial layer is grown on top of the substrate, then a mechanical layer is grown and patterned on top of the sacrificial layer. Once the mechanical layer is patterned, the sacrificial layer is etched away, leaving a suspended structure. This process of etching the sacrificial layer is called releasing the structure. Figure 2.11 shows an example of a cantilever beam created using surface micromachining. Surface micro-machining is not limited to one mechanical layer [25]. In the

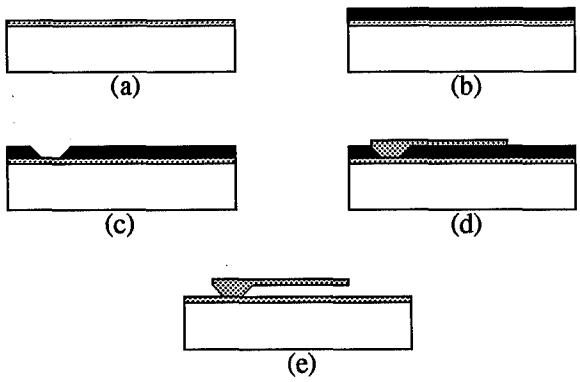

Figure 2.11 (a) silicon wafer, (b) wafer with sacrificial oxide grown, (c) oxide patterned, (d) mechanical layer grown, (e) sacrificial oxide layer removed.

previous example, after the mechanical layer is grown and patterned, a second sacrificial layer may be grown and patterned. A second mechanical layer may then be grown and patterned. Once the second mechanical layer is grown and patterned the whole structure may be released. By increasing the number of mechanical layers, the complexity of designs possible increases. The cost of using more layers is an increased difficulty of fabrication. Surface micro-machining has been used to fabricate many devices such as micro-motors, resonant combs and vibrating rings [26,27].

2.2.3 MUMPS Process Overview. The Multi-User MEMS Process (MUMPS) is a 3-layer polysilicon process with a minimum design rule of 2 μm. Table 2.3 provides an overview of the layers in the MUMPS process. Once all the layers have been deposited and patterned the structure must be released. This step is completed by placing the die into a hydrofluoric acid (HF) bath dissolving both sacrificial oxide layers and releasing the devices. Figure 2.12 shows a released mechanical structure identifying each of the layers present.

Table 2.3 Overview of Films in the MUMPS Process [28].

Layer Name	Film Description	Comments
Nitride	0.5 μm silicon nitride	isolation layer
Poly 0	0.5 μm polysilicon	ground plane, wiring
1st Oxide	2.0 μm oxide (PSG)	1st sacrificial layer, 0.75 μm dimples
Poly 1	2.0 μm polysilicon	first mechanical layer
2nd Oxide	0.5 μm oxide (PSG)	2nd sacrificial layer
Poly 2	1.5 μm polysilicon	second mechanical layer
Metal	0.5 μm evaporated metal	low resistivity contact, reflective (gold)

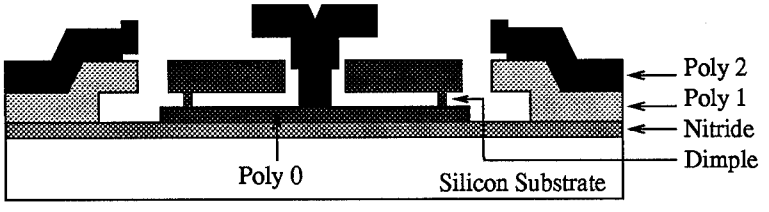

Figure 2.12 Released device cross section [29].

2.3 Chapter Summary

This chapter presented three main topics. The first was the Coriolis effect. The Coriolis effect is the underlying principal that all vibrational gyroscopes rely on, it accounts for the coupling of energy from one vibrational mode to another. The second was a discussion of different types of vibrational gyroscopes. There were five possible designs; the vibrating prismatic beam, tuning forks, dual accelerometers, planar, and resonating shell gyroscopes. Where applicable the performance of fabricated devices is related. The third topic was micromachining. An introduction to both bulk and surface micromachining was presented along with a specific discussion of the process used to complete this thesis. In the following chapter specific device theory will be derived for a tuning fork gyroscope, a planar gyroscope, and a resonant shell gyroscope.

III. Theory

Three types of vibrational gyroscopes are investigated; this chapter describes the theory behind the operation of each. The three devices are the vibrating comb gyroscope, planar or dumbbell gyroscope, and the vibrating ring gyroscope.

3.1 Vibrating Comb Gyroscope

In this section the structure shown in Figure 3.1 is analyzed. The torque equations

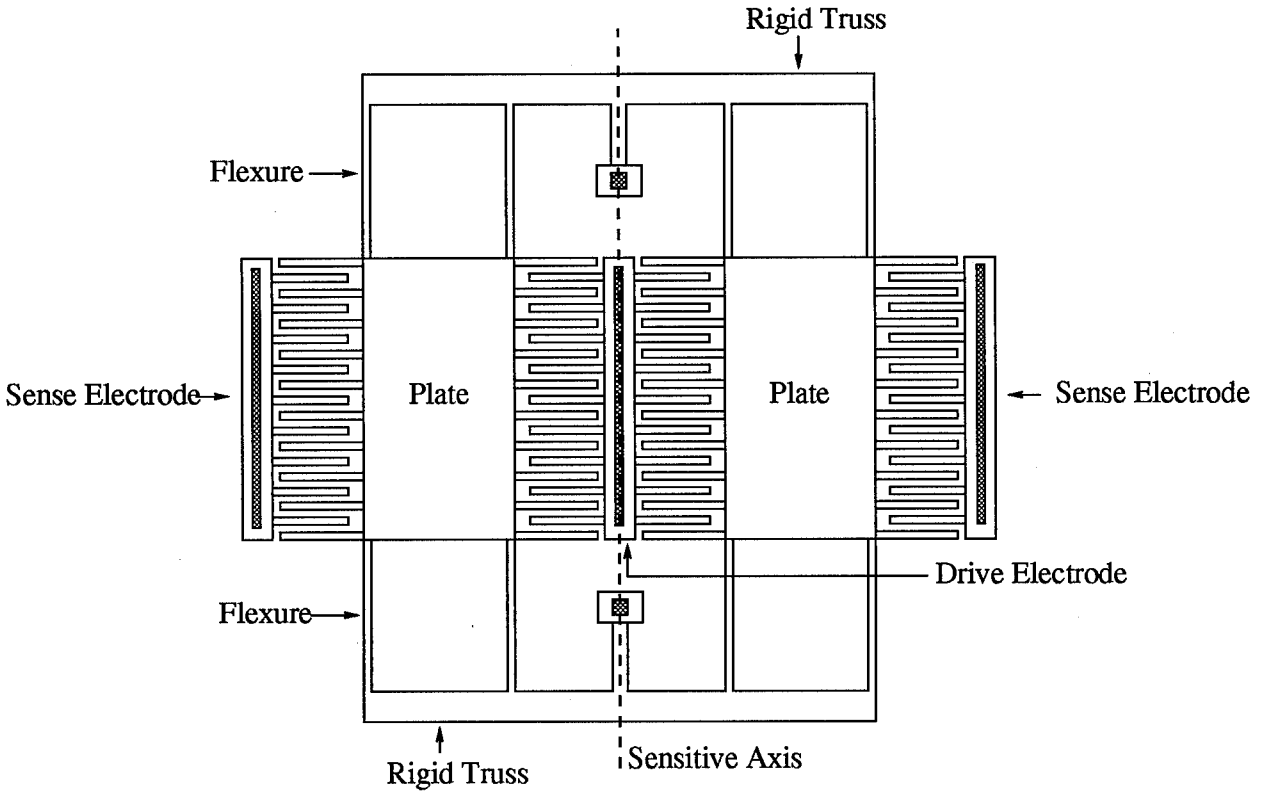

Figure 3.1 Comb drive gyroscope illustration.

are generated and differential equations for output oscillations are derived for a single input about the device's sensitive axis. A complete derivation for an arbitrary input rotation is

completed in Appendix A. The derivation will be completed for one vibrating member. A vibrating member, shown in Figure 3.2, consists of the four support flexures, plate, and the drive and sense combs. Because of device symmetry, the derivation for the second vibrating member is identical to the first. In this analysis the masses of the plate, drive

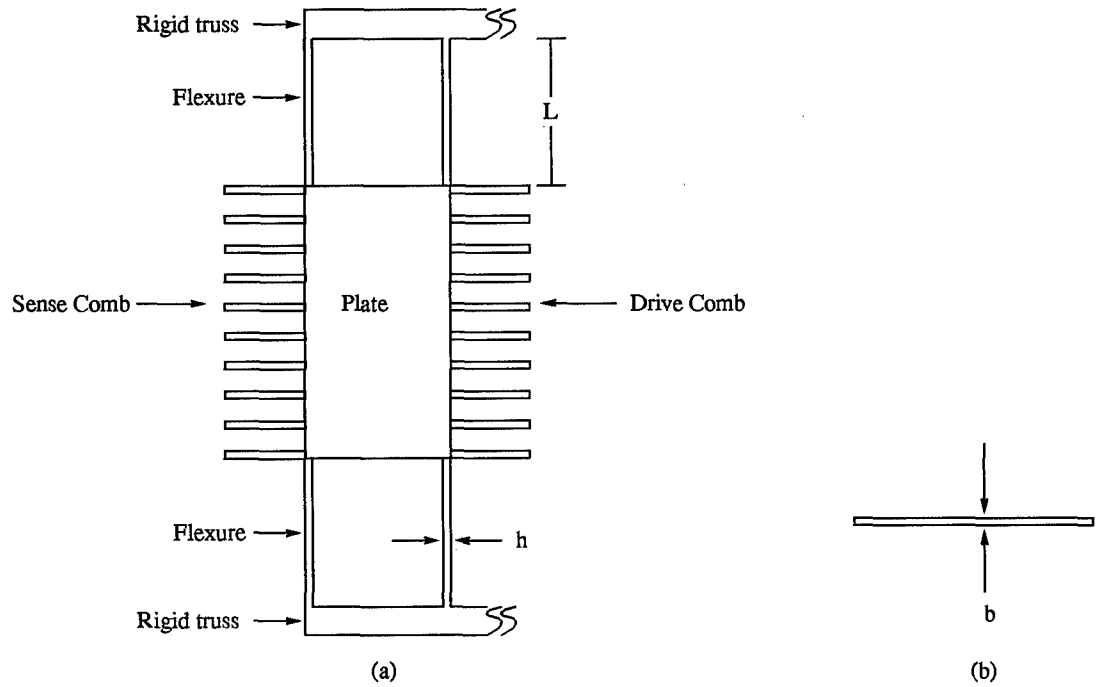

Figure 3.2 Vibrating member illustration; (a) Top view. (b) Side view.

comb, and sense comb are combined and denoted as M_p. M will refer to the mass of the four flexures.

Similar to both the Sperry Gyroscope [15] and the Charles Stark Draper Laboratories gyroscopes [9], the proposed design requires the two vibrating members to be vibrated in anti-phase. In order to reduce the voltages necessary to sustain an oscillation the device is oscillated at its resonant frequency. The resonant frequency of the device may be

determined using Rayleigh's method [27]:

$$f_r = \frac{1}{2\pi}\left[\frac{k_{sys}}{(M_p + 0.3714M)}\right]^{\frac{1}{2}} \tag{3.1}$$

where M_p and M represent the mass of the plate, including drive and sense fingers, and the mass of the supporting beams, respectively.

For this analysis the trusses joining the flexure segments are assumed to be rigid. As a result, the equivalent spring constant for a single beam, k, is broken down into three parts; k_1, the spring constant due to the residual stress; k_2, the spring constant due to beam bending; and k_3, the spring constant due to beam elongation. Residual stress refers to the stress internal to the material, it is a function of growth conditions. k_{sys}, the system spring constant, is the sum of the spring constants from each of the four support beams and is written as in Equation (3.2).

$$k_{sys} = 4(k_1 + k_2 + k_3) \tag{3.2}$$

The vibrating members are assumed to have extremely small lateral displacements. Under this assumption k_3 is several orders of magnitude smaller than k_1 and k_2. As a result k_3 is assumed to be negligible.

The spring constant due to residual stress k_1 is calculated in this section. Figure 3.3 shows an illustration of the the variables necessary to calculate k_1. The axial force, P in Figure 3.3, is constant with deflection, d in Figure 3.3, because elongation will be accounted for by k_3. The force stress relationship is given in Equation (3.3) and the force

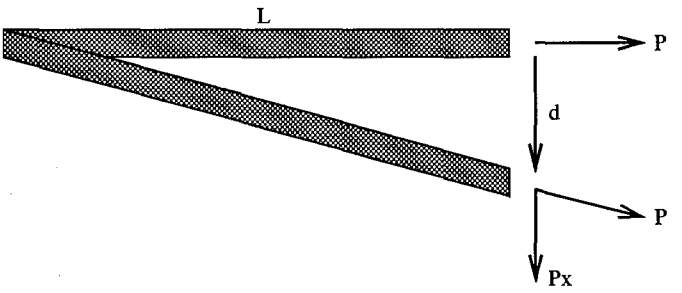

Figure 3.3 k_1 spring constant illustration.

balance as related to geometry is shown in Equation (3.4) [30].

$$P = \sigma_R A = bh\sigma_R \tag{3.3}$$

$$\frac{P_x}{P} = \frac{d}{L} \tag{3.4}$$

where b represents the beam width and h is the beam thickness in the direction of the desired motion. σ_R is the residual stress of the material and A is the cross sectional area of the beam. The spring constant k_1 is defined in Equation (3.5)

$$k_1 = \frac{P_x}{d} = \frac{bh}{L}\sigma_R \tag{3.5}$$

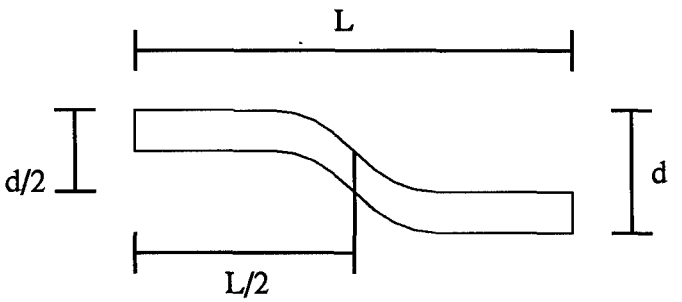

Figure 3.4 k_2 spring constant illustration.

By taking advantage of symmetry, the analysis for the k_2 calculation is broken into two parts (see Figure 3.4). For a rectangular beam, Equation (3.6) defines the displacement of half the beam [30]:

$$(\frac{d}{2}) = \frac{P_x(\frac{L}{2})^3}{3EI} \tag{3.6}$$

Where E is Young's Modulus and the polar moment of inertia for a rectangular beam, I, is defined in Equation (3.7)

$$I = \frac{hb^3}{12} \tag{3.7}$$

Multiplying this equation by two and solving for $\frac{P_x}{d}$ yields Equation(3.8)

$$k_2 = \frac{12EI}{L^3} \tag{3.8}$$

Substituting Equation (3.7) into Equation (3.8) yields the final equation for k_2 in terms of the beam width (b), length (L), thickness (h), and Young's Modulus (E):

$$k_2 = \frac{Ebh^3}{L^3} \tag{3.9}$$

Finally, substituting Equations (3.9) and (3.5) into Equation (3.2), the equivalent spring constant for the vibrating member is given by Equation (3.10):

$$k_{sys} = 4(\frac{bh}{L}\sigma_R + \frac{Ebh^3}{L^3}) \tag{3.10}$$

This value of k_{sys} is used in Equation (3.1) to calculate the vibrating member's resonant frequency.

The quality factor Q of this structure, assuming that most of the damping is from air flow underneath the plate, is [27]:

$$Q = \frac{d_p}{\mu A_p}[(M_p + 0.3714M)k_{sys}]^{\frac{1}{2}} \tag{3.11}$$

Where μ is the viscous damping of air ($1.81 \times 10^{-5} N\ s\ m^{-2}$ at $20^{o}C$ [31]), A_p is the surface area of the plate, and d_p is the distance between the plate and the substrate.

Each of the vibrating members is driven by the center electrode in Fig 3.1 with a voltage:

$$v_d(t) = V_p + v_d sin(\omega t) \tag{3.12}$$

Where V_p and v_d are scalar magnitudes. This causes the vibrating members to oscillate in antiphase. The lateral (x) displacement of the vibrating member is found by applying Hooks law, Equation (3.13):

$$x = \frac{F_x}{k_{sys}} \tag{3.13}$$

$$F_x = \frac{v_d^2(\frac{\partial C}{\partial x})}{2} \tag{3.14}$$

$$\frac{\partial x}{\partial t} = \frac{(\frac{\partial C}{\partial x})}{2k_{sys}} \frac{\partial v_d(t)^2}{\partial t} \tag{3.15}$$

In Equation (3.14), C is the drive electrode interface capacitance defined by Equation (3.16).

$$C = \frac{n \times \epsilon bl(x)}{d_e} \tag{3.16}$$

where n is the number of drive fingers on the vibrating member; d_e is the distance between the stationary and moving electrode ($2\mu m$); and $l(x)$ is the length of overlap as a function of displacement in the x direction. For completely lateral motion, $\frac{\partial C}{\partial x}$; is a constant, in other words $l(x)$ is a linear function of x. When the device experiences an input rotation, this partial derivative is no longer a constant and is instead a nonlinear function. The transfer function between the phasor drive voltage V_d and the phasor displacement X at resonance may be written in terms of the magnitude of $\frac{\partial C}{\partial x}$

$$\left|\frac{X}{V_d}\right| = V_p \frac{Q}{k_{sys}} \left|\frac{\partial C}{\partial x}\right| \tag{3.17}$$

This information may be used to design the resonant characteristics of the device in Figure 3.1. Once this is done, it is necessary to calculate the response to an input rotation about the device's sensitive axis. Figure 3.5 shows a simplified view of the device in Figure 3.1 defining the basis, system origin, position vectors to the vibrating members centers of mass, the magnitudes R and H used to write the position vectors in the basis, and noting the sensitive axis.

For this analysis let both vibrating members be subjected to a sustained oscillatory displacement given by Equation (3.18), where $\omega = 2\pi f_r$ is the radian resonant frequency calculated by using Equation (3.1) and Ω is the amplitude of the oscillation.

$$\Delta x = \Omega sin(\omega t) \tag{3.18}$$

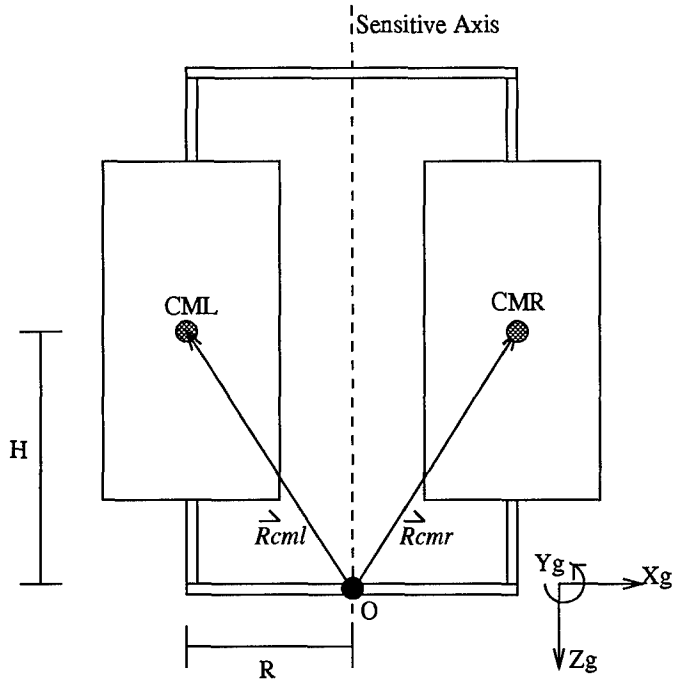

Figure 3.5 Simplified tuning fork gyroscope diagram.

where Δx is the change in lateral position. The position vectors of the left and right vibrating member's center of mass may then be written as:

$$\vec{R}_{cml} = -(R + \Omega sin(\omega t))\hat{x}_g - H\hat{z}_g \tag{3.19}$$

$$\vec{R}_{cmr} = (R + \Omega sin(\omega t))\hat{x}_g - H\hat{z}_g \tag{3.20}$$

Where $\vec{R}_{cml}$ and $\vec{R}_{cmr}$ represent the position vectors to the left and right members' centers of mass, respectively. When the device is subjected to a rotation about its sensitive axis, at a rate ω_o, a compound acceleration is applied to the resonating members. Using the same approach as in the Coriolis acceleration example, the accelerations of the left and

right member's mass centers are found to be:

$$\vec{a}_{cml} = [\Omega(\omega^2 + \omega_o^2)sin(\omega t) + \omega_o^2 R]\hat{x}_g - [\dot{\omega}_o R + \dot{\omega}_o \Omega sin(\omega t) + 2\omega_o \Omega \omega cos(\omega t)]\hat{y}_g \quad (3.21)$$

$$\vec{a}_{cmr} = [-\Omega(\omega^2 - \omega_o^2)sin(\omega t) - \omega_o^2 R]\hat{x}_g + [\dot{\omega}_o R + \dot{\omega}_o \Omega sin(\omega t) + 2\omega_o \Omega cos(\omega t)]\hat{y}_g \quad (3.22)$$

The acceleration of each member is needed to calculate the torque that each member applies about the central axis of the device. The torque equation in vector form is

$$\vec{T} = \vec{R} \times \vec{F} \quad (3.23)$$

$\vec{F}$ is defined by Newton's second law [32]

$$\vec{F} = m\vec{a} \quad (3.24)$$

m is defined in this case as the mass of the vibrating member and $\vec{a}$ is the acceleration of the member. Solving the torque equation for the left and right vibrating members yields the torque due to each member about the sensitive axis:

$$\begin{aligned} \vec{T}_{cml} = m[[-H\{\dot{\omega}_o(R + \Omega sin(\omega t) + 2\omega_o \Omega \omega cos(\omega t)\}]\hat{x}_g \\ +[H\{\Omega\omega^2 sin(\omega t) + \omega_o^2[R + \Omega sin(\omega t)]\}]\hat{y}_g \\ +[\dot{\omega}_o(R + \Omega sin(\omega t))^2 + 2\omega_o(R + \Omega sin(\omega t))(\Omega\omega cos(\omega t)]\hat{z}_g] \end{aligned} \quad (3.25)$$

$$\vec{T}_{cmr} = m[[H\{\dot{\omega}_o(R + \Omega sin(\omega t) + 2\omega_o \Omega \omega cos(\omega t)\}]\hat{x}_g$$

$$-[H\{\Omega\omega^2 sin(\omega t) + \omega_o^2[R + \Omega sin(\omega t)]\}]\hat{y}_g$$

$$+[\dot{\omega}_o(R + \Omega sin(\omega t))^2 + 2\omega_o(R + \Omega sin(\omega t))(\Omega\omega cos(\omega t)]\hat{z}_g] \quad (3.26)$$

The net torque about the central axis is found by adding the torques due to each vibrating member. The resulting torque is shown in Equation (3.27):

$$\vec{T} = \emptyset\hat{x}_g + \emptyset\hat{y}_g + 2m[\dot{\omega}_o(R + \Omega sin(\omega t))^2 + 2\omega_o(R + \Omega sin(\omega t))(\Omega\omega cos(\omega t)]\hat{z}_g \quad (3.27)$$

This equation demonstrates an interesting result: the net torque only has a component about the sensitive axis. There is no component about either of the other two axes. This is only true because of the symmetry of the device about the central axis. If the center of mass of either member were a different distance from the origin, then there would be components of torque about the other two axis. It can also be shown that, if the device is symmetric about the line connecting the two mass centers, then the torque about the center axis is the same at both the bottom and top connection points. This is a desirable result; torque of different magnitude about the top or bottom flexure would create highly nonlinear output.

A relationship may now be defined relating the angle A_g, defined to be positive in Figure 3.6, and the torque generated about the sensitive axis given in Equation (3.27).

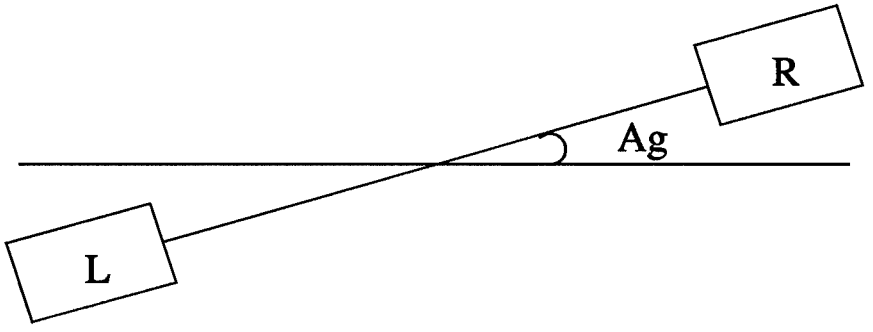

Figure 3.6 Definition of positive Ag.

This relationship is defined below [14]:

$$I(t)\ddot{A}_g = T - C\dot{A}_g - \lambda A_g \tag{3.28}$$

where $I(t)$ is the system's moment of inertia about the central axis, C is the damping coefficient of air, and λ is the torque required to rotate the structure through one radian. λ is determined by solving Equation (3.29) for T where $\theta = 57.3^o$ (1 rad), J is the polar moment of inertia for the support defined in Equation (3.30) [33], L_s is the length of the support, and G is the sheer modulus for polysilicon defined in terms of Young's modulus (E) and Poissons ratio (ν) by Equation (3.31).

$$\theta = \frac{TL_s}{GJ} \tag{3.29}$$

$$J = bh^3\left[\frac{16}{3} - 3.36\frac{h}{b}\left(1 - \frac{h^4}{12b^4}\right)\right] \tag{3.30}$$

$$G = E(1-\nu) \tag{3.31}$$

Equation (3.28) may be resolved into principal axes and $I(t)$ may then be replaced by the $(3,3)$ scalar element of the transformed matrix (I_z). As a result, the scalar nonlinear time varying differential equation for A_g may be written as:

$$\ddot{A}_g + \frac{C}{I_z}\dot{A}_g + \frac{\lambda}{I_z}A_g = \frac{T}{I_z} \tag{3.32}$$

The output of the vibrating comb gyroscope has been completely defined in terms of a second order differential equation. In addition, the resulting equation for A_g may be directly compared to other rate gyroscope output equations.

3.2 Planar Gyroscope

In this section the planar gyroscope, shown in Figure 3.7, is analyzed. The planar gyroscope operates by establishing a sustained oscillation about the device's outer gimbal. When the device is subjected to an input rotation a output oscillation is established about the inner gimbal. The torque equations are generated and differential equations for output oscillations are derived for a single input about the device's sensitive axis. A complete derivation for an arbitrary input rotation is completed in Appendix B. In order to analyze the torque generated about the output axis, the torque generated by each of the four mass centers must be calculated. The four position vectors, basis, and system origin are defined in Figure 3.8. The corresponding position vectors are given in Equations (3.33-3.36).

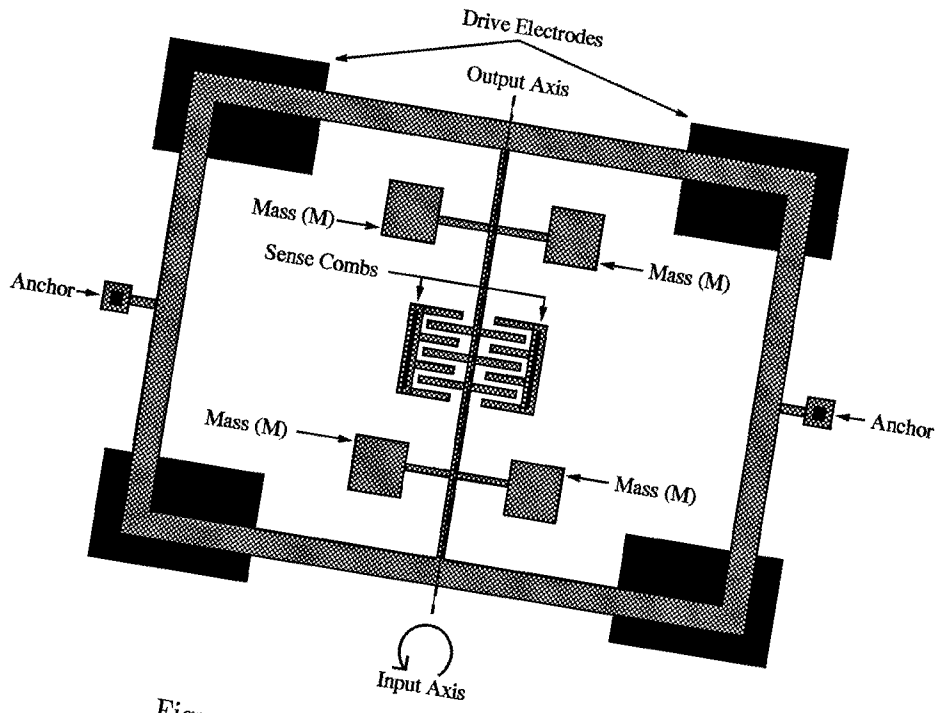

Figure 3.7 Planar gyroscope illustration.

$$R_1 = \begin{bmatrix} D \\ -R \\ 0 \end{bmatrix} \tag{3.33}$$

$$R_2 = \begin{bmatrix} D \\ R \\ 0 \end{bmatrix} \tag{3.34}$$

$$R_3 = \begin{bmatrix} -D \\ R \\ 0 \end{bmatrix} \tag{3.35}$$

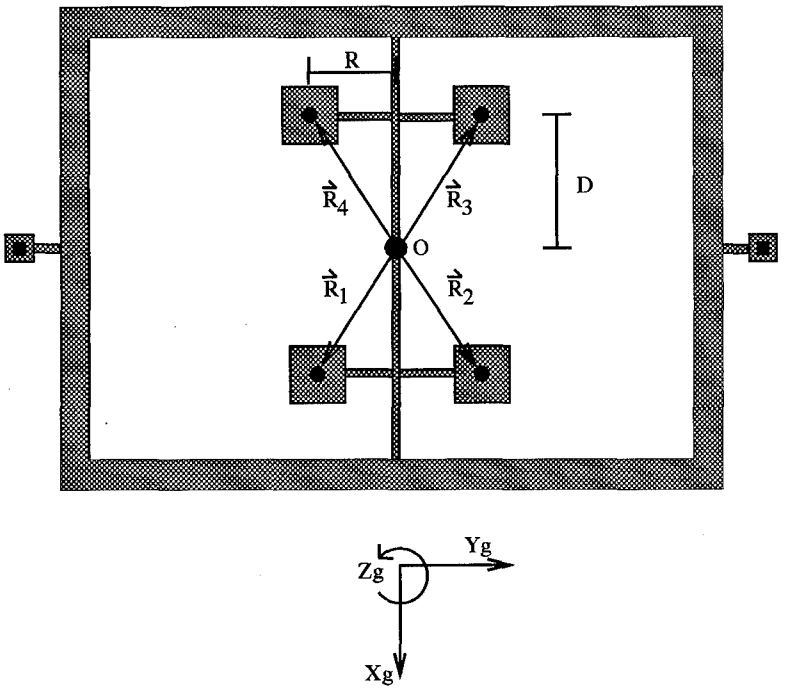

Figure 3.8 Planar gyroscope block diagram.

$$R_4 = \begin{bmatrix} -D \\ -R \\ 0 \end{bmatrix} \tag{3.36}$$

The gyroscope is subjected to a sustained oscillation about the y_g axis. This oscillation is defined by Equation (3.37).

$$\Delta y = \Omega sin(\omega t)\hat{y}_g \tag{3.37}$$

where Δy is the change in position about the y axis. For an input rotation of ω_z about the z_g axis, the rotation rate of each of the mass centers is given in Equation (3.38):

$$\vec{\omega} = \begin{bmatrix} 0 \\ 0 \\ \omega_z \end{bmatrix} \tag{3.38}$$

This results in a rotation rate of $\vec{\omega}$ with respect to inertial space given in Equation (3.39). This rotation rate has components due to the input rotation and the sustained oscillation.

$$\vec{\omega} = \begin{bmatrix} 0 \\ \omega\Omega cos(\omega t) \\ \omega_z \end{bmatrix} \tag{3.39}$$

Using the above definitions, the accelerations of each of the mass centers is calculated and given by Equations (3.40-3.43):

$$A_1 = [R\dot{\omega}_z - D\omega^2\Omega^2 cos^2(\omega t) + D\omega_z^2]\hat{x}_g + [-D\dot{\omega}_z - R\omega_z^2]\hat{y}_g$$
$$+[(-D\dot{\omega} - R\omega_z\omega)\Omega cos(\omega t) + D\omega\Omega sin(\omega t)]\hat{z}_g \tag{3.40}$$

$$A_2 = [-R\dot{\omega}_z - D(\omega\Omega cos(\omega t))^2 + \omega_z^2 D]\hat{x}_g + [-D\dot{\omega}_z + R\omega_z^2]\hat{y}_g$$
$$+[(-D\dot{\omega} + R\omega_z\omega)\Omega cos(\omega t) + D\omega^2\Omega sin(\omega t)]\hat{z}_g \tag{3.41}$$

$$A_3 = [-R\dot{\omega}_z + D\omega^2\Omega^2 cos^2(\omega t) - D\omega_z^2]\hat{x}_g + [D\dot{\omega}_z + R\omega_z^2]\hat{y}_g$$
$$+[(D\dot{\omega} + R\omega_z\omega)\Omega cos(\omega t) - D\omega^2\Omega sin(\omega t)]\hat{z}_g \tag{3.42}$$

$$A_4 = [R\dot{\omega}_z + D\omega^2\Omega^2 cos^2(\omega t) - D\omega_z^2]\hat{x}_g + [D\dot{\omega}_z - R\omega_z^2]\hat{y}_g$$
$$+[(D\dot{\omega} - R\omega_z\omega)\Omega cos(\omega t) - D\omega^2\Omega sin(\omega t)]\hat{z}_g \quad (3.43)$$

The torques generated by each of the mass centers are given in Equations (3.44-3.47):

$$T_1 = m[[DR\dot{\omega}\Omega cos(\omega t) - DR\omega^2\Omega sin(\omega t) + R^2\omega_z\omega\Omega cos(\omega t)]\hat{x}_g$$
$$+[-D^2\dot{\omega}\Omega cos(\omega t) + D^2\omega^2\Omega sin(\omega t) - DR\omega_z\omega\Omega cos(\omega t)]\hat{y}_g$$
$$+[-D^2\dot{\omega}_z + R^2\dot{\omega}_z - DR(\omega\Omega cos(\omega t))^2]\hat{z}_g] \quad (3.44)$$

$$T_2 = m[[-DR\dot{\omega}\Omega cos(\omega t) + DR\omega^2\Omega sin(\omega t) + R^2\omega_z\omega\Omega cos(\omega t)]\hat{x}_g$$
$$+[-D^2\dot{\omega}\Omega cos(\omega t) + D^2\omega^2\Omega sin(\omega t) + DR\omega_z\omega\Omega cos(\omega t)]\hat{y}_g$$
$$+[-D^2\dot{\omega}_z + R^2\dot{\omega}_z + DR(\omega\Omega cos(\omega t))^2]\hat{z}_g] \quad (3.45)$$

$$T_3 = m[[DR\dot{\omega}\Omega cos(\omega t) - DR\omega^2\Omega sin(\omega t) + R^2\omega_z\omega\Omega cos(\omega t)]\hat{x}_g$$
$$+[-D^2\dot{\omega}\Omega cos(\omega t) + D^2\omega^2\Omega sin(\omega t) - DR\omega_z\omega\Omega cos(\omega t)]\hat{y}_g$$
$$+[-D^2\dot{\omega}_z + R^2\dot{\omega}_z - DR(\omega\Omega cos(\omega t))^2]\hat{z}_g] \quad (3.46)$$

$$T_4 = m[[-DR\dot{\omega}\Omega cos(\omega t) + DR\omega^2\Omega sin(\omega t) + R^2\omega_z\omega\Omega cos(\omega t)]\hat{x}_g$$
$$+[-D^2\dot{\omega}\Omega cos(\omega t) + D^2\omega^2\Omega sin(\omega t) + DR\omega_z\omega\Omega cos(\omega t)]\hat{y}_g$$
$$+[-D^2\dot{\omega}_z + R^2\dot{\omega}_z + DR(\omega\Omega cos(\omega t))^2]\hat{z}_g] \quad (3.47)$$

The net torque is found by summing each of the individual torques at the origin. The resulting net torque is shown in Equation (3.48):

$$T_{net} = 4m[[R^2\omega_z\omega\Omega cos(\omega t)]\hat{x}_g + [-D^2\dot{\omega}\Omega cos(\omega t) + D^2\omega^2\Omega sin(\omega t)]\hat{y}_g + [-D^2\dot{\omega}_z + R^2\dot{\omega}_z]\hat{z}_g \tag{3.48}$$

It may be seen by the final torque equation that the structure as shown in Figure 3.7 is not the best structure. The net torque equation shows the effect of placing the mass centers off a line connecting the outer gimballs results in a reduction in the net torque. A structure with a single dumbell like mass placement along the line connecting the outer gimballs of the device would result in a larger output torque. This may be shown by letting D in Equation (3.48) equal to zero.

3.3 Vibrating Ring Gyroscope

The theory for the third gyroscope, the ring gyroscope, was first developed by Michael Putty in his dissertation at the University of Michigan [10]. The devices developed by Dr. Putty were constructed by electroforming nickel to generate high aspect ratios and allow for plate capacitors to be used to drive and sense the flexural modes of the device. In this thesis, the study is limited to use of a standard polysilicon surface micromachining process (MUMPS). The aspect ratio in the MUMPS process is limited requiring new drive and sense mechanisms. The basic ring structure evaluated in this thesis is the same as Dr. Putty's, making most of the device theory the same. Changes to the sense and drive mechanisms make the calculation of the electrical potential energy unique. As a result of the similarities, Dr. Putty's dissertation is used extensively as a reference. The ring

structure to be analyzed is shown in Figure 3.9. The device is suspended off the substrate

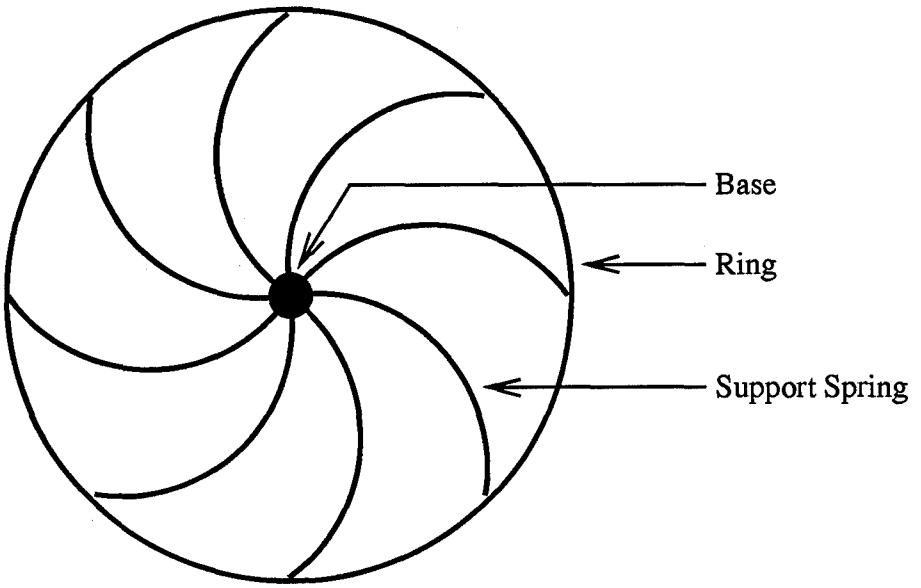

Figure 3.9 Basic structure of the ring gyroscope.

by the central support post, or base, and then driven at its flexural resonant frequency. The resonant mode of interest is the second order mode resulting in two elliptically shaped resonant patterns shown in Figure 3.10. In order to describe the device behavior normal mode equations were developed by applying Lagrange's equation (3.49):

$$\frac{d}{dt}\left(\frac{\partial T}{\partial \dot{q}_i}\right) + \frac{\partial T}{\partial q_i} + \frac{\partial U}{\partial q_i} = Q_i \tag{3.49}$$

Where T is the kinetic energy of the system, U is the potential energy, and Q is the generalized force found from the amount of work, ∂W, to perform a virtual displacement, ∂q [34]. The analysis results in a set of coupled second order differential equations. The analysis relies on the fact that a complex vibrational displacement, u, may be written as a linear combination of its normal mode displacements, Φ_i, with complex amplitudes, q_i,

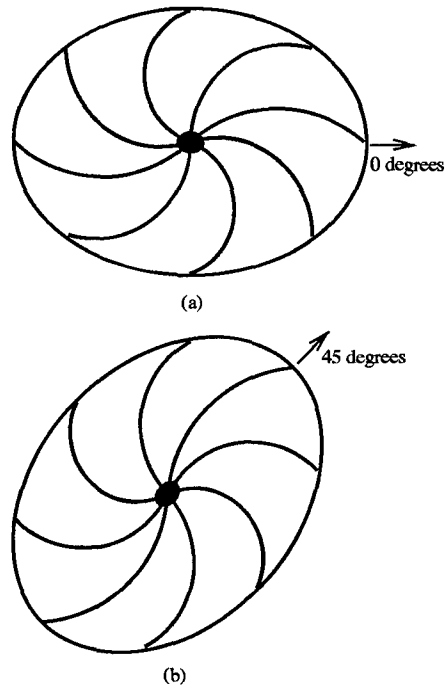

Figure 3.10 Flexural vibrations in a ring gyroscope; (a) primary vibrational mode (b) secondary vibrational mode.

as given by Equation (3.50):

$$u = \sum_{i=1}^{n} \Phi_i q_i \tag{3.50}$$

Vibrational modes other than the two fundamental flexural modes contribute only minor second order effects; as a result they are not included in the device model.

It is now necessary to define the coordinates used in the analysis: Figure 3.11 defines the x and y directions; Figure 3.12 defines the generalized coordinates that give the complex amplitude of the two flexural modes; and Figure 3.13 defines the generalized coordinates used to calculate the generalized force Q_i in Lagrange's equations. The first generalized coordinate, q_1, is located an angle of θ_o counter-clockwise from the $\hat{x}$ direction and the q_2 direction is 45 degrees past the q_1 direction. The angle θ_τ defines the location of the q_1'

direction. The vibrational displacement may then be described in terms of its x and y

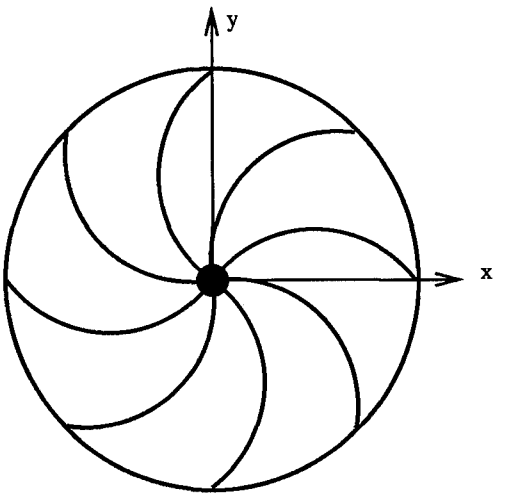

Figure 3.11 Definition of the x and y coordinate directions.

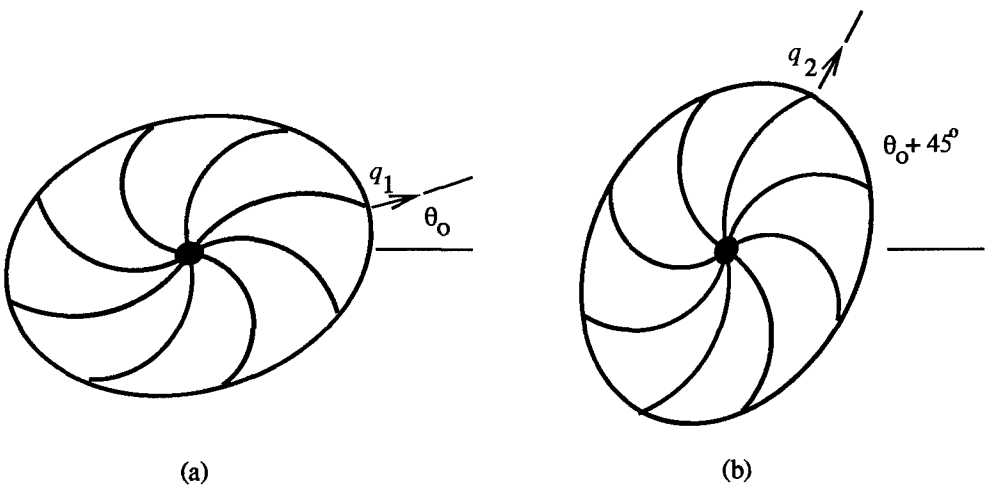

Figure 3.12 (a) definition of the q_1 coordinate direction (b) definition of the q_2 coordinate direction

displacements, u_x and u_y, its mode shape functions for the x displacement, Φ_{x1} and Φ_{x2}, its mode shape functions for the y displacement, Φ_{y1} and Φ_{y2}, and coordinatized in terms of the generalized direction vectors q_1 and q_2. Equations (3.51)(3.52) define the u_x and u_y

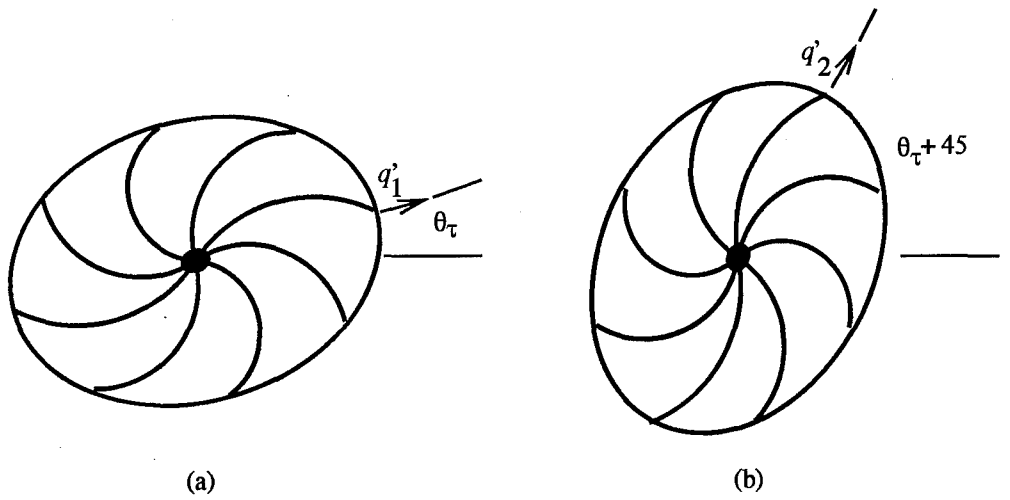

Figure 3.13 (a) definition of the q_1' coordinate direction (b) definition of the q_2' coordinate direction.

displacements:

$$u_x = \Phi_{x1} q_1 + \Phi_{x2} q_2 \tag{3.51}$$

$$u_y = \Phi_{y1} q_1 + \Phi_{y2} q_2 \tag{3.52}$$

To facilitate the analysis further, the ring will be broken up into nine parameterized segments, one for the ring itself and eight for the support springs. Figure 3.14 shows the parameterization for each of the elements in terms of the x and y directions. Applying these parameter definitions to Equations (3.53)(3.54) and adding the parameter p, the final x and y displacement functions may be written as in Equations (3.53 and 3.54).

$$u_x(p) = \Phi_{x1}(p) q_1 + \Phi_{x2}(p) q_2 \tag{3.53}$$

$$u_y(p) = \Phi_{y1}(p) q_1 + \Phi_{y2}(p) q_2 \tag{3.54}$$

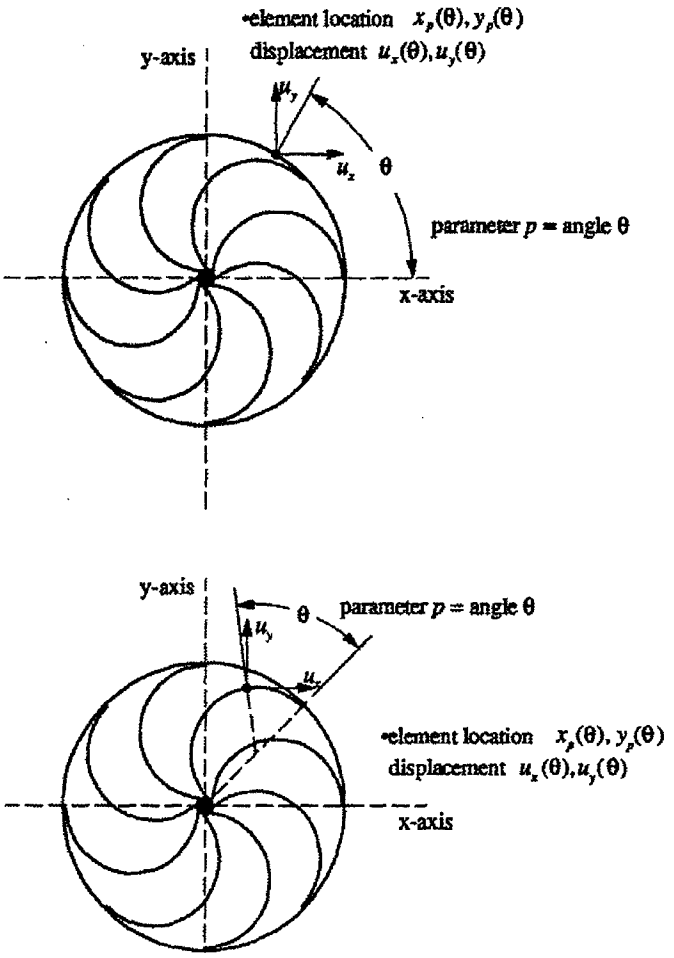

Figure 3.14 Ring gyroscope parameterization [10]. In the upper portion of the figure the parameter θ represents the location of a point on the ring. In the lower portion θ represents the location of a point along one of the semi-circular support springs.

In order to apply Lagrange's equations to this system, it is necessary to calculate the kinetic energy, potential energy, and generalized force. The following sections complete these calculations.

3.3.1 Kinetic Energy. The derivation of the kinetic energy of the system was completed by Michael Putty in his dissertation [10]. The definitions necessary are provided along with the results of the analysis. Let the ring structure be located in a reference frame OXYZ at $r_a = x_a\hat{x} + y_a\hat{y}$ (see Figure 3.15). Let the OXYZ frame be rotating with a rate of $\omega = (\Omega_x, \Omega_y, \Omega_z)$ and translating with respect to an inertial frame $O_oX_oY_oZ_o$ with a velocity of $v_o = v_{xo}\hat{x} + v_{yo}\hat{y} + v_{zo}\hat{z}$. The kinetic energy is determined by calculating the inertial

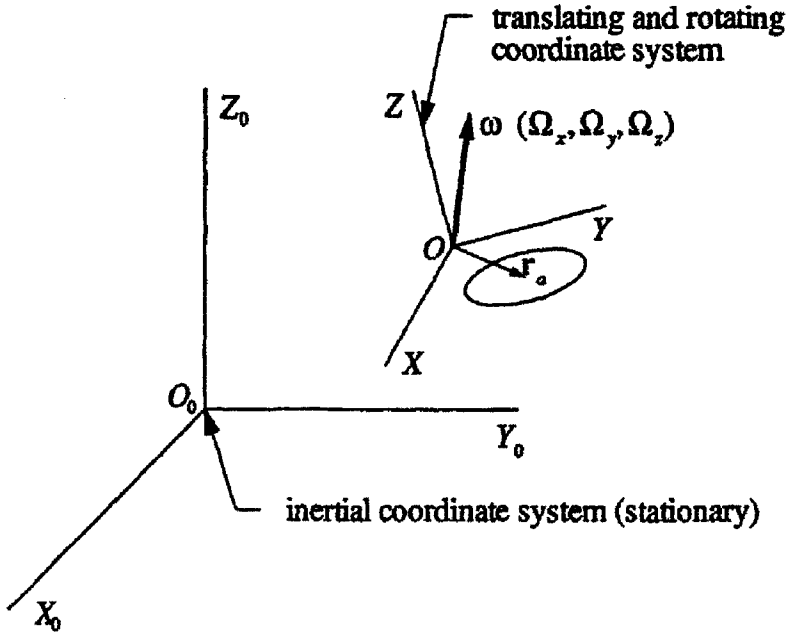

Figure 3.15 Coordinate definitions for kinetic energy derivation [10].

velocity and finding its magnitude squared, multiplying by the density of the material ρ,

and integrating over the volume of the device. The resulting equation is shown in Equation (3.55):

$$T = \frac{1}{2}\int_V \rho |v|^2 dV \tag{3.55}$$

After the integration is performed, the equation is simplified and the definitions of the small x and y displacements are substituted into the equation. The result is given in Equation (3.56):

$$T = \frac{1}{2}M_1\dot{q}_1^2 + \frac{1}{2}M_2\dot{q}_2^2 + \Omega_z\gamma(q_1\dot{q}_2 - q_2\dot{q}_1) + \frac{1}{2}(\Omega_x^2\beta_1 + \Omega_y^2\alpha_1 + \Omega_z^2\mu_1)q_1^2 + \frac{1}{2}(\Omega_x^2\beta_2 + \Omega_y^2\alpha_2 + \Omega_z^2\mu_2)q_2^2 \tag{3.56}$$

where

$$M_1 = \int_V \rho[\Phi_{x1}^2 + \Phi_{y1}^2]dV$$

$$M_2 = \int_V \rho[\Phi_{x2}^2 + \Phi_{y2}^2]dV$$

$$\gamma = \int_V \rho[\Phi_{x1}\Phi_{y1} - \Phi_{x2}\Phi_{y2}]dV$$

$$\beta_1 = \int_V \rho\Phi_{y1}^2 dV$$

$$\beta_2 = \int_V \rho\Phi_{y2}^2 dV$$

$$\alpha_1 = \int_V \rho\Phi_{x1}^2 dV$$

$$\alpha_2 = \int_V \rho\Phi_{x2}^2 dV$$

$$\mu_1 = \int_V \rho[\Phi_{x1}^2 + \Phi_{y1}^2]dV$$

$$\mu_2 = \int_V \rho[\Phi_{x2}^2 + \Phi_{y2}^2]dV$$

It is important to note that, in the second term of the kinetic energy equation, the Coriolis coupling depends only on the rotation about the device sensitive axis. It should also be noted that the kinetic energy is independent of the location of the ring and the translational velocity of the moving frame. This shows the independence of mounting location and, to first order, insensitivity to linear accelerations. This completes the kinetic energy analysis; it is necessary next to derive the potential energy of the system.

3.3.2 Potential Energy. The potential energy terms may be broken up into two categories, the mechanical energy, U_m, of the ring's differential elements, and the electrical potential energy, U_e. The mechanical potential energy of the ring gyroscopes designed for this thesis is identical to the mechanical potential energy derived by Putty in his dissertation. The electrical potential energy, however, is unique to these devices. The mechanical potential of the ring is given by Equation (3.57).

$$U_m = \frac{1}{2}K_1 q_1^2 + \frac{1}{2}K_2 q_2^2 \tag{3.57}$$

$$K_1 = EI \int_p \frac{[\dot{x}_p \ddot{\Phi}_{y1} - \dot{y}_p \ddot{\Phi}_{x1} + \ddot{y}_p \dot{\Phi}_{x1} - \ddot{x}_p \dot{\Phi}_{y1}]^2}{[\dot{x}_p + \dot{y}_p]^{\frac{3}{2}}} dp \tag{3.58}$$

$$K_2 = EI \int_p \frac{[\dot{x}_p \ddot{\Phi}_{y2} - \dot{y}_p \ddot{\Phi}_{x2} + \ddot{y}_p \dot{\Phi}_{x2} - \ddot{x}_p \dot{\Phi}_{y2}]^2}{[\dot{x}_p + \dot{y}_p]^{\frac{3}{2}}} dp \tag{3.59}$$

The electrical potential energy, U_e, is analyzed via the specific electrode sets affecting the ring. Specifically, the electrical potential energy may be separated into the energy from the drive electrodes (U_d), sense electrodes (U_s), and from the remaining electrode sets (U_g). The electrical potential energy is dependent on the size and shape of the electrodes. In the case of the ring gyroscope developed at the University of Michigan, the ring had flat

faces interfacing with flat electrodes. This was possible because of the thickness of their structures, 25μm, compared to the maximum thickness from the MUMPS process of 3.5μm. As a result, the drive and sense electrodes are constructed from a series of interdigitated combs (Figures 3.16 and 3.17). There are one fixed comb and a comb attached to the ring that make up a single electrode.

The potential energy of the system may be expanded and written as a linear combination of the potentials from each electrode set; this is shown in Equation (3.60):

$$U_e = U_d + U_s + U_g \tag{3.60}$$

U_d, U_s, and U_g are replaced with their definitions in equation 3.61

$$U_e = \underbrace{-\sum_{n=1,5} \frac{1}{2} V_n^2 C_n}_{drive} \underbrace{-\sum_{n=2,6} \frac{1}{2} V_n^2 C_n}_{sense} \underbrace{-\sum_{n=3,4,7,8} \frac{1}{2} V_n^2 C_n}_{ground} \tag{3.61}$$

In Equation (3.61) the subscripts on the summations refer to the electrode numbers assigned in Figure 3.16, V_n is the total voltage applied to the electrode, and C_n represents the capacitance generated by the interaction between the electrode and the ring. The derivation of each capacitance for each of the eight electrodes is the same, as a result the analysis will be completed for one electrode and then substituted into Equation (3.60). The capacitance is calculated by assuming infinitely small parallel plate capacitors in parallel. This reduces the capacitance equation to an integral form. Figure 3.17 shows a single electrode and ring interface. Let the initial finger overlap length be defined as L and the nominal position be defined as d_o. The change in capacitance may be written in terms of

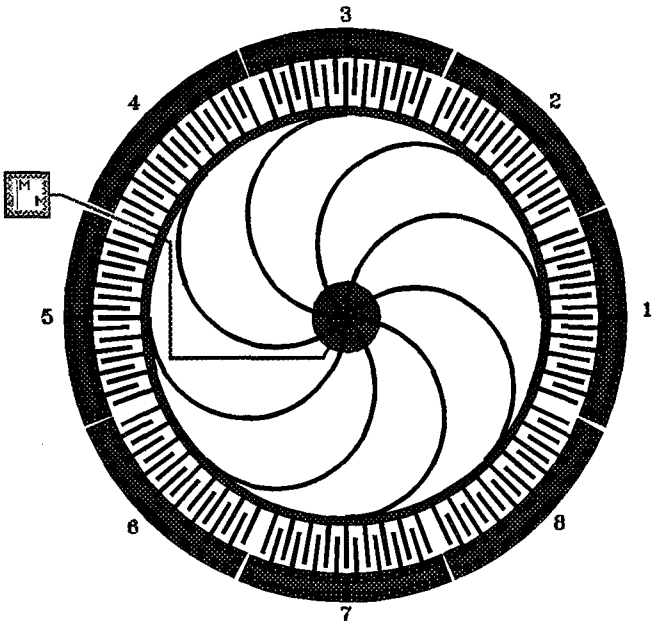

Figure 3.16 Electrode location definitions.

the small displacements u_x and u_y. Figure 3.18 shows the interface between one ring finger and two of the electrode fingers. It is necessary to integrate along the finger from its start to the end of the overlap. Let the end of the stationary electrode finger be defined as zero. The change in overlap distance is then defined by Equation (3.62):

$$|u_x|cos(\theta) + |u_y|cos(90^o - \theta) \tag{3.62}$$

the magnitudes of the x displacement and the y displacement must be found by applying the law of cosines because of the non-orthogonality of the q_1 and q_2 directions. In general the magnitude of u_x may be written as in Equation (3.63) and the magnitude of u_y may be written as in Equation (3.64):

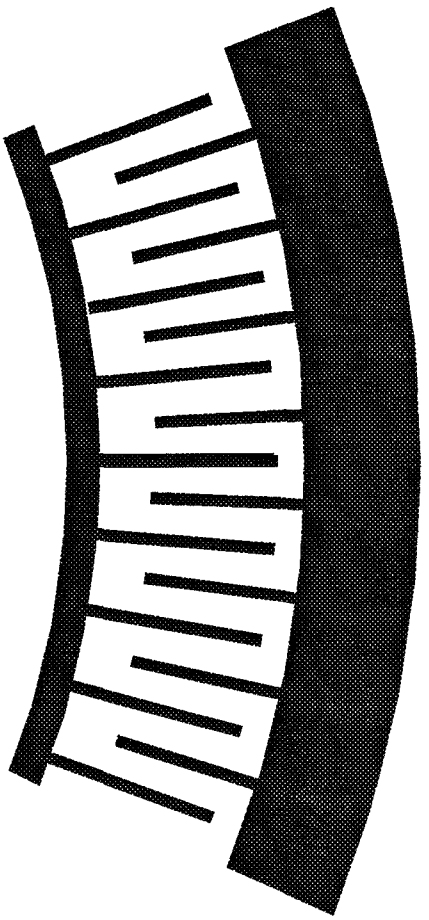

Figure 3.17 Single ring gyroscope electrode.

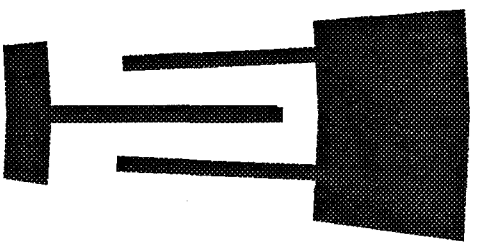

Figure 3.18 A single ring finger and its stationary electrode counterparts.

$$|u_x| = \sqrt{\Phi_{x1}(\theta)^2 + \Phi_{x2}(\theta)^2 - 2\Phi_{x1}(\theta)\Phi_{x2}(\theta)cos(135^o)} \tag{3.63}$$

$$|u_y| = \sqrt{\Phi_{y1}(\theta)^2 + \Phi_{y2}(\theta)^2 - 2\Phi_{y1}(\theta)\Phi_{y2}(\theta)cos(135^o)} \tag{3.64}$$

The total overlap at any time instant then becomes:

$$L = |u_x|cos(\theta) + |u_y|cos(90^o - \theta) \tag{3.65}$$

In order for the overlap distance to be used, L must be defined in terms of the generalized coordinates q_1 and q_2. By applying the law of sines to a vector of magnitude L located at an angle of θ, the vector $\vec{L}$ expressed in terms of the generalized coordinates is given by Equation (3.66):

$$\vec{L} = \frac{Lsin(45^o + \theta_o - \theta)}{sin(135^o)}q_1 + \frac{Lsin(\theta - \theta_o)}{sin(135^o)}q_2 \tag{3.66}$$

and the capacitance from one ring finger is defined by the integral:

$$C = \int_0^{\vec{L}} \left[\frac{\epsilon t}{d_o + \Delta d} + \frac{\epsilon t}{d_o - \Delta d}\right] dl \tag{3.67}$$

where, ϵ is the permeativity of the medium and t is the layer thickness, d_o is the initial stationary to free electrode spacing, and Δd is the change in spacing from the stationary to the free elctrode. The first term inside the integral comes from the stationary electrode above the moving electrode and the second comes from the lower electrode. If either of the stationary combs is missing (e.g., at the ends of the electrode), the corresponding term

may be omitted. When both stationary fingers are present, the integral simplifies to:

$$C = \int_0^{\vec{L}} \frac{2\epsilon t d_o}{d_o^2 + \Delta d^2} dl \tag{3.68}$$

A McLaurin series expansion is used about Δd to linearize this equation. This simplifies the integral to:

$$C = \int_0^{\vec{L}} \frac{2\epsilon t}{d_o} \tag{3.69}$$

Evaluating the integral yields the capacitance due to one moving finger surrounded by two stationary fingers:

$$C = \frac{2\epsilon t \vec{L}}{d} \tag{3.70}$$

It is also necessary to calculate the result for the upper stationary electrode being present only, and for just the lower stationary electrode as well. The result of completing the analysis for the upper electrode only is:

$$C_u = \frac{\epsilon t}{d} \int_0^{\vec{L}} dl - \frac{\epsilon t}{d^2} \int_0^{\vec{L}} \Delta d dl + \frac{\epsilon t}{d^3} \int_0^{\vec{L}} \Delta d^2 dl \tag{3.71}$$

The result for only the lower electrode being present is:

$$C_l = \frac{\epsilon t}{d} \int_0^{\vec{L}} dl + \frac{\epsilon t}{d^2} \int_0^{\vec{L}} \Delta d dl - \frac{\epsilon t}{d^3} \int_0^{\vec{L}} \Delta d^2 dl \tag{3.72}$$

Where Δd is defined as in the direction of increasing θ and is related to the u_x and u_y displacements by Equation (3.73):

$$|\Delta d| = |u_x| sin(\theta) + |u_y| cos(\theta) \tag{3.73}$$

In order to maintain consistency, it is necessary to write a vector $\vec{\Delta d}$ in terms of q_1 and q_2. This is given in Equation (3.74)

$$\vec{\Delta d} = -|\Delta d| cos(90^\circ - \theta + \theta_o) q_1 + |\Delta d| cos(45^\circ + \theta - \theta_o) q_2 \tag{3.74}$$

The capacitance for an electrode is found by summing the individual effects of the ring fingers. The effects are dependent on time and the angular location of the finger. Using the definitions above, the capacitance for the nth electrode may be written as shown in Equation (3.75).

$$C_n = \frac{7(2\epsilon t)\vec{L}}{d} + C_u + C_l \tag{3.75}$$

The potential energy may now be written as a function of the ring's mode shapes. The mode shapes for the analysis must come from a finite element analysis tool. The use of these tools is beyond the scope of this thesis; as a result a closed form solution for the potential energy of the system is not included. Investigation of a closed form solution for these mode shapes and a finite element analysis of the other gyroscopes investigated provides an excellent opportunity for future research. The Nastran finite element package available at AFIT would be an ideal package to use. The last piece needed to implement Lagrange's equations is the generalized force Q.

3.3.3 Generalized Force. The non-conservative forces rise mainly from damping, both material damping and viscous damping. The generalized force Q is a function of the amount of work ∂W necessary to create a virtual displacement ∂q, and is defined in terms of the q_1' and q_2' coordinates by Equations (3.76) and (3.77):

$$Q_{1'} = \frac{\partial W}{\dot{q}_{1'}} = -C_1 \dot{q}_{1'} \tag{3.76}$$

$$Q_{2'} = \frac{\partial W}{\dot{q}_{2'}} = -C_2 \dot{q}_{2'} \tag{3.77}$$

C_1 and C_2 are the independent damping coefficients. In order to maintain consistency, the q_1' and q_2' coordinates must be translated into the q_1 and q_2 coordinates. The results of this coordinate transformation are given below:

$$\begin{aligned} Q_1 = &-[C_1 cos^2(2\phi) + C_2 sin^2(2\phi)]\dot{q}_1 \\ &-[(C_1 - C_2)cos(2\phi)sin(2\phi)]\dot{q}_2 \end{aligned} \tag{3.78}$$

$$\begin{aligned} Q_2 = &-[(C_1 - C_2)cos(2\phi)sin(2\phi)]\dot{q}_1 \\ &-[C_1 cos^2(2\phi) + C_2 sin^2(2\phi)]\dot{q}_2 \end{aligned} \tag{3.79}$$

Where ϕ is defined as :

$$\phi = \theta_\tau + \theta_0 \tag{3.80}$$

The damping accounts for the loss of energy in the system due to damping both in the material and due to viscous damping in the air. This completes the evaluation of the terms necessary to implement Lagrange's equations.

In this section the ring gyroscope was analyzed using a work energy approach. Because of design choices, the electrode capacitance is not a simple function of radial displacement; instead it is a function of a linear combination of the mode shape functions. The complexity of the structure makes it necessary to use a finite analysis program to attain the mode shape functions. The difficulty in learning these tools makes this analysis beyond the scope of this thesis.

3.4 Chapter Summary

In this chapter the theory of operation for the three gyroscopes investigated was developed. Versions of each gyroscope were designed and fabricated. In the following chapter each of the designs is discussed and experimental procedures are recorded.

IV. Experimental Approach and Procedures

In the previous chapter a theoretical derivation was completed for the operation of three types of mechanical gyroscopes. Each of the gyroscopes was then fabricated. The purpose of this chapter is to describe the resulting designs and their testing. The designs will be discussed in the order of creation. There were four fabrication runs: MUMPS 6, MUMPS 7, MUMPS 8 and MUMPS 9. The submission date of each run is given in Table 4.1 below. Sections 4.1 - 4.9 describe the designs included on each of the fabrication runs and provide the statistics specific to each run. The variables that were assumed constant over all the fabrication runs are provided in Table 4.2. The device descriptions are followed by the experimental set-ups and procedures used to test for device resonant frequency characteristics.

Table 4.1 Fabrication Dates For MUMPS Runs.

Run Name	Due Date
MUMPS 6	1 Dec 94
MUMPS 7	28 Feb 95
MUMPS 8	8 May 95
MUMPS 9	14 Aug 95

Table 4.2 Common Design parameters.

Parameter Name	Symbol	Value
Density	ρ	2330 $\frac{g}{cm^3}$
Young's Modulus	E	160 MPa
Poisons Ratio	v	0.23-0.3

4.1 MUMPS 6

The MUMPS 6 fabrication run statistics are given in Table 4.3. In that table, the

Table 4.3 MUMPS 6 Fabrication Statistics.

Film	Thickness (A)	Stress (MPa)	Resistivity (ohm-cm)
poly 0	5200	19.7 (C)	1.84E-3
poly 1	20220	5.1 (C)	2.58E-3
poly 2	15650	5.1 (C)	2.72E-3
metal (Cr/Au)	5540	30 (T)	3.39E-6
nitride	6213	19.2 (T)	–
oxide 1	20151	–	–
oxide 2	5230	–	–

stress of the layer is followed by a C or a T; C represents a compressive stress and T a tensile stress. The dashes indicate values not computed. The nitride layer acts as an isolation layer so its resistivity is very high. The two oxide layers are the sacrificial layers of the process. These layers provide spacing between mechanical layers and are removed once the structure is released. MUMPS 6 was the first fabrication run used in this thesis and device theory was under initial investigation. There were two classes of devices created. The first was a vibrating comb gyroscope. In order to maximize the output of this gyroscope, a multi-layer structure was investigated, using different flexure and support lengths. Figure 4.1 shows the device as created. In addition the legend attached to all Scanning Electron Microscope (SEM) photos is labelled. The multilayer structure was created strictly adhering to the MUMPS process design rules given in Table 2.3. As a result, the device is not symmetric in the vertical direction. A cross section of the resulting structure is shown in Figure 4.2. As the comb gyroscope theory matured, it became obvious that this type of device was not ideal. The asymmetric nature of the vibrating plates lends itself to twisting under normal operation. As a result, an output will be seen for a zero input rotation. In addition, the sense capacitance is too small to provide a reliable signal. There were also initial planar

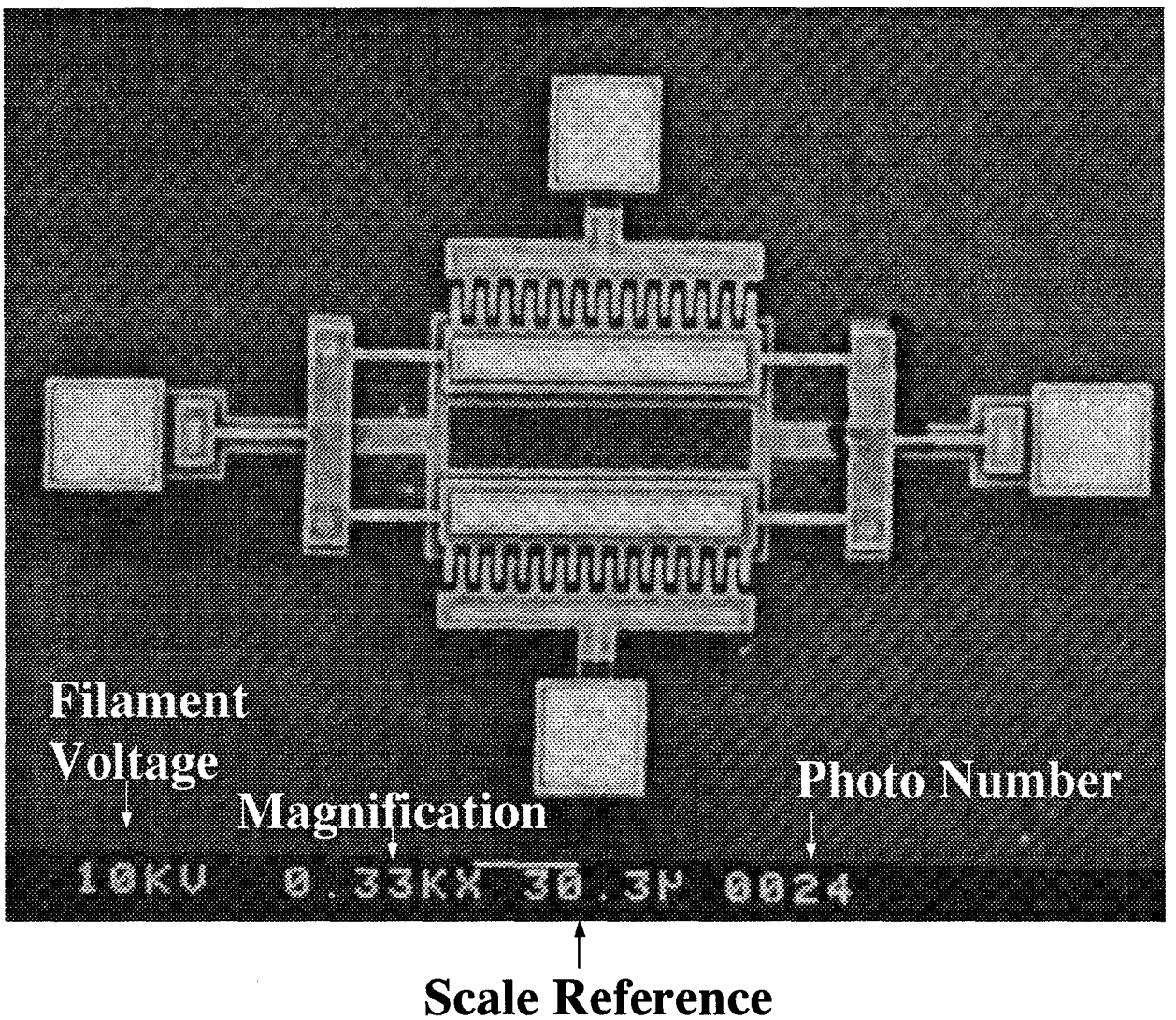

Figure 4.1 Initial comb gyroscope design. The legend attached to all Scanning Electron Microscope Photographs is labelled.

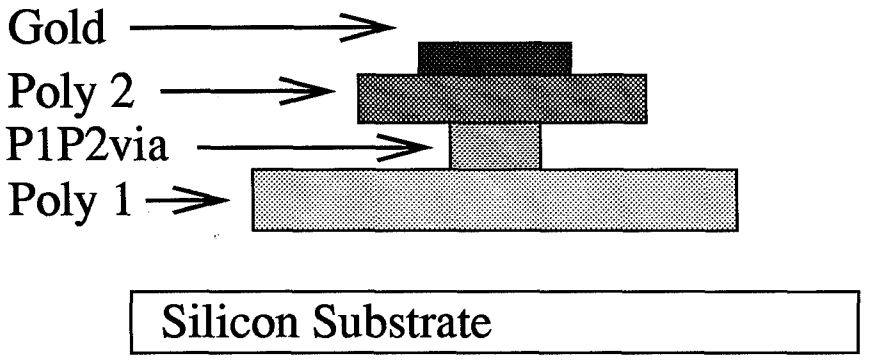

Figure 4.2 Initial comb gyroscope design cross section.

gyroscope designs included on this fabrication run, but layout errors in these designs made them unusable.

4.2 MUMPS 7

The characteristics of the MUMPS 7 fabrication run are given in Table 4.4. Versions

Table 4.4 MUMPS 7 Fabrication Statistics.

Film	Thickness (A)	Stress (MPa)	Resistivity (ohm-cm)
poly 0	4880	–	2E-3
poly 1	20100	8.0 (C)	1.65E-3
poly 2	14706	11.1 (C)	1.54E-3
metal (Cr/Au)	5318	21 (T)	3.30E-6
nitride	6049	41.0 (T)	–
oxide 1	20400	–	–
oxide 2	5281	–	–

of the tuning fork, ring, and planar gyroscopes were fabricated in this run. Each device is discussed in terms of its sense mechanism, drive mechanism, and design considerations.

4.2.1 Vibrating Comb Gyroscope. There were two versions of the vibrating comb gyroscope implemented in this run. The first is named comb1. This design uses combs both to drive the sustained oscillation and to sense the output oscillation. Figure 4.3 shows

the fabricated structure. Variations on this device consisted of changes in structural layer

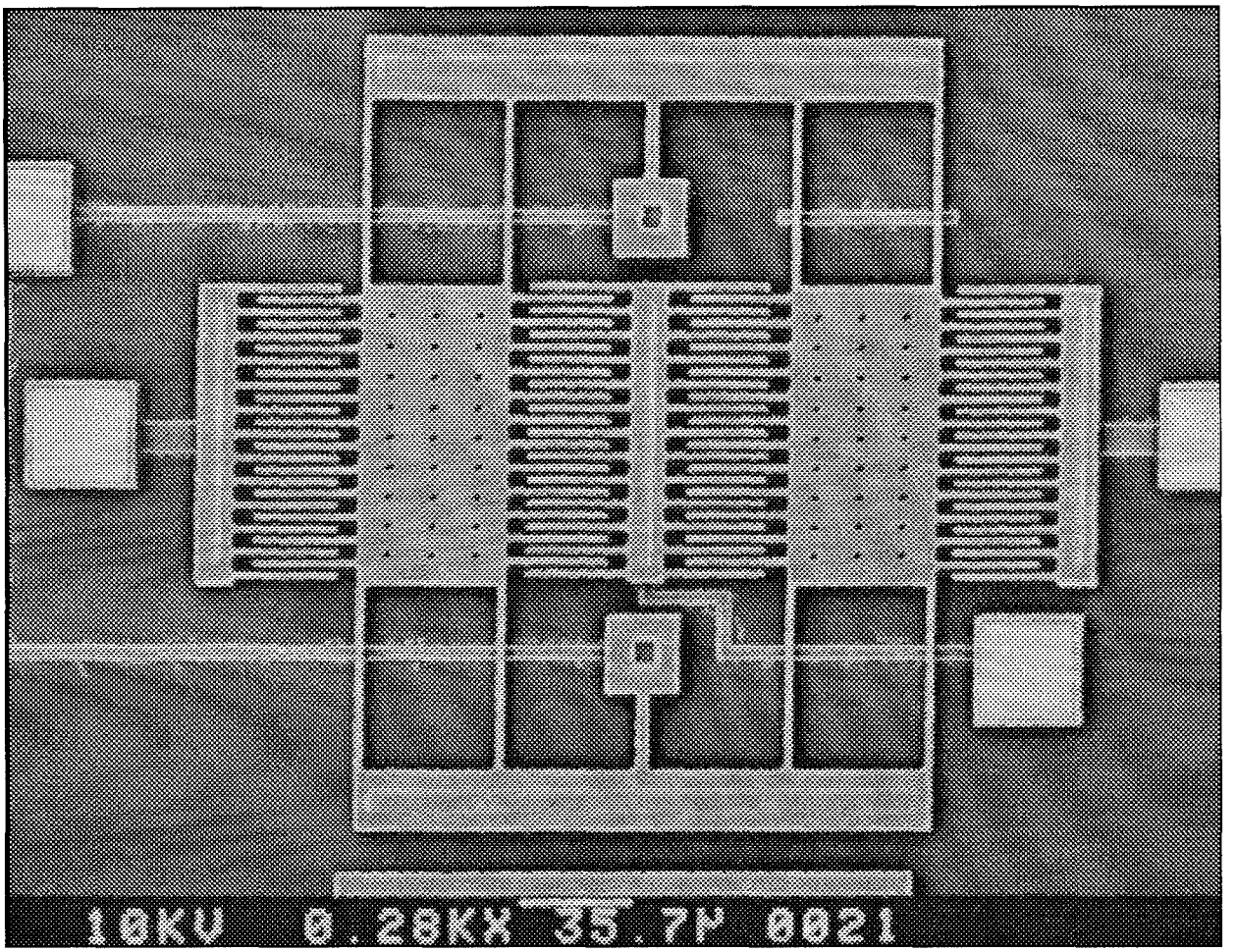

Figure 4.3 Comb1 gyroscope design in MUMPS 7.

and alterations in the width of the central support. Table 4.5 lists the specific variations and design geometry information. The variations in the dimensions of the torsion bar are intended to allow for different torsional spring constants for the output flexure. The variations should result in different device sensitivities. The device spring constant and resonant frequency are calculated by applying the equations developed in Chapter 3. The only device variation affecting the resonant frequency is the structural layer. The resonant

Table 4.5 Variations and Geometry Information for the Comb 1 Gyroscope.

Parameter	Value(s)
Structural Material	Poly 1 or Poly 2
Plate Width	50 μm
Plate Length	100 μm
Support Beam Length	60 μm
Support Beam Width	2 μm
Number of Combs	24
Comb Overlap	33 μm
Comb Length	35 μm
Torsion Bar Width	4 μm, 3 μm, 2 μm
Torsion Bar Length	25 μm, 10 μm (4 μm width only)

frequencies were calculated using a MATLAB script file, titled ksys.m; the code is provided in Appendix C. The predicted resonant frequencies are listed in Table 4.6 with each of the parameters used to calculate the resonant frequency. In Table 4.6, ksys is the system spring

Table 4.6 Comb 1 gyroscope parameters.

Parameter	Value by structural layer	
	Poly 1	Poly 2
ksys	2.192	2.211
M	2.342×10^{-11}	1.713×10^{-11}
Msup	5.620×10^{-13}	4.112×10^{-13}
Fr	48.47×10^{3}	56.92×10^{3}

constant in Kg/s^2, M is the mass of the plate and any combs attached in grams, Msup is the mass of the support springs in grams, and Fr is the device resonant frequency in Hertz. In all of the comb gyroscope designs, an array of holes may be seen. These holes ensure a complete etch of oxide from underneath the large plates, and they reduce the viscous damping in the output oscillation mode. The second design approach to the tuning fork gyroscope, named comb 2, uses a large plate capacitor as the sense mechanism. Figure 4.4 shows a fabricated device. Variations of this type of gyroscope are listed in Table 4.7. As

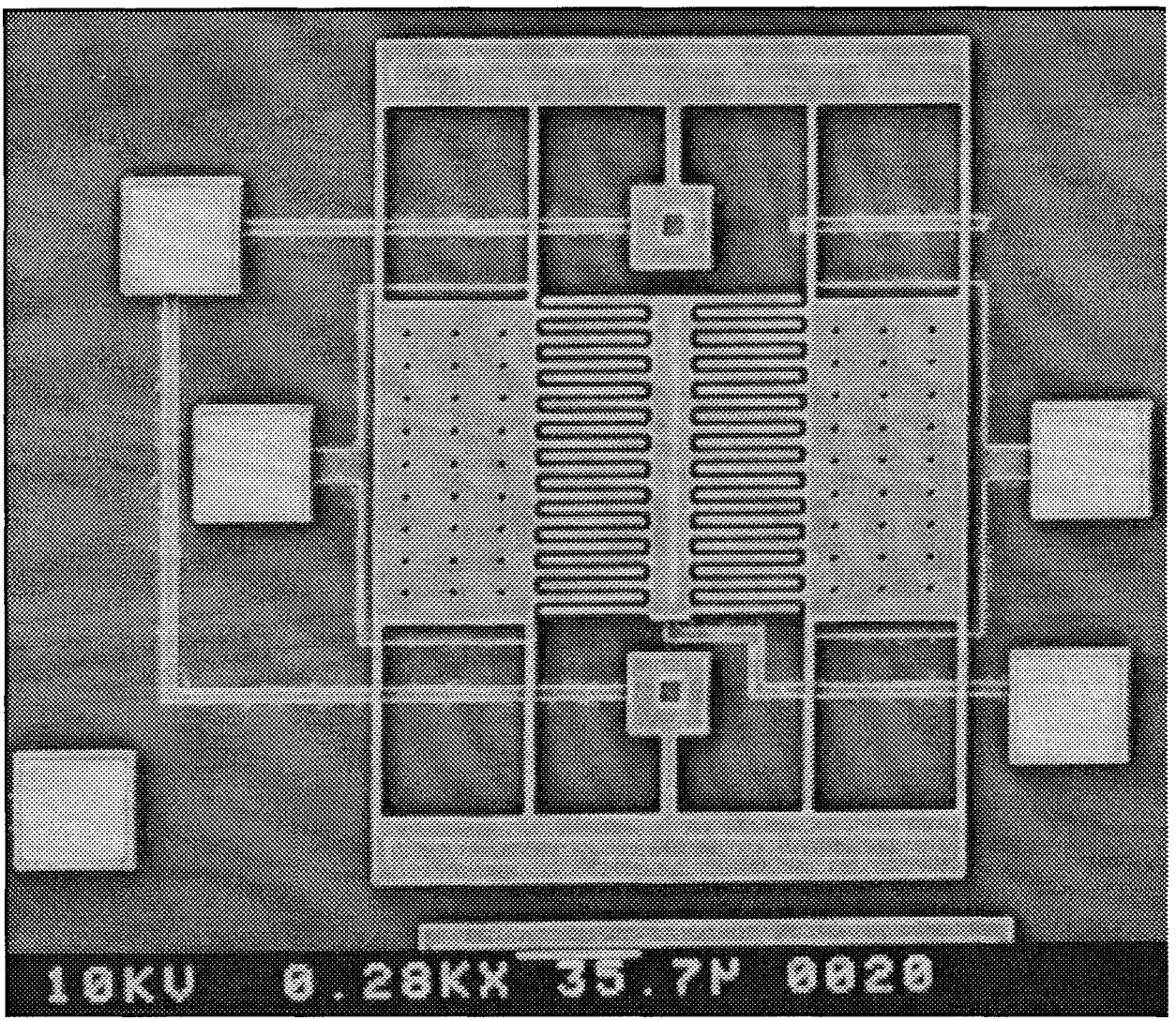

Figure 4.4 Comb2 gyroscope design In MUMPS 7.

Table 4.7 Variations and Geometry of the Comb 2 Gyroscope Design.

Parameter	Value(s)
Structural Material	Poly 1 or Poly 2
Plate Width	50 μm
Plate Length	100 μm
Support Beam Length	60 μm
Support Beam Width	2 μm
Number of Combs	12
Comb Overlap	33 μm
Comb Length	35 μm
Torsion Bar Width	4 μm, 3 μm, 2 μm
Torsion Bar Length	25 μm, 10 μm (4 μm width only)

seen from this table, the variations are the same as for the first approach and are similarly motivated. The results of running the ksys routine for this design and its variations are given in Table 4.8. The resonant frequencies from the two different designs are identical.

Table 4.8 Comb 2 gyroscope parameters.

Parameter	Value by structural layer	
	Poly 1	Poly 2
ksys	2.192	2.211
M	2.342×10^{-11}	1.713×10^{-11}
Msup	5.620×10^{-13}	4.112×10^{-13}
Fr	48.47×10^{3}	56.92×10^{3}

The additional mass contributed by the fingers in the first design is not large enough to contribute to the effective mass of the plate.

4.2.2 Planar Gyroscope. For the MUMPS 7 fabrication run, the errors in the planar gyroscope layout were corrected and the device was implemented in two main forms. The first is shown in Figure 4.5, here the device is close to square. The device specifics are given in Table 4.9. The second approach used a more rectangular shape and is shown

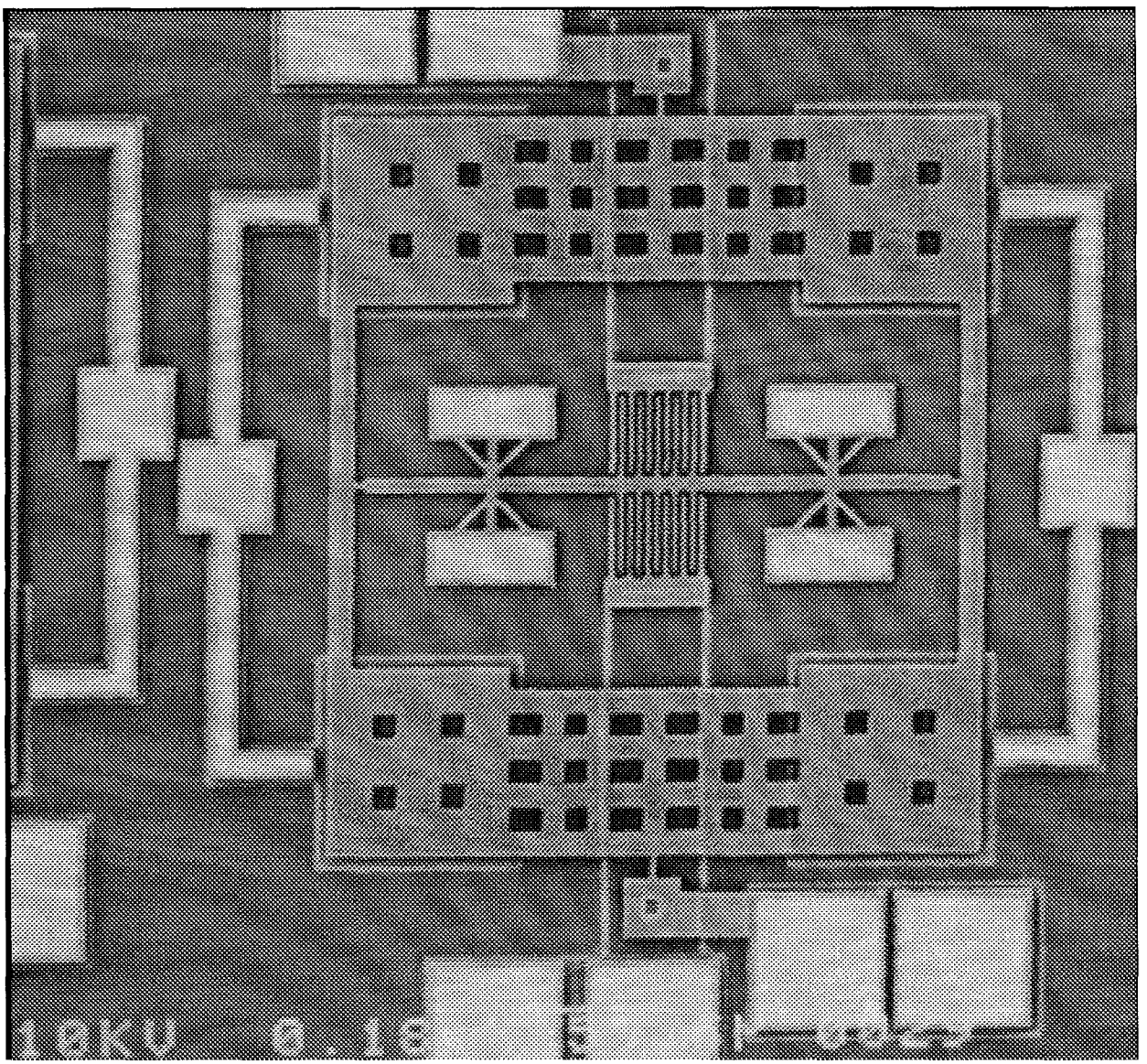

Figure 4.5 Planar gyroscope design 1 in MUMPS 7.

Table 4.9 Variations and Geometry of the First Planar Gyroscope Design.

Parameter	Value(s)
Structural Material	Poly 2
Structure Dimensions	320 μm x 290 μm
Drive Plate Width	80 μm
Drive Plate Length	80 μm
Outer Gimbal Width	2 μm, 4 μm, 6 μm, 8 μm
Outer Gimbal Length	10 μm
Inner Gimbal Dimensions	2 μm x 5 μm and 6 μmx130μm
Number of Sense Combs	10
Comb Overlap	35 μm
Comb Spacing	2 μm
Poly 2 Mass Area	23 μm x 56 μm
Gold Mass Area	17 μm x 50 μm
Mass location (D and R for torque equations)	D= 75 μm R= 30 μm

in figure 4.6. The device specifics and variations are given in Table 4.10. The rectangular approach allows for a larger sustained oscillation amplitude but limits the size of the proof masses. The more square the design, the larger the proof masses may be, but the smaller the amplitude of the sustained oscillation. The output torque is directly proportional to both the mass and the amplitude of the sustained oscillation. In both designs, the device has a sustained oscillation about the external gimbal excited through vertical electrostatic actuation. The output sense mechanism of each design is also identical: two differential comb electrodes. There were two elements varied in both the designs. The first was the width of the outer flexure. The width of the flexure is varied to adjust the device resonant frequency. The second used two different proof mass placements in order to attempt to maximize the output torque, the first placed the proof masses on the output axis and the second placed the proof masses off the output axis. Figures 4.7 and 4.8 show the two mass placements. The first mass placement would result in zero output torque about the output axis. As a result, the devices with the mass placed on the output axis will

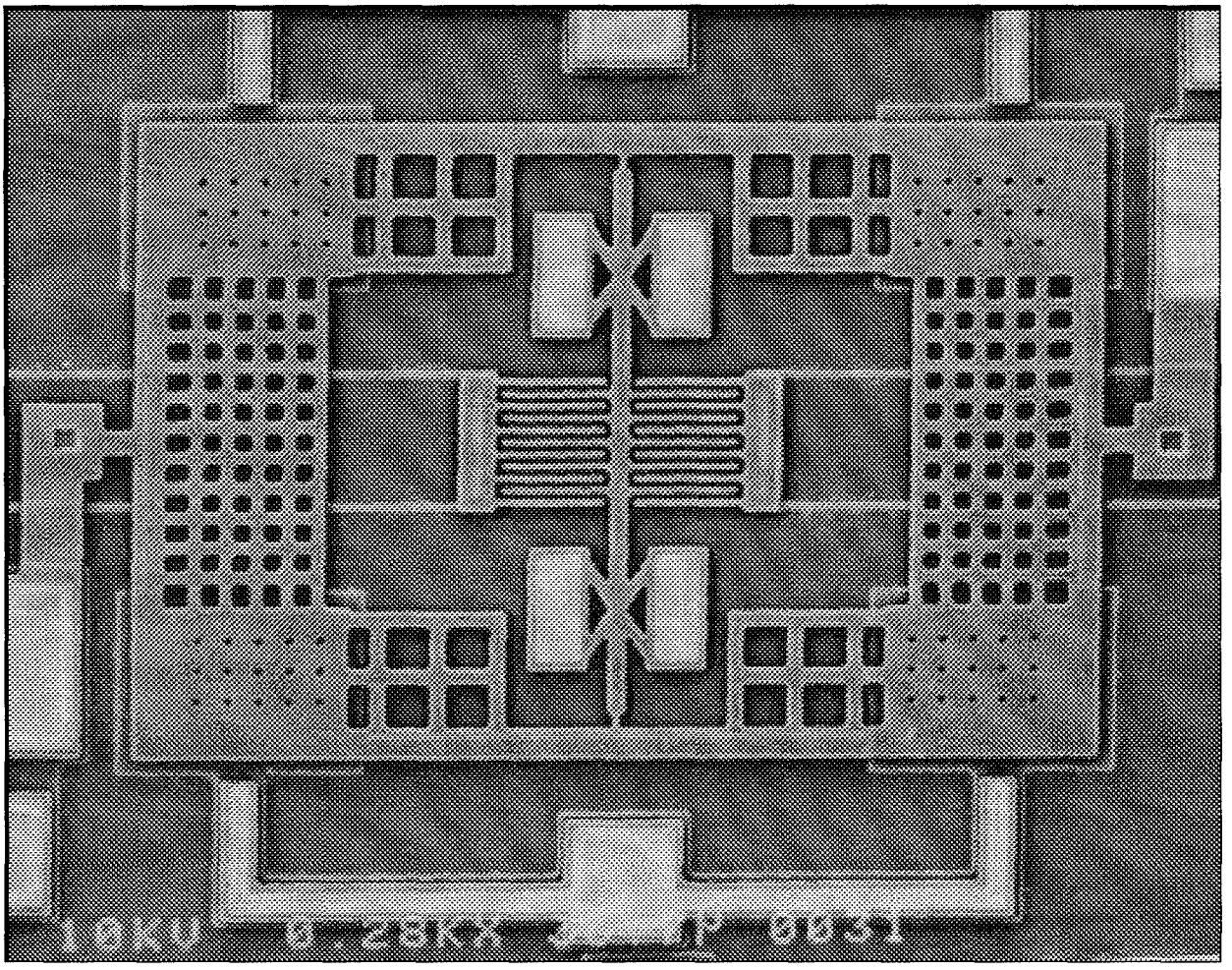

Figure 4.6 Planar gyroscope design 2 in MUMPS 7.

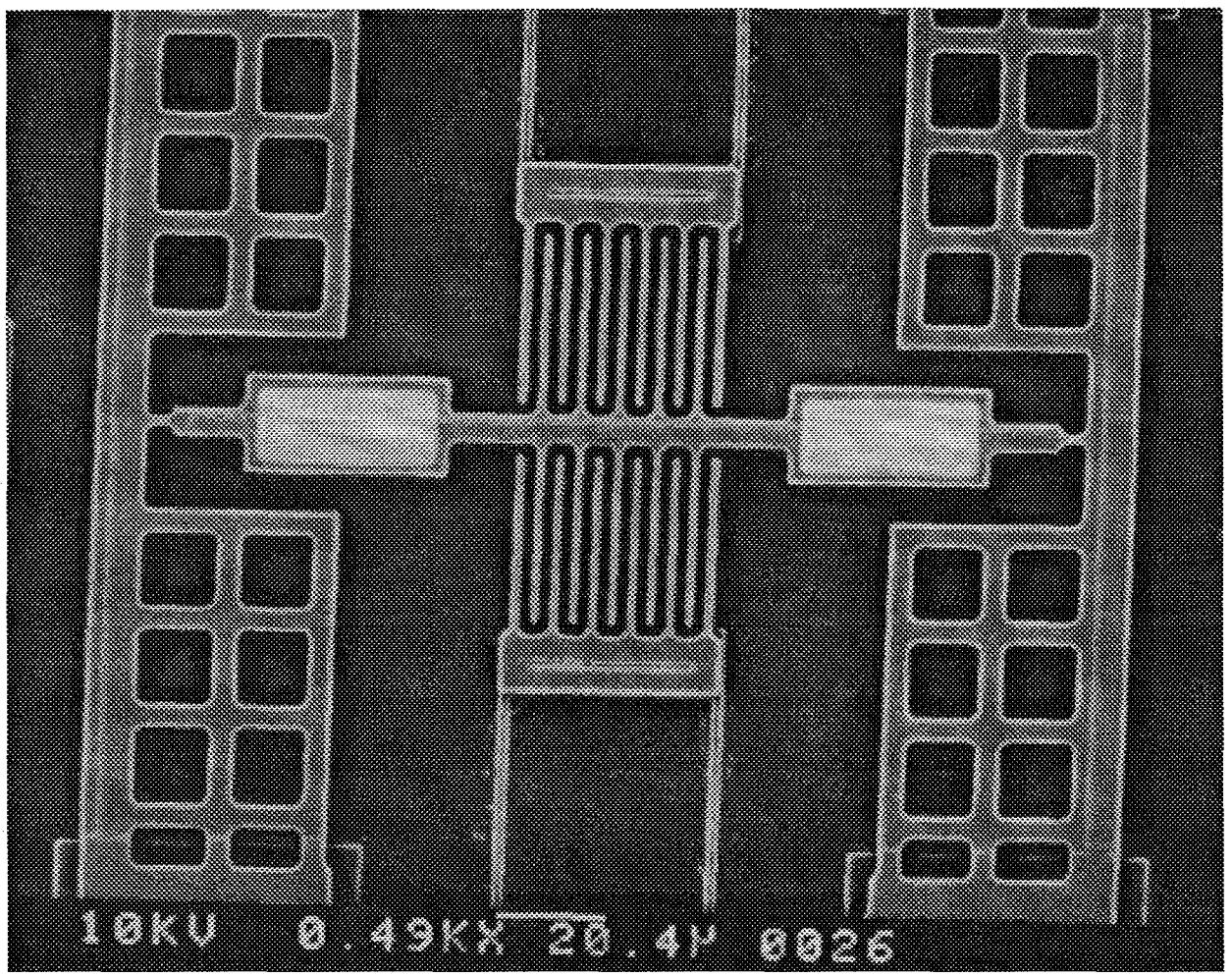

Figure 4.7 Planar gyroscope mass placement on the output axis in MUMPS 7.

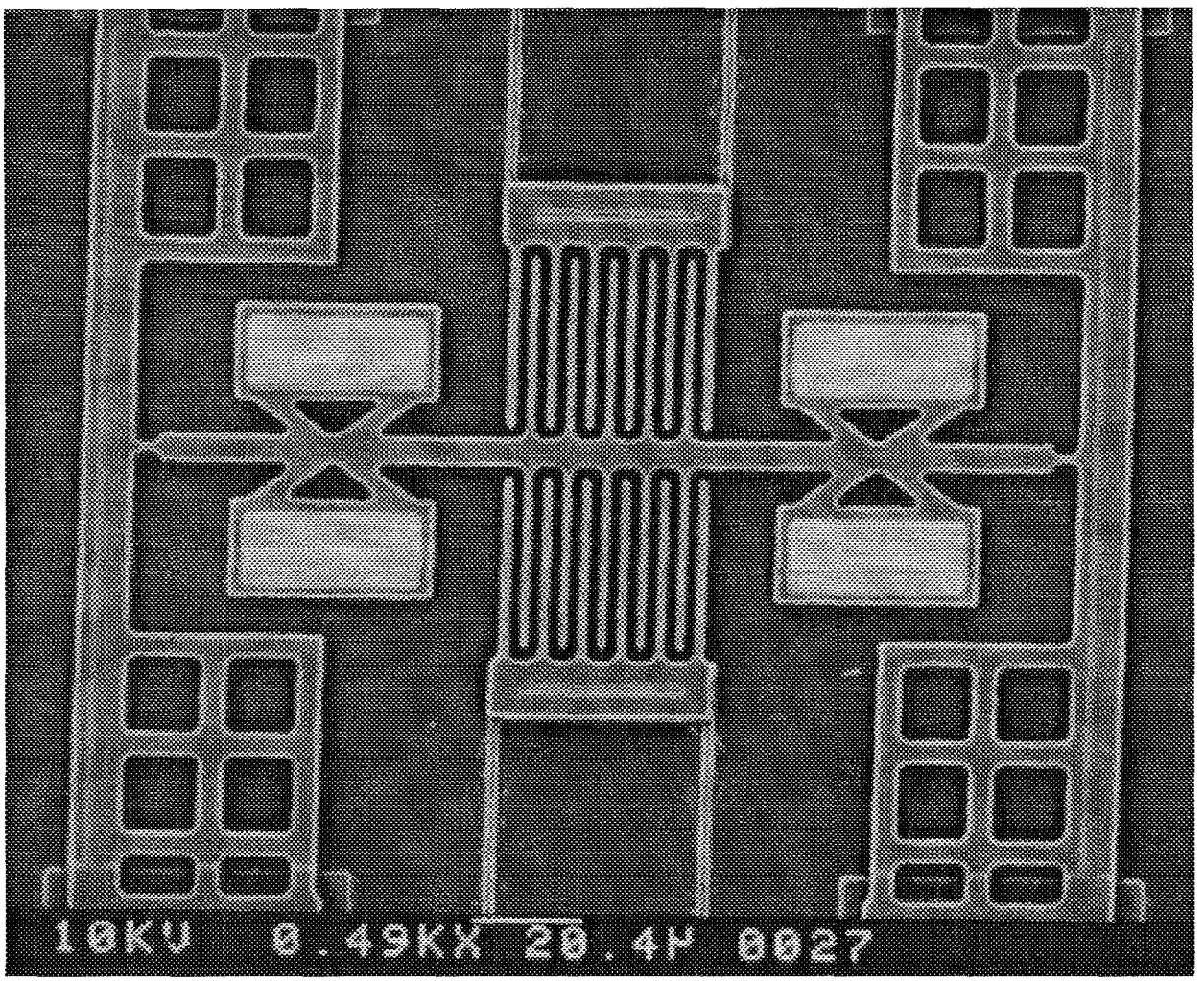

Figure 4.8 Planar gyroscope mass placement off the output axis in MUMPS 7.

Table 4.10 Variations and Geometry of the Second Planar Gyroscope Design.

Parameter	Value(s)
Structural Material	Poly 2
Structure Dimensions	320 μm x 210 μm
Drive Plate Width	50 μm
Drive Plate Length	70 μm
Outer Gimbal Width	2 μm, 4 μm, 6 μm, 8 μm
Outer Gimbal Length	10 μm
Inner Gimbal Dimensions	2 μm x 5 μm and 6 μmx90μm
Number of Sense Combs	10
Comb Overlap	35 μm
Comb Spacing	2 μm
Poly 2 Mass Area	20 μm x 40 μm
Gold Mass Area	14 μm x 35 μm
Mass location (D and R for torque equations)	D= 56 μm R= 20 μm

not function. The second placement used two dumbell-like structures. Examination of the output torque equations suggests that a single dumbell structure located at the center of the output axis would produce a larger output signal. The distance out from the center of the gyroscope generates a negative term in the final output torque equations. If the dumbell structure is located at the center this term is zero, it contributes nothing to the output torque.

4.2.3 Ring Gyroscope. The third type of gyroscope investigated was the ring gyroscope. This gyroscope was first investigated at the University of Michigan [10], where the device was constructed from electro-formed nickel yielding a high aspect ratio. The aspect ratios attainable in the MUMPS process make the Michigan approach to driving and sensing the ring's motion impractical. A comb drive was developed to maximize the interface area when driving the ring. Two methods of sensing the output motion were developed. The first was to use a set of combs identical to the drive combs to sense the

output. The second used a series of plates suspended over poly zero, resulting in a series of capacitive transducers in parallel. Figure 4.9 shows the design implemented using drive and sense combs. The second type of ring gyroscope is shown in Figure 4.10. In these

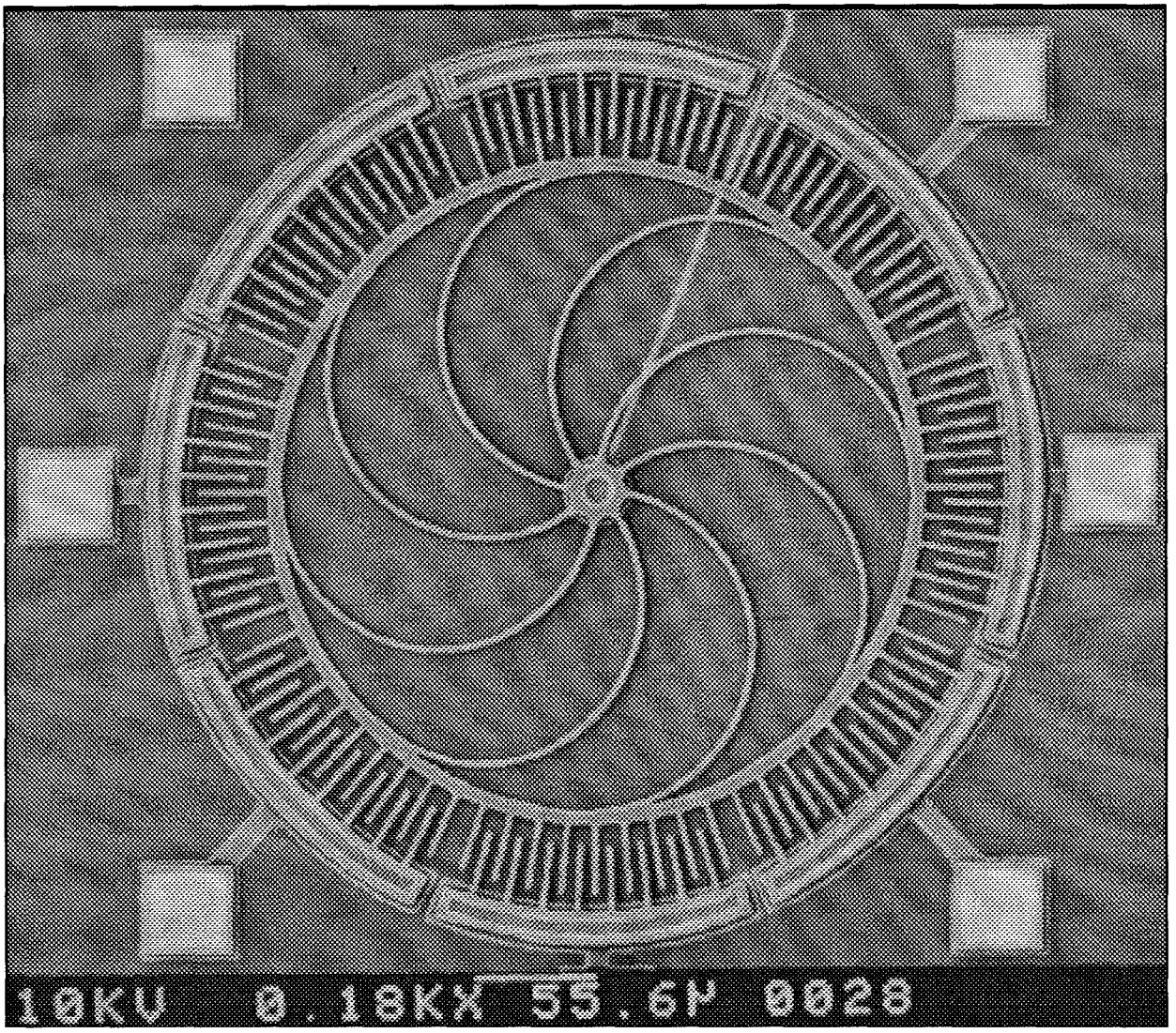

Figure 4.9 Ring gyroscope design using sense combs.

designs, a single drive electrode has an initial capacitance of 0.764 fF and a drive electrode from Putty's gyroscope has a stationary capacitance of 0.737 fF. The drive capacitance of the two structures is almost identical; as a result the force generated by the two drive

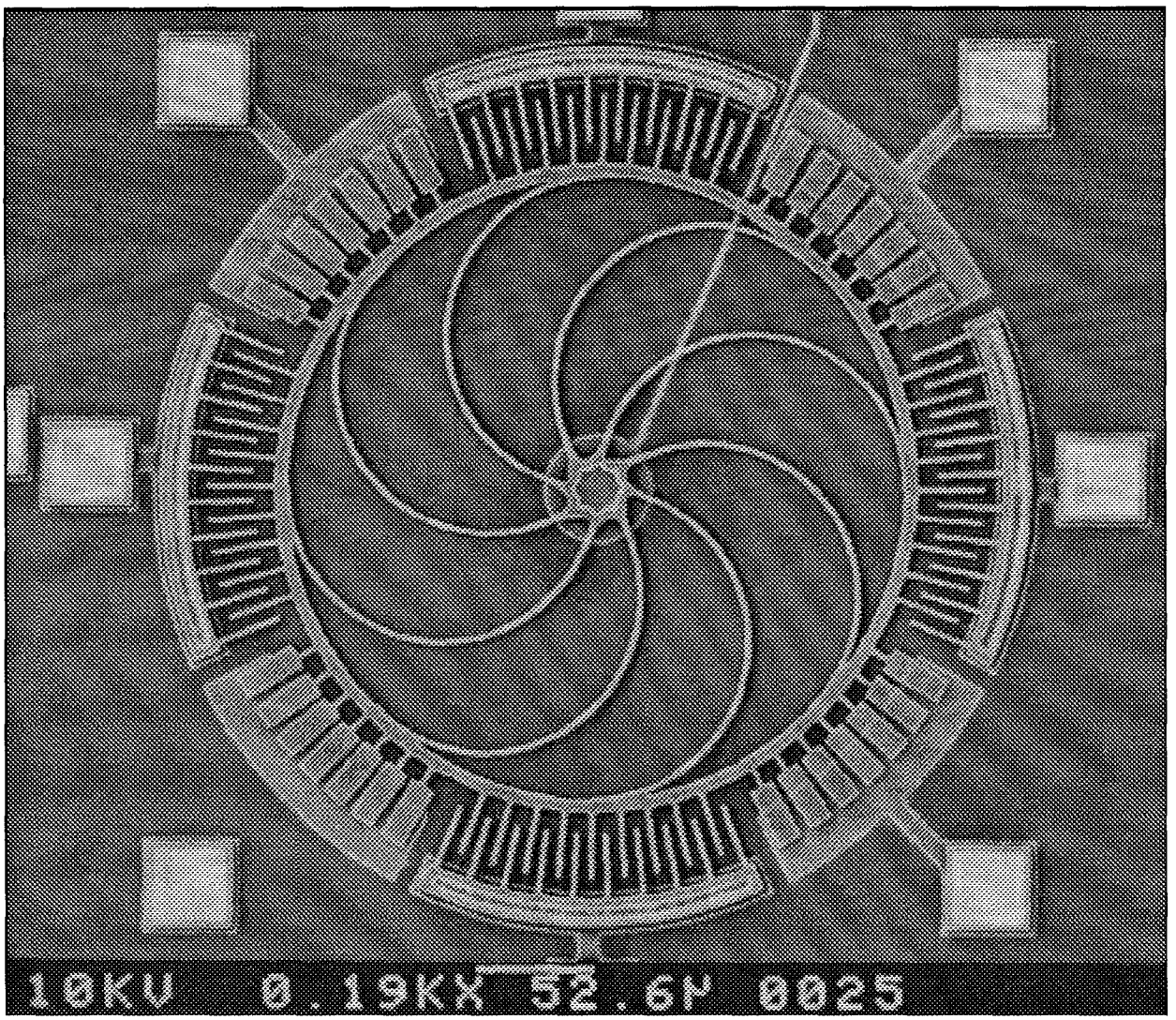

Figure 4.10 Ring gyroscope using capacitive plates to sense output motion.

electrodes is also very close. The sense electrodes for the first ring design are identical to the drive electrodes. This is also the case for the Putty gyroscope. When plates are used instead to sense the output, the stationary capacitance is 0.850 fF, an increase over the stationary sense capacitance. The capacitance values for the sense electrodes provide a means of comparison between the two electrode types. These electrodes, however, are used to sense the change in capacitance. For a larger stationary capacitance in both designs there will be a larger change in capacitance for an output motion.

Each of the ring structures fabricated on the MUMPS 7 fabrication run has an inner radius of 150 μm supported by eight semicircular support springs. In addition eight electrodes surround the structure. Variations of this design are changes in the sense mechanism and support structure. Two sense mechanisms were developed. The first is the use of combs identical to the drive combs and the second is the use of plates suspended over poly zero in order to form a variable capacitor. The nominal comb length is $32\mu m$ with a $5\mu m$ spacing this spacing resulted from the choice of ring diameter. There are seven plates, each having an initial overlap area of $240\mu m$. Three different base designs were investigated. The first and second are cylinders, the first with a diameter of $10\mu m$ and the second with a diameter of $20\mu m$. The third base design is a star shape; two squares with a side length of $20\mu m$ are anchored to poly zero, where one square is rotated 45 degrees relative to the other. The goal of the star base is to make the support more rigid, shifting non-critical resonant frequencies higher than the resonant frequency of the two flexural modes. The cylindrical approach was first used in Putty's working designs. Figures 4.11 and 4.12 show the two approaches to base design. The ring structures fabricated on this run contained no layout errors. The probe electrode structure used to make connections to

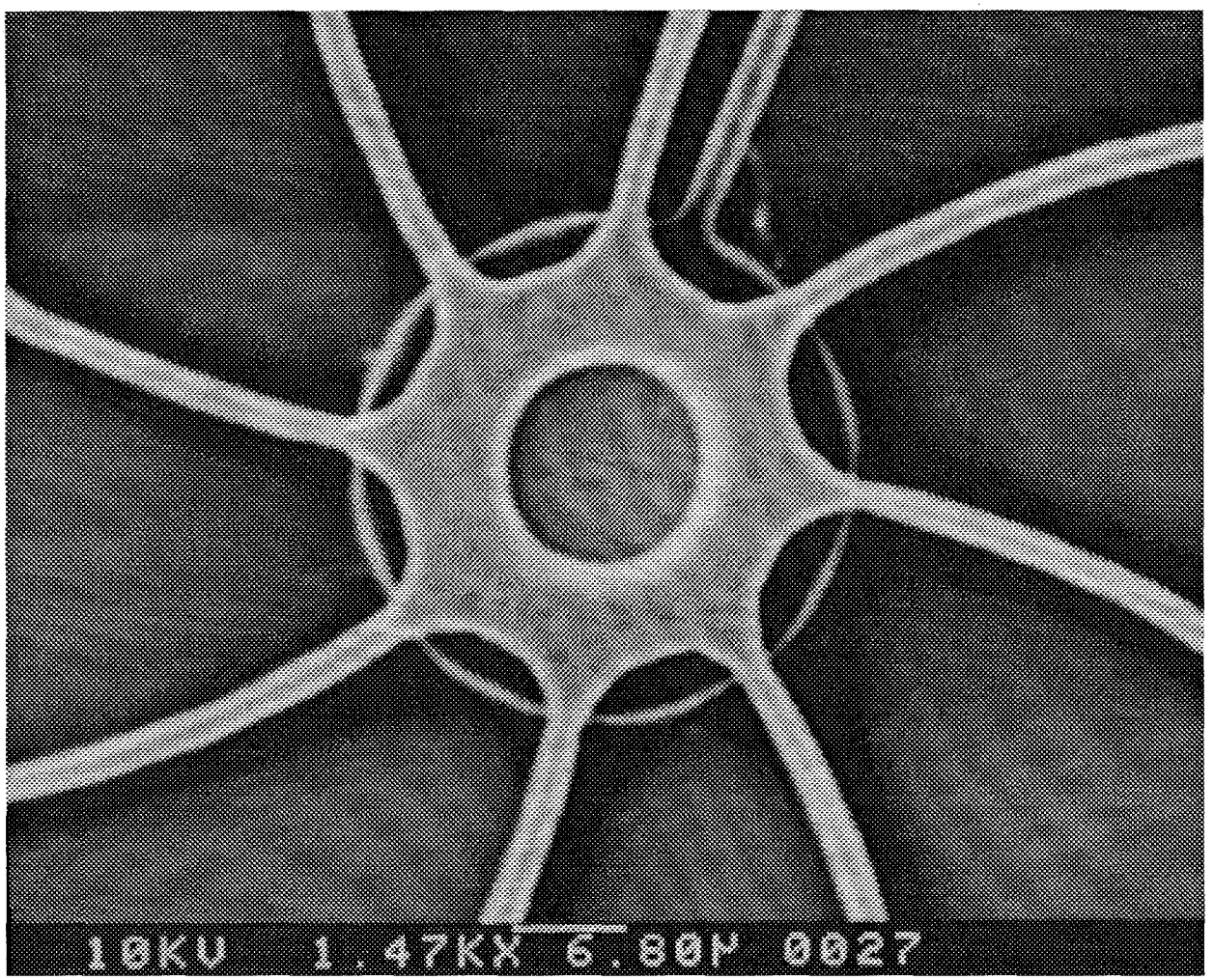

Figure 4.11 Ring gyroscope cylindrical base design.

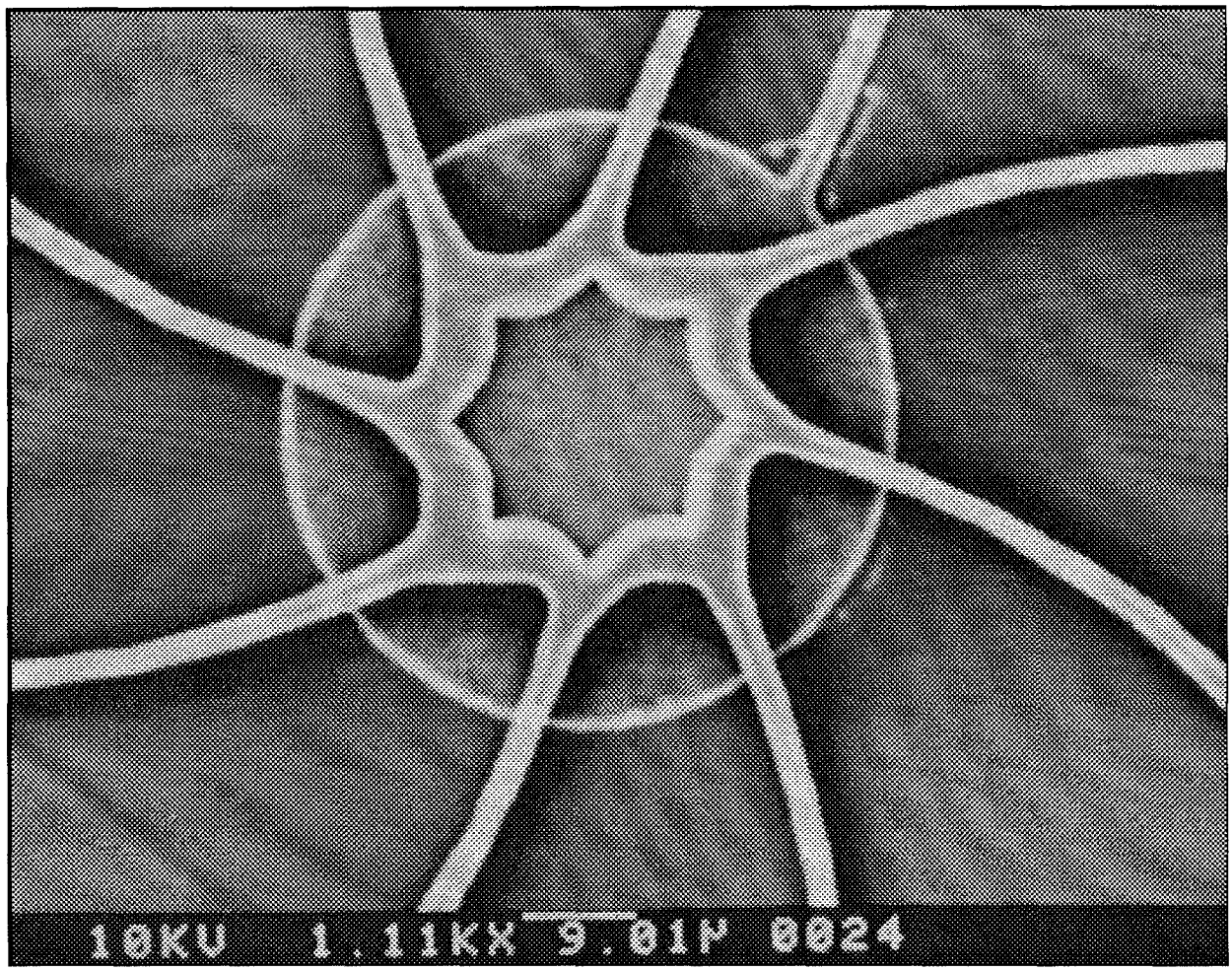

Figure 4.12 Ring gyroscope star base design.

the ring gyroscopes did, however, have one layout error. An electrode was not connected to one of the probe pads. This was corrected in the MUMPS 8 fabrication run.

4.3 MUMPS 8

The statistics from this run are given in Table 4.11. The largest change that takes

Table 4.11 MUMPS 8 Fabrication Statistics.

Film	Thickness (A)	Stress (MPa)	Resistivity (ohm-cm)
poly 0	4696	8.0 (C)	1.5E-3
poly 1	19780	14.1 (C)	1.6E-3
poly 2	15450	10.3 (C)	2.5E-3
metal (Cr/Au)	5200	166 (T)	3.5E-6
nitride	5580	133 (T)	–
oxide 1	20362	–	–
oxide 2	6133	–	–

place on this fabrication run is the creation of stacked structures. A stacked structure increased the thickness of the mechanical layer. This results in higher capacitance values and makes it possible to apply a larger force to a structure. The procedure for creating a stacked structure follows. The layer names are consistent with those used in the process description found in Chapter 2, Section 2.3. To create a stacked structure, first poly layer is grown; this layer is then patterned, leaving a large square of poly 1. The second oxide layer is then grown and the p1p2via glass cut made exposing the poly 1 plate. Poly 2 is grown and patterned, when poly 2 is patterned, it is overetched by 175 percent. An overetch is the duration of the etch past the minimum required to cut the specific layer. Poly 2 is 1.5 microns thick and poly one is 2.0 microns thick. As a result, the overetch of poly 2 is enough to pattern both the poly 1 and poly 2 layers. Figure 4.13 shows each of the steps in creating a double structure. At the time the MUMPS 8 fabrication run was sent out, the

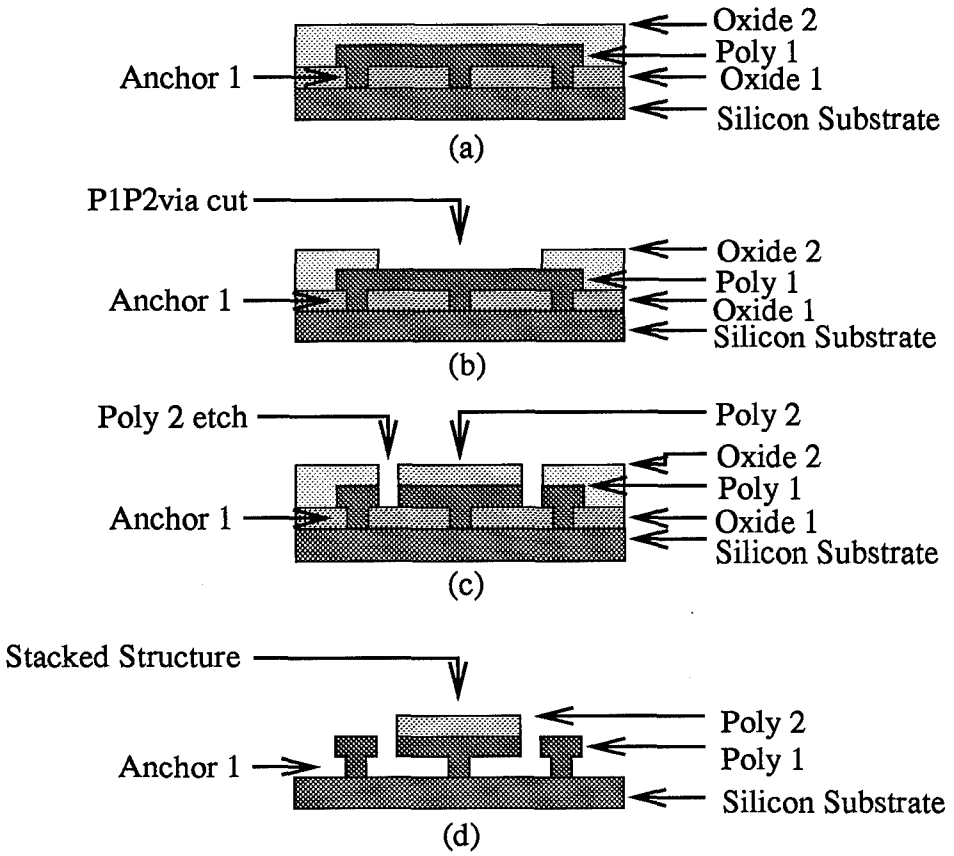

Figure 4.13 Creation of double structures using the MUMPS process: (a) Structure after the second oxide growth. (b) Structure after the p1p2via glass cut. (c) Structure after the poly 2 etch is completed. (d) Structure after it is released showing the anchored poly 1 around the stacked structure.

amount of the poly 2 overetch was unknown; as a result, the poly 1 plate was expanded beyond the p1p2via cut and anchored to prevent excess poly from floating around the chip. Figure 4.14 shows a side view of a fabricated double structure. Figure 4.14 also shows a

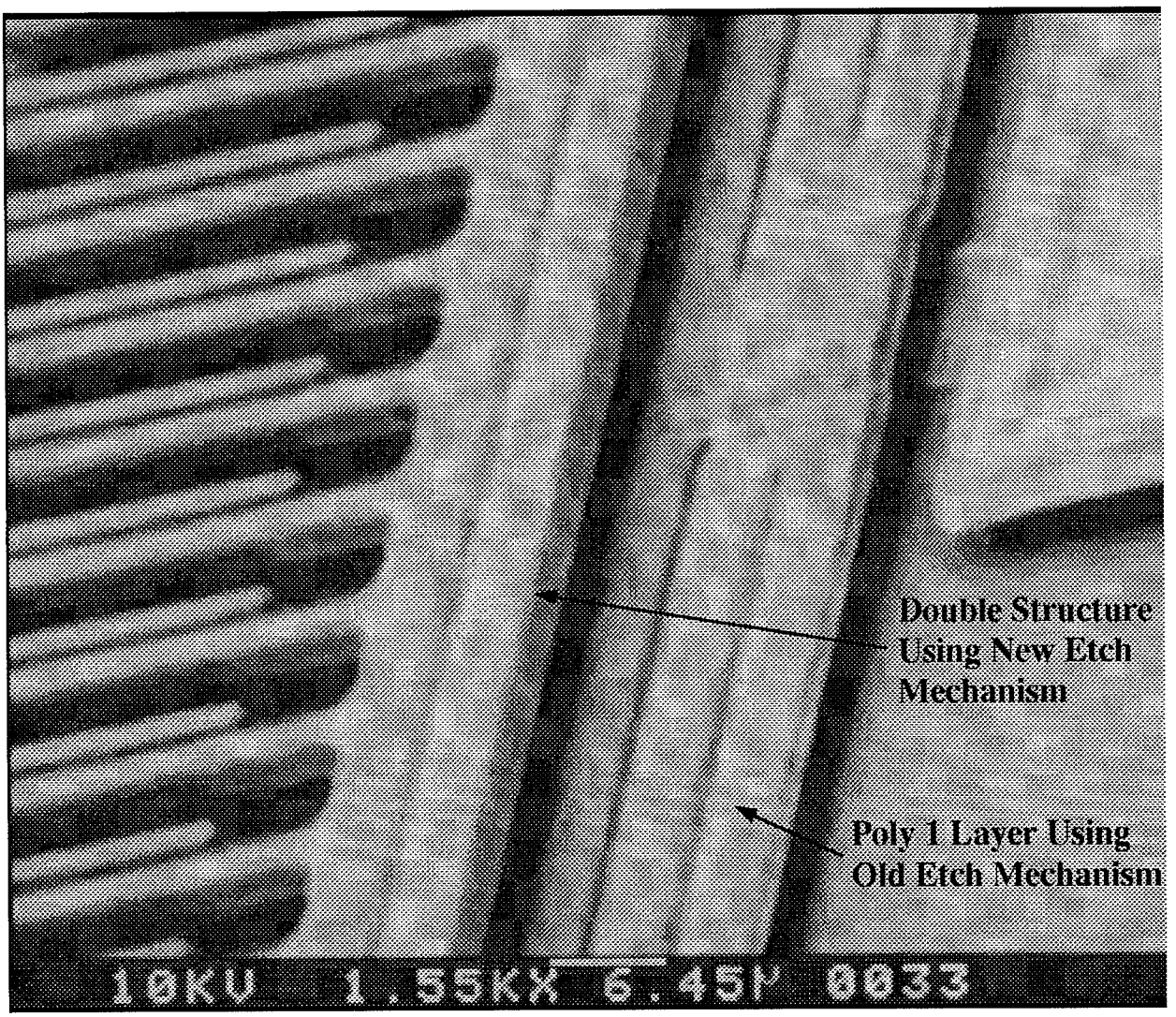

Figure 4.14 Side view of a fabricated double structure.

comparison of two different etch mechanisms used at MCNC. The first etch is the etch that was used up to MUMPS 8, shown by the poly 1 in the right of Figure 4.14 (thinner layer). The sidewall has a rough appearance. The new etch mechanism was used on poly 2 and is

shown by the double structure (thicker layer). This new etch yields a much smoother side wall making the capacitance equations used more accurate.

4.3.1 Vibrating Comb Gyroscope. The two vibrating comb gyroscopes developed for the MUMPS 7 fabrication run were modified for the MUMPS 8 run. The spring lengths were increased to reduce the resonant frequency of the devices in an attempt to increase the ability to drive the devices at their resonant frequencies. The comb overlap was increased to maximize the force applied by the drive comb. The length of the central support spring was increased to maximize output sensitivity. Comb 3 is the modified version of the first vibrating comb gyroscope and Comb 4 is the modified version of the second vibrating gyroscope. Table 4.12 has the design parameters for the Comb 3 design and Table 4.13 contains the predicted resonant frequency information. Table 4.14 has the

Table 4.12 Variations and Geometry Information for the Comb 3 Gyroscope Design.

Parameter	Value(s)
Structural Material	Poly 1, Poly 2 or Stacked
Plate Width	50 μm
Plate Length	100 μm
Support Beam Length	80 μm
Support Beam Width	2 μm
Number of Combs	24
Comb Overlap	30 μm
Comb Length	40 μm
Torsion Bar Width	4 μm, 3 μm, 2 μm
Torsion Bar Length	40 μm

design parameters for the Comb 4 design and Table 4.15 contains the predicted resonant frequency information.

Table 4.13 Comb 3 gyroscope parameters.

Parameter	Value by structural layer		
	Poly 1	Poly 2	Stacked
ksys	2.809	1.607	5.003
M	2.305×10^{-11}	1.800×10^{-11}	4.105×10^{-11}
Msup	7.374×10^{-13}	5.760×10^{-13}	1.313×10^{-12}
Fr	55.23×10^{3}	47.27×10^{3}	55.23×10^{3}

Table 4.14 Variations and Geometry of the Comb 4 Gyroscope Design.

Parameter	Value(s)
Structural Material	Poly 1, Poly 2, or Stacked
Plate Width	50 μm
Plate Length	100 μm
Support Beam Length	80 μm
Support Beam Width	2 μm
Number of Combs	12
Comb Overlap	30 μm
Comb Length	40 μm
Torsion Bar Width	4 μm, 3 μm, 2 μm
Torsion Bar Length	40 μm

Table 4.15 Comb 4 gyroscope parameters.

Parameter	Value by structural layer		
	Poly 1	Poly 2	Stacked
ksys	2.809	1.607	5.003
M	2.305×10^{-11}	1.800×10^{-11}	4.105×10^{-11}
Msup	7.374×10^{-13}	5.760×10^{-13}	1.313×10^{-12}
Fr	55.24×10^{3}	47.27×10^{3}	55.24×10^{3}

4.3.2 Planar Gyroscope and Ring Gyroscope. The planar gyroscope was not changed on this fabrication run. The ring gyroscope design was not modified. A third ring gyroscope was created in order to take advantage of the double structure concept. By doing so the drive electrode capacitance increases to 1.16 fF. This increases the ability to drive the structure.

4.4 MUMPS 9

The MUMPS 9 fabrication run is the last fabrication run used in this thesis. The statistical data on the run is given in Table 4.16. There were changes to all three of the

Table 4.16 MUMPS 9 Fabrication Statistics.

Film	Thickness (A)	Stress (MPa)	Resistivity (ohm-cm)
poly 0	6243	8.0 (C)	1.5E-3
poly 1	19948	3 (C)	2.2E-3
poly 2	15048	6 (C)	3.0E-3
metal (Cr/Au)	4923	5 (T)	3.0E-6
nitride	6243	67 (T)	–
oxide 1	20008	–	–
oxide 2	7598	–	–

gyroscopes on this run to improve on the previous designs. These changes are outlined below.

4.4.1 Vibrating Comb Gyroscope. Testing of the MUMPS 7 and MUMPS 8 die illustrated a need to lower the spring constant for the vibrating comb gyroscope. As a result the support springs were lengthened in both the comb 3 and comb 4 designs. The new designs are named comb 5 and comb 6 respectively. Tables 4.17 and Table 4.18 list the modifications to comb 3 and comb 4 respectively.

Table 4.17 Variations and Geometry Information for the Comb 5 Gyroscope Design.

Parameter	Value(s)
Structural Material	Poly 2 or Stacked
Plate Width	50 μm
Plate Length	100 μm
Support Beam Length	200 μm
Support Beam Width	2 μm
Number of Combs	24
Comb Overlap	30 μm
Comb Length	40 μm
Torsion Bar Width	4 μm, 3 μm, 2 μm
Torsion Bar Length	40 μm

Table 4.18 Variations and Geometry of the Comb 6 Gyroscope Design.

Parameter	Value(s)
Structural Material	Poly 2, or Stacked
Plate Width	50 μm
Plate Length	100 μm
Support Beam Length	200 μm
Support Beam Width	2 μm
Number of Combs	12
Comb Overlap	30 μm
Comb Length	40 μm
Torsion Bar Width	4 μm, 3 μm, 2 μm
Torsion Bar Length	40 μm

The largest concern with these designs is that the poly may sag and stick to the substrate.

4.4.2 Planar Gyroscope. The planar gyroscope design was changed to contain a single dumbell like structure located at the center of the inner axis. This increases the output torque generated by a given input rotation. The device specifics are given in Table 4.19. Figure 4.15 shows a SEM photograph of the new planar gyroscope design. This device

Table 4.19 Variations and Geometry of the First Planar Gyroscope Design.

Parameter	Value(s)
Structural Material	Poly 2
Structure Dimensions	220 μm x 320 μm
Drive Plate Width	30 μm
Drive Plate Length	85 μm
Outer Gimbal Width	2 μm
Outer Gimbal Length	10 μm
Inner Gimbal Dimensions	2 μm x 5 μm and 4 μmx290μm
Poly 2 Mass Area	50 μm x 220 μm
Mass location (distance from center axis)	R= 50 μm

will maximize the output torque generated for a given input, while maintaining symmetry. In addition the interface capacitance of this type of planar gyroscope is much larger than for the previous designs. The larger interface capacitance should increase device sensitivity.

4.4.3 Ring Gyroscope. There were two main modifications to the ring gyroscope on this fabrication run. First, the diameter of the ring was doubled. This change was dictated when initial tests failed to identify the device resonant frequency. The increase seems dramatic; in the initial designs, a diameter of 400 μm was used in order to prevent sagging of the suspended structure. The designs developed at Michigan, however, used a much larger diameter of 1 mm for their designs. The large diameter was made possible

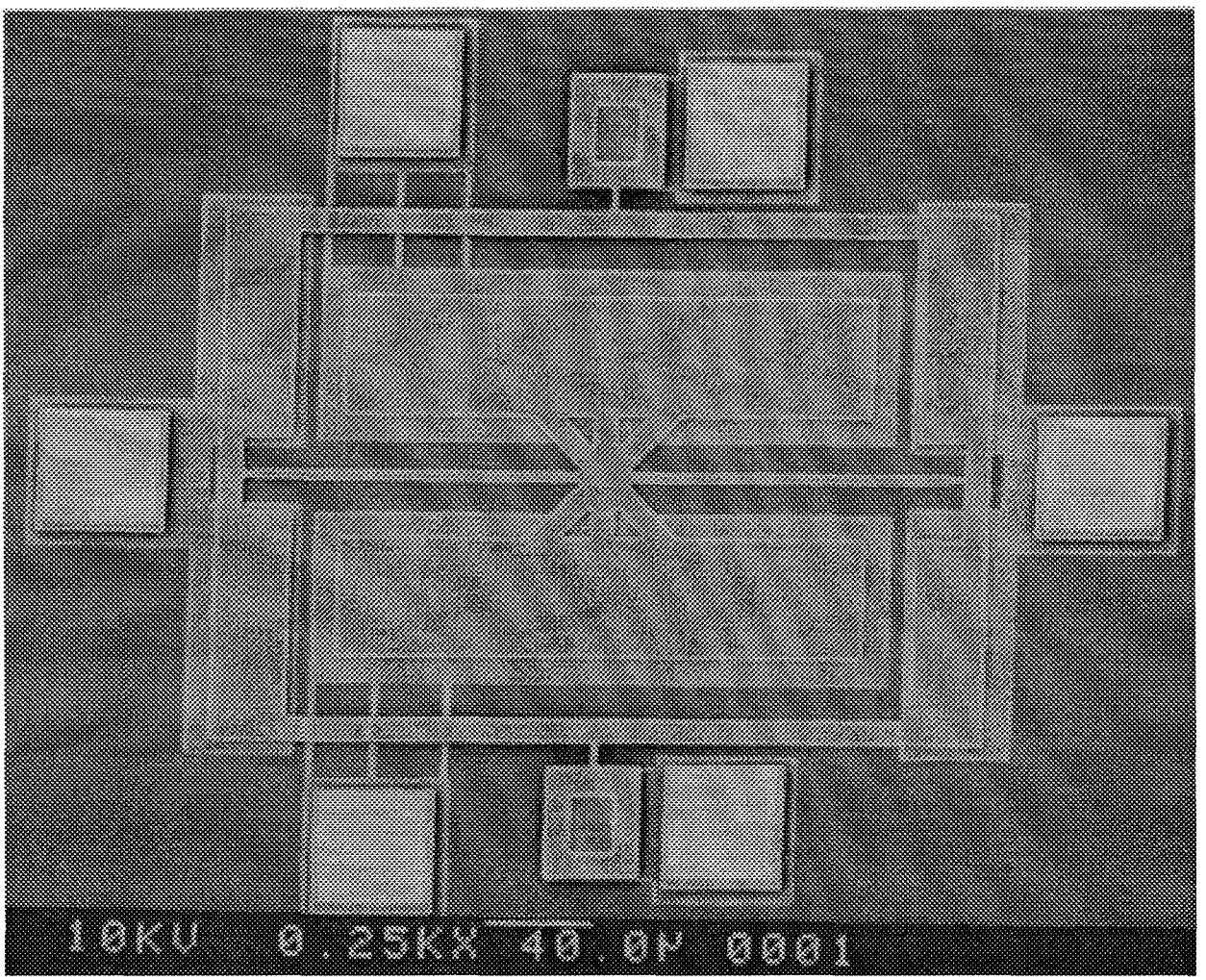

Figure 4.15 Planar gyroscope 4 design.

largely because of the high vertical sidewalls. The new ring diameter of 800 μm in poly may result in the structure sagging down onto the substrate. The second change is a result of an ambiguity created in the first designs. In the ring gyroscopes on the MUMPS 7 and MUMPS 8 designs, a structure with eight electrodes was using and each electrode accounted for 22.5 degrees of the ring. In normal device operation, a resonant node, or maximum of the resonant pattern, is established in the middle of the sense electrode. For an input rotation, that node moves counter-clockwise for a positive rotation and clockwise for a negative rotation. In both the devices in which sense combs are used and those in which sense plates are used, the direction of rotation will be unknown until the node moves 11.25 degrees in either direction. This severely limits the device sensitivity. In order to reduce the effects of this ambiguity, the sense electrodes have been made smaller. A single sense electrode in this design accounts for 5 degrees of the ring and the resulting ambiguity is reduced to 2.5 degrees. The cost of reducing the ambiguity is the reduction in the nominal capacitance of the sense electrodes. The ring shown in Figure 4.16 is the result of adjusting for these concerns. Electrodes not used for sensing or driving the ring will be grounded with respect to the ring. The geometry specifics of the ring gyroscope are given in Table 4.20.

Table 4.20 Variations and Geometry of the Fourth Comb Drive Gyroscope Design.

Parameter	Value(s)
Structural Material	Poly 2, or Stacked
Diameter	800 μm
Number of Support Springs	8
Anchor Type	Star Base
Nominal Comb Overlap	47 μm
Nominal Comb Length	56 μm

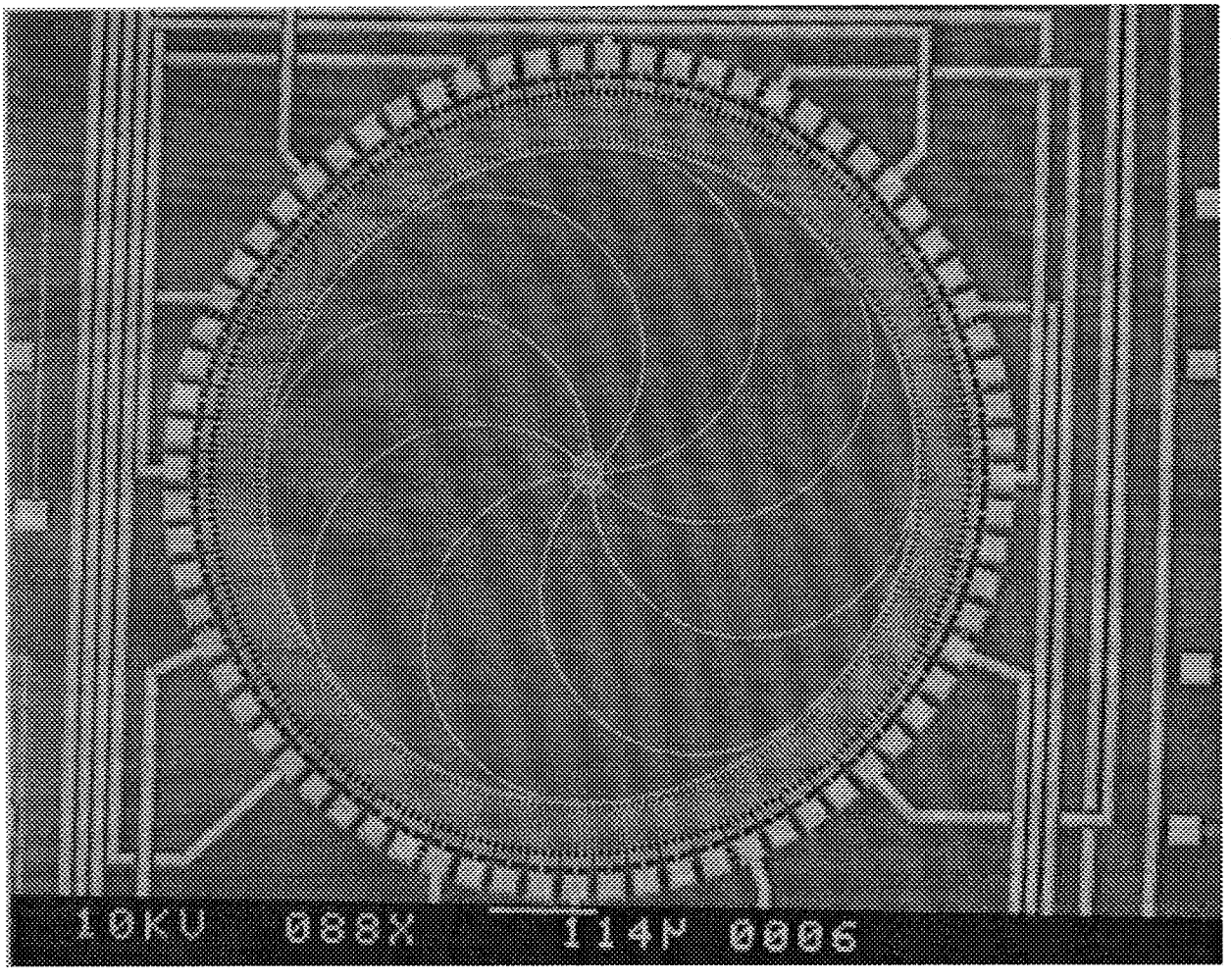

Figure 4.16 Modified ring gyroscope design.

In the previous four sections, design considerations for the three types of gyroscopes were discussed. Specific geometry data was given and, where applicable, predicted resonant frequencies were generated. The next section covers the experimental approach and procedures used in testing the devices, including the procedures used to process the die once returned by MCNC.

4.5 Experimental Approach / Procedures

In this section, the experimental approach and procedures are covered. First a general plan of attack is developed. This plan is followed by the experimental procedures as implemented. The larger task of testing the vibrating gyroscopes may be broken down into a series of smaller tests. The general approach to testing each of the vibrating gyroscope designs is given below:

1. Attempt to drive the devices to resonance; measure the corresponding resonant frequency and record the results.
2. Force a motion identical to the output motion physically to see if it may be sensed.
3. Wire bond devices out and verify 1 and 2.
4. Place devices into a rotating field to apply an input rotation and measure output.

In the following sections specific procedures used will be provided. An equipment list precedes each set of procedures.

4.5.1 Release Procedures. When the chips are delivered to AFIT, they are not yet released. The release process involves three steps; the first removes any photo-resist

on the die, the second performs the silicon dioxide etch, the third attempts to dry the die without causing the devices to stick. These procedures must be used on every die before it may be tested.

Equipment

1. 1 Small pail
2. 4 150 ml Beakers
3. 1 Petri dish
4. 1 Hot plate
5. 1 Magnetic stirrer with stir bar
6. 1 Tweezers
7. Rubber gloves
8. Apron and Lab Coat
9. Protective Eye-ware

Chemicals

1. Hydrofluoric Acid (HF) 49%
2. 2-Propanol
3. Methanol
4. Acetone
5. De-ionized (DI) Water

Procedures

1. Clean all glassware with DI water and blow dry with nitrogen.
2. Fill pail about half full of DI water. Place stir bar in pail off to one side so die may be placed in pail out of the stir bar's path. Adjust stirrer speed so water is continuously moving.
3. Place petri dish on hot plate. Adjust heat so the dish is warm to the touch.
4. Label each of the four beakers with one chemical name (HF, Acetone, 2-Propanol, and Methanol) and pour approx. 50ml of the appropriate chemical into the labeled beakers.
5. Place the die to be released into the acetone, stirring occasionally for 5 minutes. The acetone is intended to wash any excess resist away.
6. Remove die from the acetone and place into the methanol, stirring occasionally for 3 minutes. The methanol should rinse excess acetone and resist off the die.
7. Place die into DI water bath for 3 minutes to remove the methanol.
8. Place die into HF for 120 seconds. The HF etches the silicon dioxide, releasing the structure.
9. Remove the die from the HF, keeping a drop of liquid on top of the die, to prevent stiction, and place in the DI water bath for 5 minutes.
10. Remove the die from the DI water bath, again keeping a drop on top of the die and place into the 2-Propanol. Leave in 2-Propanol for 5 minutes.

11. Remove die from 2-Propanol and place in the petri dish. If the plate is too hot the Propanol will boil, flipping the chip. This should be avoided. If unsure of the temperature, place a drop of Propanol into the dish and watch to see if it boils. If it does, turn the heat down and repeat. The goal is to evaporate the Propanol rapidly but not to boil it off.

12. Inspect the die under a microscope to verify the release. If the die is not completely released return the die to the HF bath and repeat steps 9-11.

13. If the die has been released, dispose of chemical in properly marked waste bottles. The DI water may be dumped in the sink. Rinse and dry equipment used.

Steps 5-7 of the procedures are used to remove any excess resist on the die. Steps 8 and 9 perform the actual release, and steps 10 and 11 attempt to dry the die without the devices sticking to the substrate. When a device sticks to the substrate, it is referred to as stiction. Stiction often results because, as the device dries, the meniscus pulls the device to the substrate. The force generated is a function of the surface tension of the liquid. Water has a high surface tension in comparison to 2-Propanol; as a result, if the water is sublimated with 2-Propanol, there is a better chance stiction will be avoided. If the devices do stick to the substrate, it is not possible to free them. Once the chips are released, they may be tested.

4.5.2 Resonant Frequency Testing. The resonant frequency testing proved to be difficult. Experimental test procedures were verified using a comb drive lateral resonator included on every die as a test structure by MCNC (see Figure 4.17). The resonant frequency of this test structure was provided by MCNC for the MUMPS 6 fabrication run.

Three methods of testing for resonance were investigated. The first method was optical.

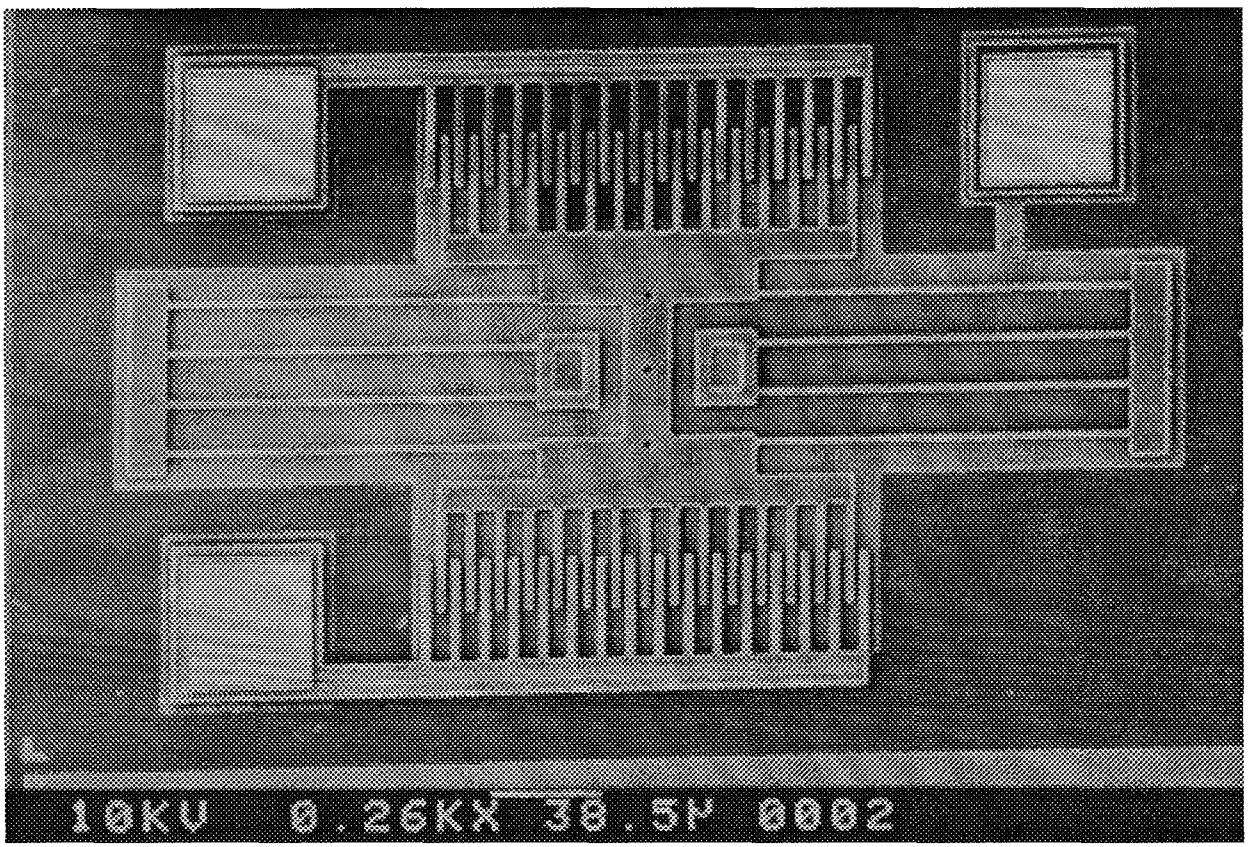

Figure 4.17 MCNC lateral comb resonator test cell.

The bandwith of resonance is very small, so if the output motion is visible, resonance may be identified by slowly varying the frequency of the input waveform until resonance is observed. The second method used a network analyzer to measure resonance. The third and final method involved monitoring the current output by the voltage source; at resonance, the current should increase as more energy is coupled from the electrical to the mechanical system. Specific procedures for testing the devices are included in this section. An equipment list precedes each of the procedure sections.

Each of the gyroscopes has a stationary electrode and a free, or moving electrode. For the vibrating comb and ring gyroscopes, these are a set of combs. On the planar gyroscopes, the stationary electrode is a poly 0 pad and the moving electrode is the poly 2 plate.

4.5.2.1 Optical Identification. Previous work on lateral comb resonators indicated that the resonant frequency of structures may be determined by visual identification [27]. The first tests were conducted based on this approach. The procedures used to identify the resonant frequency visually are given below.

Equipment

1. High voltage DC power supply
2. HP function generator
3. Micromanipulator Probe Station with 2 probes

Procedures

1. Connect the stationary electrode to the output of the function generator using a BNC to BNC cable. Disable the function generator output to protect devices from damage, adjust the amplitude to 20 V peak to peak, and set the initial frequency to 10 kHz (well below the frequency of interest).
2. Connect the second probe from the DC power supply to the structure. Place a DC bias on the structure to facilitate resonance. The DC bias acts as a static load, increasing the magnitude of the resonance spike. An initial value of 60 V was attempted. This value was increased to 150 Vdc for testing of the fabricated devices.

3. Enable the output of the function generator and slowly begin raising the frequency of the output waveform. At resonance, the device motion will be visible.

4. Once motion is visible, it is possible to make small adjustments to the function generator's output frequency so the maximum displacement is observed.

The above method is a not as accurate as other methods. Because the bandwith of resonance is small, it does provide a good first measure of at the device resonant frequency.

4.5.2.2 Network Analyzer Measurements. The network analyzer provides a reliable method of measuring the resonant frequency. Several experimental set-ups were used to conduct resonant frequency measurements on the vibrating comb and vibrating ring gyroscopes using the network analyzer. Each method is listed below, along with variations attempted.

Equipment

1. 1 HP 4195A Network / Spectrum Analyzer

2. 2 HP 41800A Active probes

3. Micromanipulator probe station with 3 probes

4. HP-IB compatible printer

5. High voltage DC power supply

Procedures

1. The network measurements require applying a source input to one fixed electrode and measuring the output from a second. For the vibrating comb gyroscope, the input

is connected to the center structure and the output is measured on one of the two other fixed electrodes. For the ring gyroscope, the input is placed on one comb drive and the output is placed on the fixed electrode 180 degrees from the input. Figure 4.18 shows a general diagram of the network analyzer, showing functional blocks and labeling the input and output connections.

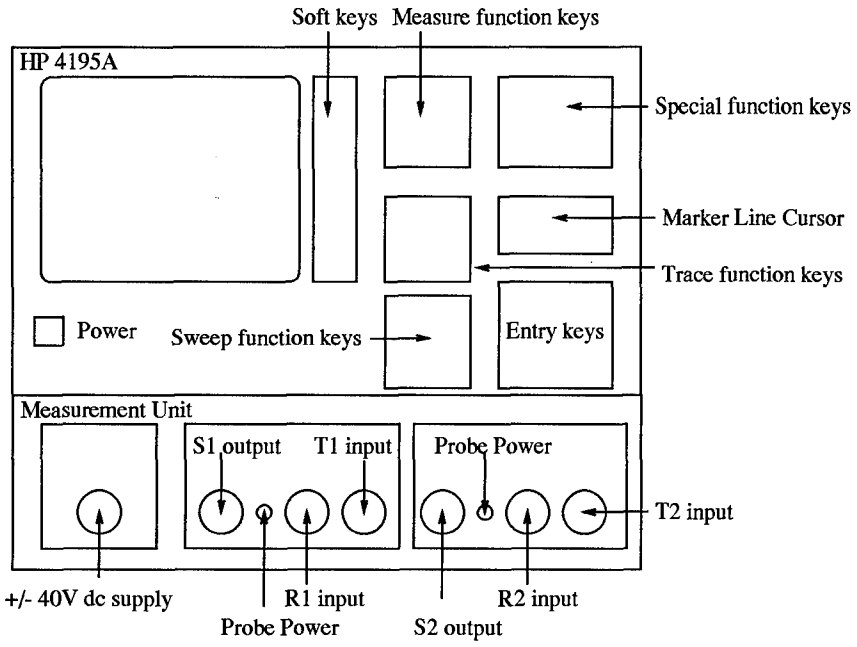

Figure 4.18 Network analyzer block diagram labeling output and input connections.

2. All measurements were conducted using active probes in order to minimize system noise. The probes are connected to the R1 and T1 Network Analyzer inputs. The power of one active probe is connected to the probe power connection next to the S1 output (source 1 output) and the second active probe's power is connected to the probe power port to the right of the S2 output. The S1 output is connected to the R1 input (reference 1 input) using a BNC to BNC cable and a dual male single

female BNC adapter. The female connection of the adapter is connected to the probe attached to the input fixed electrode.

3. The T1 input (test channel input) is connected to the probe attached to the output fixed electrode.

4. The DC bias from the network analyzer is not sufficient for these tests. The high voltage power supply is used, and is attached to the free electrode (suspended structure) and an initial voltage of 60V is applied.

5. The procedures for calibrating the network analyzer for a through transmission measurement are found on pages 4-19 and 4-20 of the network analyzer user manual [35]. In order to ensure the accuracy of the calibration, both the input and output probes were placed on the same pad to short the input to the output.

6. The amplitude of the output oscillation on S1 was adjusted to its maximum value of 1.26 V.

7. Different frequency ranges were investigated to increase the resolution. The network analyzer breaks the frequency range into a maximum of 401 pieces, making the minimum step size equal to the frequency span divided by 401. A range of 2 kHz was used to ensure a high resolution. The 2 kHz span was adjusted to cover frequencies from 15 kHz to 75 kHz for the comb and ring gyroscopes.

8. No output was seen for the vibrating comb or ring gyroscopes. As a result, the DC bias was increased to 150 V and the output was amplified to +/- 10 V peak-to-peak sinusoid. The network analyzer was recalibrated with the amplifier in line, and the frequency range from 15 kHz to 75 kHz was again investigated.

9. The second modification was to raise the substrate potential to the DC bias level in an attempt to reduce the lateral friction on the structures. This was attempted both with and without the amplifier in line. The amplifier eventually was removed because its response characteristics dominated the measurements.

10. In an attempt to increase the quality factor of the resonance, a low temperature probe station was used to evacuate the chamber to 15mTorr. The measurements were conducted with both the amplifier in and out of line with the source. The measurements were conducted in a vacuum in an attempt to increase the magnitude of the resonant spike.

The verification and results of these experimental procedures are provided in the following chapter.

4.5.2.3 Current Monitoring. The final method investigated was monitoring the current sourced by a function generator as the input frequency was swept. At mechanical resonance, the current sourced should increase as the coupling between the electrical and mechanical systems increases. The maximum current observed should be at resonance.

Equipment

1. Function generator
2. Resistors (1 ohm,10 ohm,100 ohm)
3. Volt meter
4. Micromanipulator probe station 2 probes.

Procedures

1. Connect the function generator output in series with the resistor to one fixed drive electrode.
2. Connect the volt meter across the resistor.
3. Apply a DC bias to the suspended structure. A voltage of 150 Vdc is used.
4. Adjust the output of the function generator to get a 20 V peak to peak sinusoid with an initial frequency of 10 kHz.
5. Slowly sweep the input waveform frequency and monitor the voltage across the resistor.
6. Repeat with different resistor values until valid output is obtained

The procedures are presented in the order that they were attempted. The network measurements taken were chosen because of frequency limitations on the impedance and reflectance / transmission test sets. Reflectance / transmission tests sets, used to determine the two port network parameters (S-parameters), have a minimum frequency threshold of 100kHz. A minimum frequency of 100kHz is approximately two times the frequencies of interest. The impedance test sets available have similar frequency limitations.

4.6 Chapter Summary

This chapter presented the experimental approach and procedures used in completion of this thesis. Device descriptions along with design variations were presented in sections corresponding to the fabrication runs the designs were included on. The procedures used were then presented along with equipment lists to simplify implementation. The following

chapter will provide validation of the procedures and the observed results when applied to test devices.

V. Experimental Validation and Results

The previous chapter outlined the general approach to device testing and then described the specific procedures implemented. This chapter provides the validation of those procedures and the results of implementing the procedures on experimental devices. In addition, a discussion of the observed experimental results are discussed.

5.1 Optical Identification of Device Resonant Frequency

Verification of the optical identification procedures was conducted on die from the MUMPS 6 fabrication run. Predicted resonant frequencies were provided by MCNC and six different MCNC test devices were investigated. The results provided from MCNC were based on a 50 volt DC bias applied to the suspended structure and a 16 volt peak to peak input sinusoid applied to the drive combs. A 50 volt DC bias was also used to validate the experimental procedures outlined in Chapter 4; however, an input waveform of an 18 volt peak to peak sinusoid was used. The amplitude of the input waveform used by MCNC was unknown when the tests were conducted. This resulted in the difference in the amplitude of the waveform used to conduct the tests and the waveform used by MCNC. The results provided by MCNC indicate an output oscillation amplitude of 3 μm to 5 μm, which was experimentally verified. The results of testing for resonant frequency are provided in Table 5.1. These results show that optical identification may be used to roughly determine resonant frequency on devices for which the output motion is visible. There was no output oscillation visible below 25 kHz or above 28 kHz. In addition, there were no significant fabrication errors on this run. A larger variation in resonant frequencies was

Table 5.1 Experimental results from optical resonant frequency identification tests.

Device Name	Observed Resonant Frequency
MCNC	26.3 kHz
Device 1	26.8 kHz
Device 2	26.9 kHz
Device 3	26.8 kHz
Device 4	26.6 kHz
Device 5	26.7 kHz
Device 6	26.6 kHz

seen on the MUMPS 7 and MUMPS 8 fabrication runs, possibly as a result of fabrication inconsistencies. A full discussion of fabrication problems in MUMPS 7 and MUMPS 8 is included at the end of this chapter.

The optical approach to resonant frequency determination presents a simple but crude method of identifying the resonant frequency. Once the procedure was verified it was applied to the vibrating comb and ring devices fabricated on the MUMPS 7, MUMPS 8, and MUMPS 9 runs. Using a 60 volt DC bias and a 36 volt peak to peak sinusoid, the frequency of the input waveform was swept slowly from 15kHz to 150kHz, but no output motion was observed. The DC bias applied to the structure was then increased to 100 volts and then followed by a DC bias of 150 volts. No output motion was observed.

5.2 Network Analyzer Measurement Validation and Resonant Frequency Results

The use of the network analyzer was validated using the MCNC lateral comb resonators on the MUMPS 7 die. The resonant frequency, of the MCNC test structures, was first measured using the optical method, validated in the previous section. The network analyzer was then connected, as outlined in the procedures in Chapter 4, and measurements

were taken. The resonant frequency determined optically was 21.5 kHz with a 50 volt DC bias and a 36 volt peak-to-peak sinusoid. The network analyzer measured frequency was 21.3 kHz also at a 50 volt DC bias. The output of the network analyzer consists of two curves; the *magnitude* of the test channel divided by the *magnitude* of the reference channel (output over input) in mdB, and the phase in degrees. Several different DC bias voltages were tested. The results indicate a correlation between the DC bias voltage and the device resonant frequency. This result is expected, since the DC bias voltage applies a static load to the structure. The larger this load is, the higher the resonant frequency will be. A good analogy to this effect is a guitar string. The resonant frequency of the string is adjusted by changing the tension on the string. The application of a static load has changed the string's resonant frequency. Network analyzer outputs are shown in Figures 5.1-5.7 for DC biases from 0 volts to 150 volts. The plot for the DC bias of 50 volts (Figure 5.3) was used to compare the optical results and the network analyzer results for consistency. In addition to increasing the resonant frequency, Figures 5.1- 5.7 show that, as the static load is increased, the resonant spike becomes more asymmetric. The dependence of resonant frequency on DC bias indicates the need to test experimental devices at a set of different DC biases. The initial DC bias (60 volts) was increased first by 15 volts DC then in 25 volt increments to its maximum value of 150 volts. Both the vibrating comb and ring gyroscope were investigated. Resonance could not be determined for experimental vibrating comb and ring devices using this method. Possible explanations for the inability to identify the resonant frequencies of experimental devices using this method are provided in Chapter 6.

In an attempt to increase the amplitude of the resonant spike, the devices were placed in a vacuum, chamber at 15mTorr. By placing the devices in a vacuum the effects

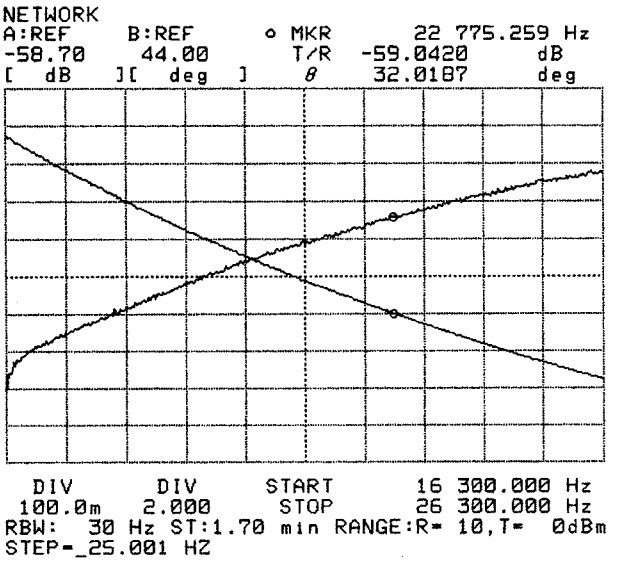

Figure 5.1 Network analyzer output for the MCNC comb test structure with a zero volt DC bias (MUMPS 7).

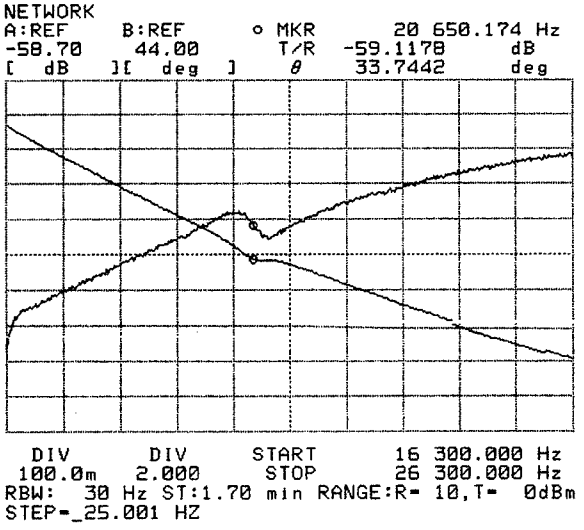

Figure 5.2 Network analyzer output for the MCNC comb test structure with a 25 volt DC bias (MUMPS 7).

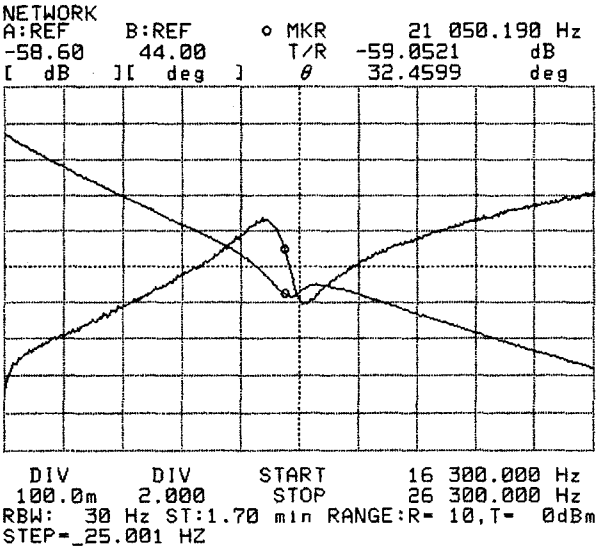

Figure 5.3 Network analyzer output for the MCNC comb test structure with a 50 volt DC bias (MUMPS 7).

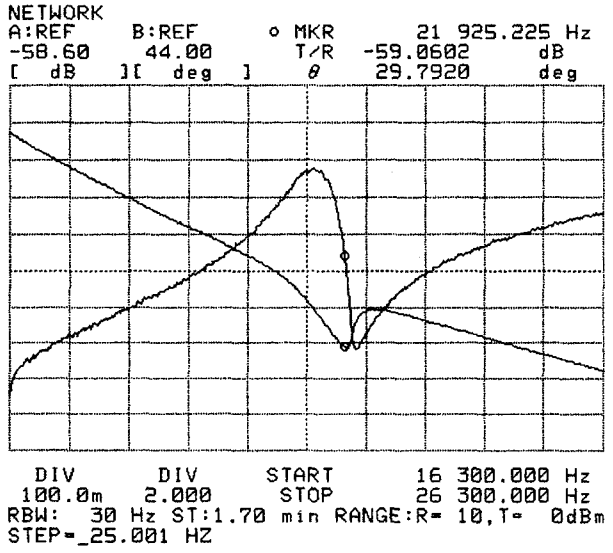

Figure 5.4 Network analyzer output for the MCNC comb test structure with a 75 volt DC bias.

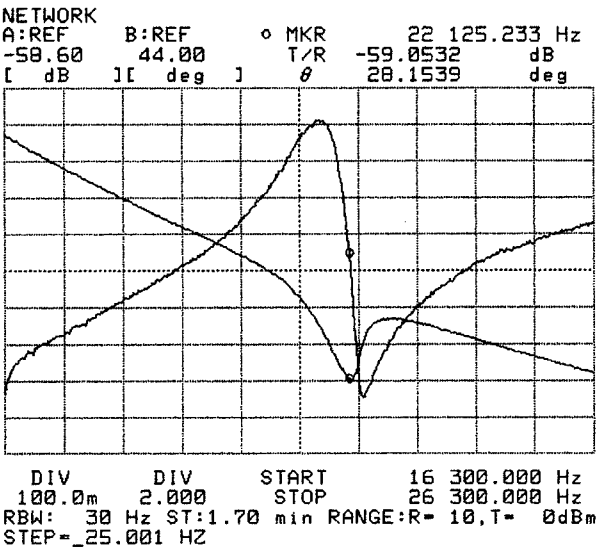

Figure 5.5 Network analyzer output for the MCNC comb test structure with a 100 volt DC bias (MUMPS 7).

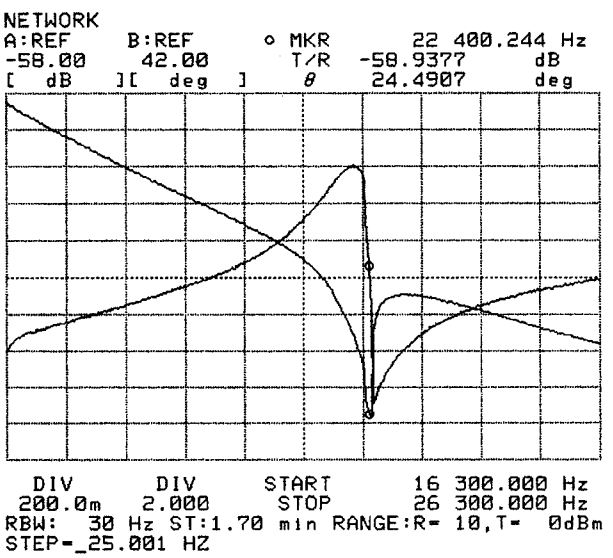

Figure 5.6 Network analyzer output for the MCNC comb test structure with a 125 volt DC bias (MUMPS 7).

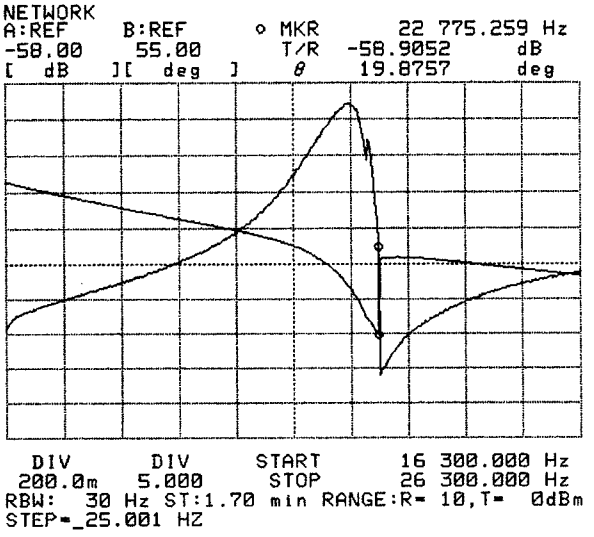

Figure 5.7 Network analyzer output for the MCNC comb test structure with a 150 volt DC bias (MUMPS 7).

of viscous damping decrease. The MCNC test structure was again used to validate the tests. The bias voltage required for an output response to be observable was lowered significantly. In addition, the asymmetries of the resonant spike increased with lower DC bias voltages. The results are shown in Figures 5.8-5.12. Devices on both MUMPS 7 and MUMPS 8 fabrication runs were tested in the vacuum chamber. Resonance for the experimental devices could not be determined using this method.

5.3 Current Monitoring To Identify Resonance.

The current monitoring technique to identify device resonant frequencies has not been tested in this thesis and is left as a possible area for future research.

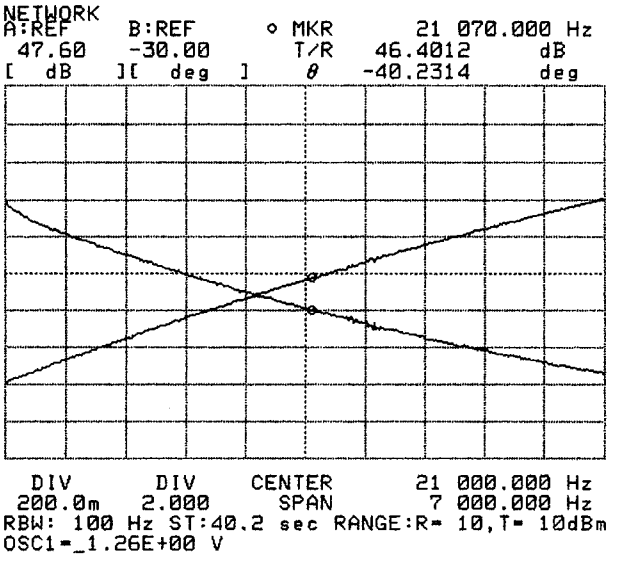

Figure 5.8 Network analyzer output for the MCNC comb test structure with a 0 volt DC bias in a vacuum chamber (MUMPS 7).

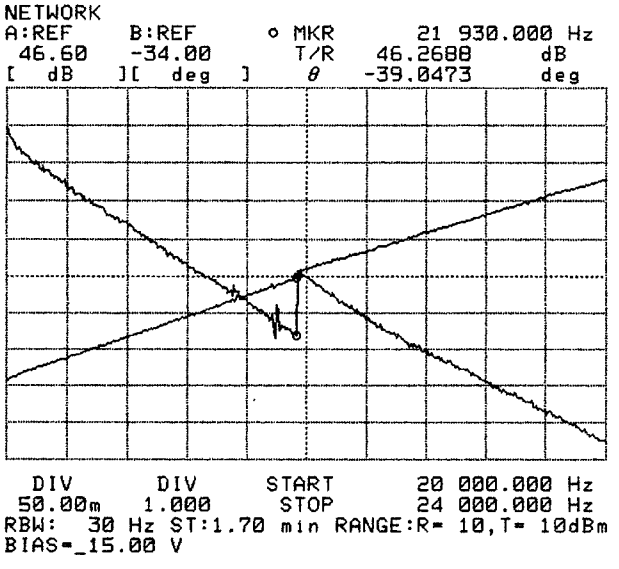

Figure 5.9 Network analyzer output for the MCNC comb test structure with a 15 volt DC bias in a vacuum chamber (MUMPS 7).

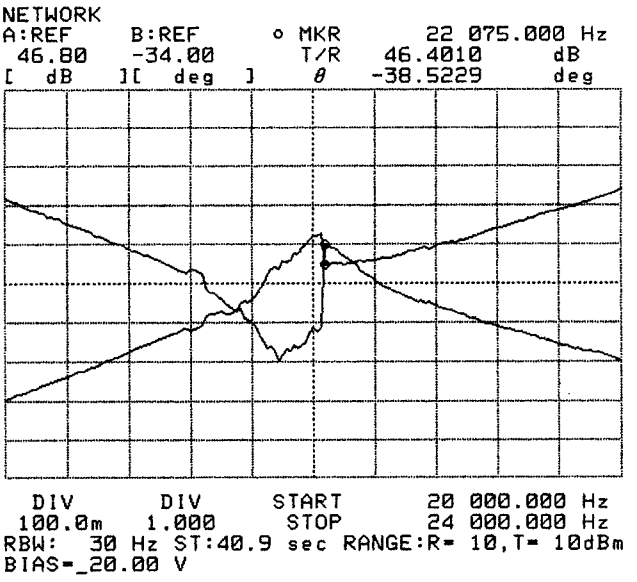

Figure 5.10 Network analyzer output for the MCNC comb test structure with a 20 volt DC bias in a vacuum chamber (MUMPS 7).

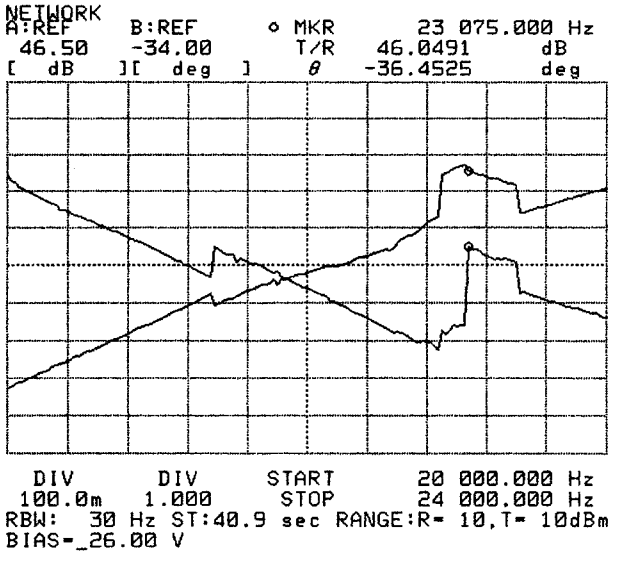

Figure 5.11 Network analyzer output for the MCNC comb test structure with a 26 volt DC bias in a vacuum chamber (MUMPS 7).

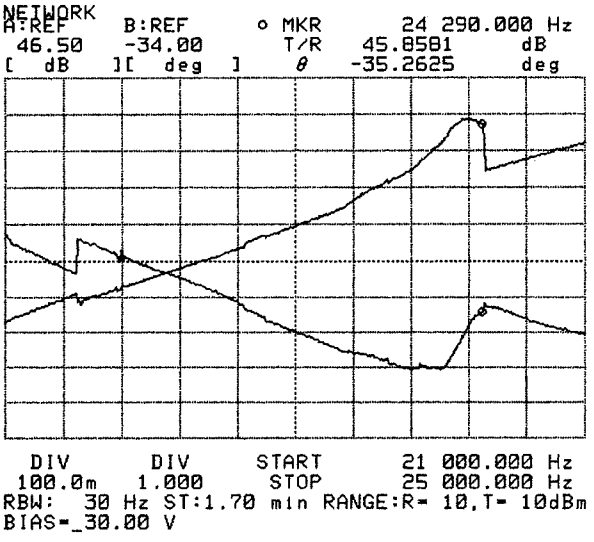

Figure 5.12 Network analyzer output for the MCNC comb test structure with a 30 volt DC bias in a vacuum chamber (MUMPS 7).

5.4 Discussion of MUMPS Fabrication Process.

Four MUMPS fabrication runs were participated in; MUMPS 6, MUMPS 7, MUMPS 8, and MUMPS 9. Of these runs, two were returned without fabrication difficulties; they were the MUMPS 6 and MUMPS 9 fabrication runs. The residual stresses of the material layers in these runs were significantly smaller than those seen in the MUMPS 7 and MUMPS 8 runs. There were four problems with the MUMPS 7 and MUMPS 8 fabrication runs. The first problem was located in places the poly 1 layer and poly 2 layers had been fused. This was not a significant issue for the devices designed as resonators. The second problem, however, caused significant difficulty. Where the topology changes the polysilicon layers will be thicker. As a result, if the polysilicon etch is not long enough, thin lines of polysilicon, called stringers, are left behind. Figure 5.13 shows how stringers are created. Once the die is released these lines stick to the substrate. For electrostatic devices, these thin lines

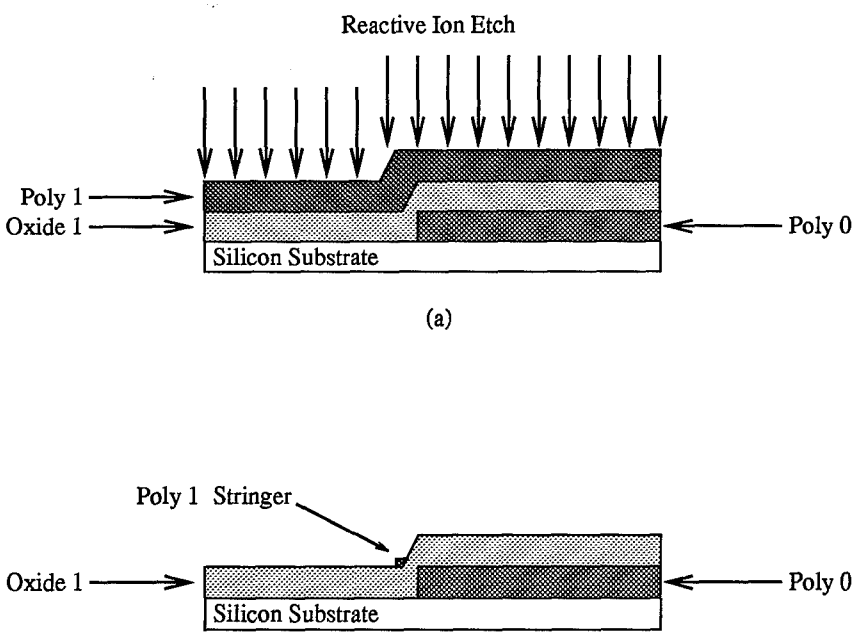

Figure 5.13 Stringer creation in the MUMPS process: (a) Polysilicon is deposited across the wafer and then etched using a reactive ion etch. The polysilicon layer is thicker where contour changes occur, requiring a longer etch time. (b) Stringers are the result of an incomplete reactive ion etch, as shown in this figure.

of polysilicon or stringers align themselves with the electrostatic field. Often the result is shorting from a high potential (150V DC) to a low potential (0V DC). Figure 5.14 shows an MCNC test structure that, because of stringers, would short instantly. The resulting

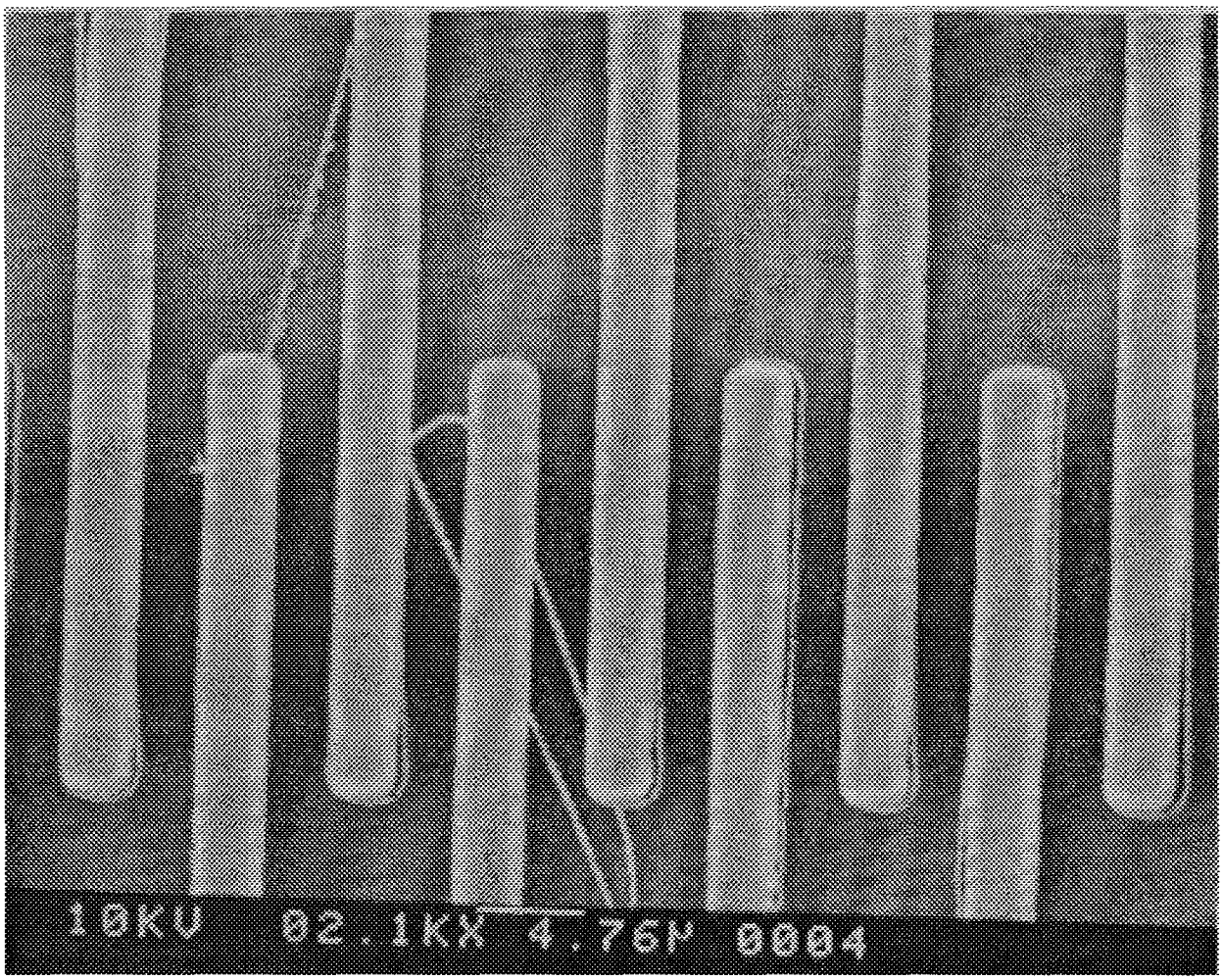

Figure 5.14 Stringers shown shorting the MCNC test structure and making it unusable.

current surge is sufficient to melt the device, probe tips, and often create a significant depression in the substrate. While stringers were present on the MUMPS 7 fabrication run, they were not abundant and therefore had little effect. There were significantly more stringers on MUMPS 8, making device testing difficult and the results questionable. In

addition to stringers, the residual stress of the mechanical layers increased consistently from MUMPS 6 through MUMPS 8 and then decreased again in MUMPS 9. For example, the residual stress of the poly 1 layer increased from a moderate value of 5.6 MPa on MUMPS 6 to approximately 2.5 times that, 14.1 MPa, on MUMPS 8, increasing the device's resonant frequency. The residual stress of the poly 1 layer decreased in MUMPS 9 to 3 MPa. Variations in the residual stress characteristics led to large variations in device resonant frequencies. In addition, the lack of consistency in the residual stress characteristics makes it difficult to design devices with specific resonant frequencies. The third problem encountered may or may not be a fabrication error. It has been observed that a thin film is present over many poly 0 surfaces. This film causes devices to stick in position. They may be moved laterally with probes; however, when probe pressure is removed, the structure stays in its last position. The film causes the devices to stick as a result of increasing the friction present. Several methods were investigated to remove this film, including placing the die in both organic and inorganic solvents. Neither of these methods was effective. It is possible that the film was the result of contaminated DI water or a contamination at the foundry. While the majority of the MCNC test structures functioned on the MUMPS 7 die, only one of 15 structures tested on MUMPS 8 functioned and many others were not tested because of the number of stringers on the structures. The fourth challenge presented by the MCNC fabrication process was the lead time from sending out devices to having them returned. The devices sent out took three months to return on each of the MUMPS 6, MUMPS 7, and MUMPS 8 fabrication runs. The runs were also spaced three months apart. As a result, fabricated devices were returned no more than two or three days before the next run was due to be sent out. There was no time to test

devices between runs. The lead time has been decreased and was two and a half months for the MUMPS 9 fabrication run.

5.5 Discussion of Resonant Frequency Testing Results

The optical and network analyzer methods of testing for device resonant frequency was conducted on devices from the MUMPS 7, MUMPS 8, and MUMPS 9 fabrication runs. The procedures were verified using the MCNC test structure and have proven effective in determining the resonant characteristics of micro mirrors and arrays of those mirrors [36]. There are two possible reasons why the experimental gyroscope devices failed to work. The first possibility is that the flexures provided too large a spring constant. As a result, too large a force was necessary to move the devices both at atmospheric pressure and when in a vacuum. The second possibility is that the suspended mass was large enough to cause the devices to sag and either stick to the substrate or to move the free drive combs out of alignment with the fixed drive combs. Figure 5.15 shows a stacked structure with 12 fingers. The device plate is suspended off the substrate and the combs are still interdigitated. Figure 5.16 shows a double structure with 24 combs, all other geometry features are the same. The picture shows the combs are not interdigitated and the device plate appears to be resting on the substrate. Ten to fifteen devices of each type were investigated, all showed similar results. The consistency in the comb alignment indicates the MUMPS 8 devices have one of three problems. The first possibility is the four flexures in the vibrating members are too long. This is possible as the spring constant in the vertical direction is identical to the spring constant in the lateral direction. The second possibility is the length of the output flexure may be too large, resulting in enough sag

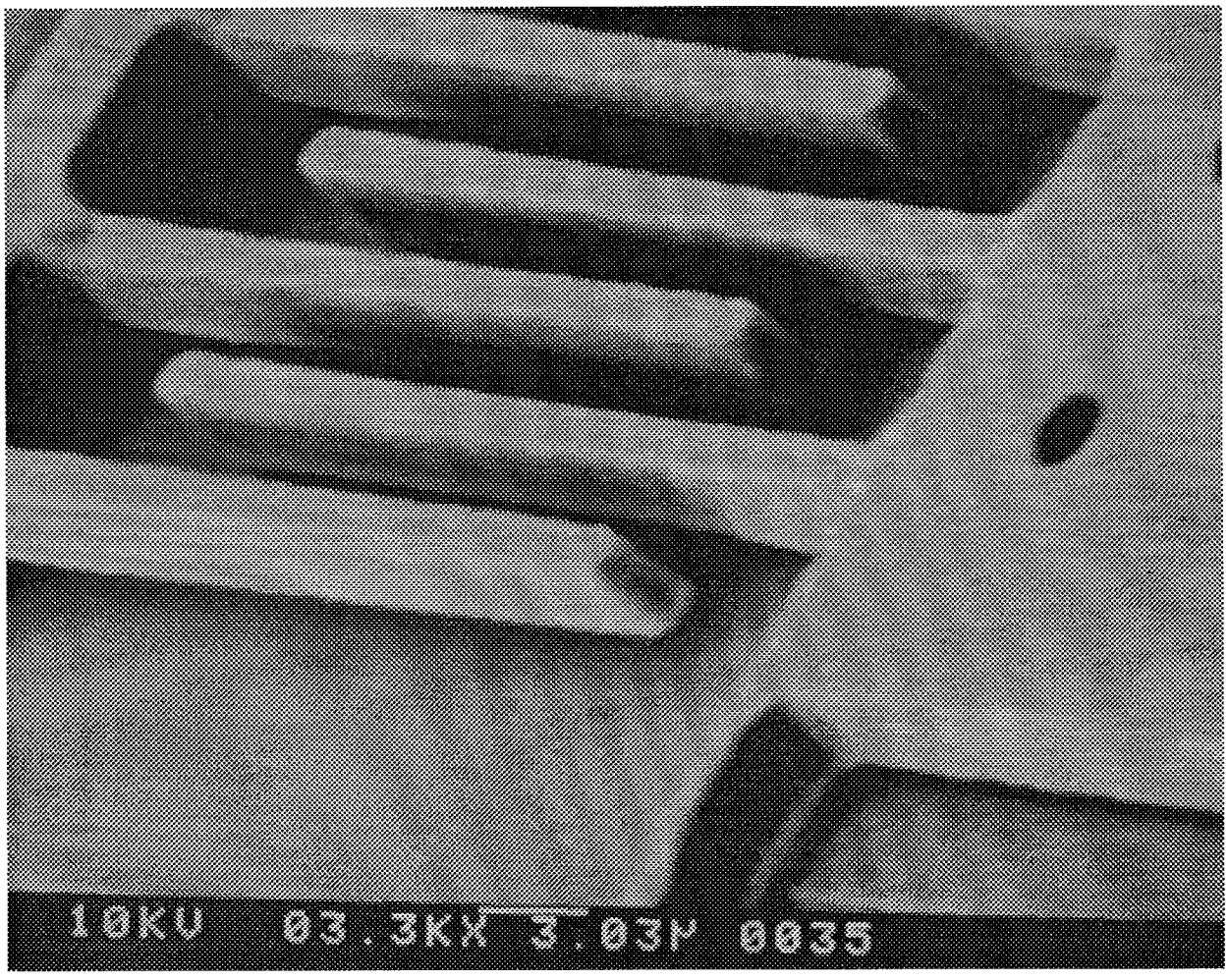

Figure 5.15 Stacked comb 6 structure showing the overlap of the combs (MUMPS 8).

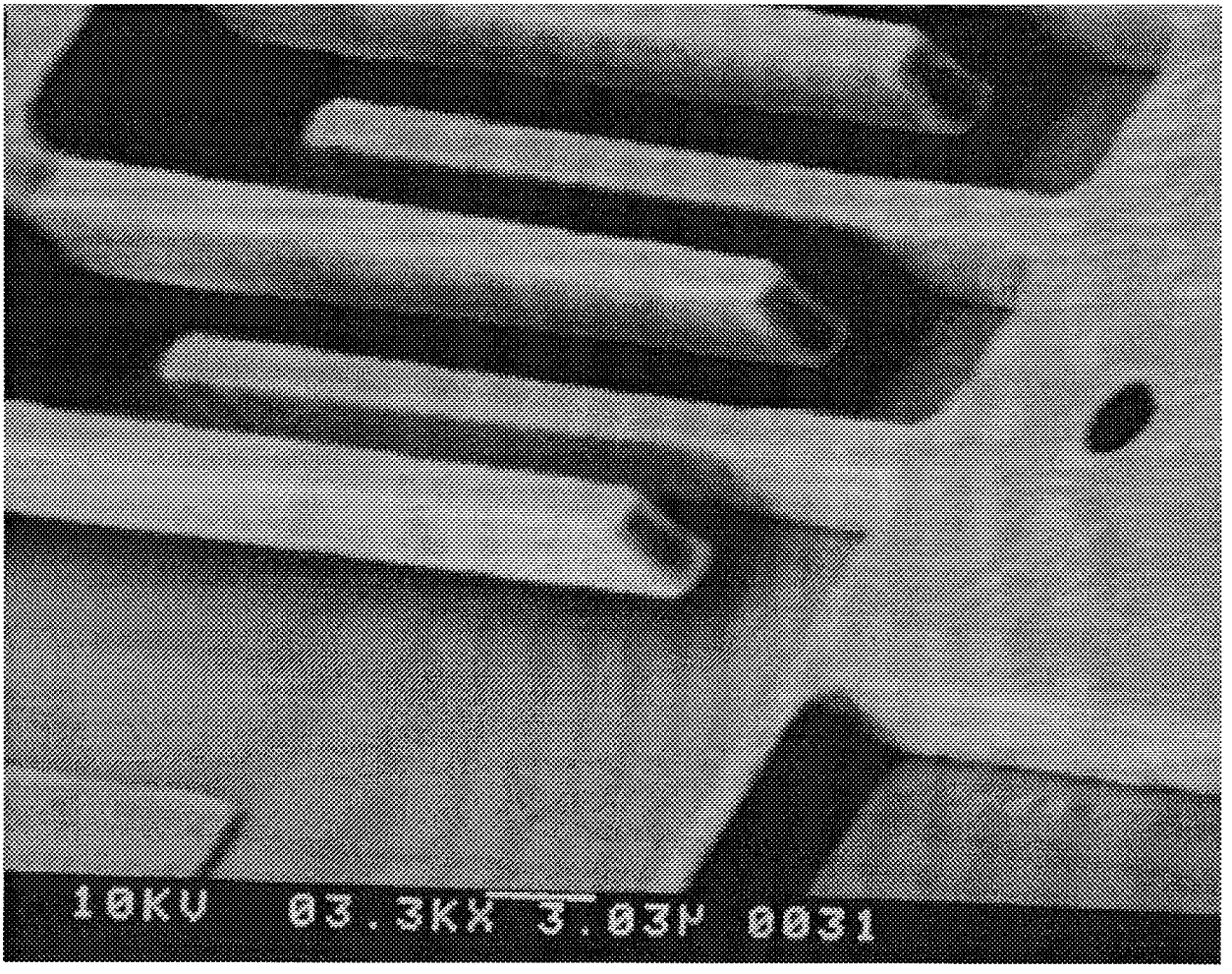

Figure 5.16 Stacked comb 5 structure showing the sagging of the device plate (MUMPS 8).

to lower the combs. The amount of drive force generated is decreased linearly with the decreasing overlap area of the combs. The third possibility is that stiction caused the structures to stick to the substrate. The devices were located in different quadrants of the die. Stiction may have been a larger factor in one quadrant than in the other. The Comb gyroscope designs developed for the MUMPS 9 fabrication run were based on a high residual stress value. The MUMPS 9 run ended up having a low residual stress value. As a result, the devices sagged and stuck to the substrate.

The ring gyroscopes in the MUMPS 7 and MUMPS 8 fabrication runs did not illustrate as consistent a result. Some rings were suspended off the substrate as expected and others were not. The inconsistencies indicate the cause as stiction. Methods have been developed to minimize the effects of stiction [30]. One such method places the die in a pressure chamber. Any liquid on the die is sublimated using liquid carbon dioxide. The chamber is then brought to a pressure consistent with the triple point of carbon dioxide. The triple point refers to the temperature and pressure where a substance may exist in the liquid, gas, and solid phases. The carbon dioxide then transitions from a liquid to a gas instantaneously. Using this method, a 100 percent successful release rate has been reported [30]. The ring gyroscope design included on MUMPS 9 had twice the diameter. Again the choice to increase the diameter was based on the high residual stress of the previous two runs. The lower stress in MUMPS 9 caused these devices to sag and stick to the substrate.

The planar gyroscope designs on the MUMPS 7 and MUMPS 8 fabrication runs were tested using the both the optical and network analyzer methods. Resonance could not be determined applying these methods. The outer flexures on these designs may have been

too short to twist properly. The MUMPS 9 planar gyroscope designs were based on a high residual stress. With the lower residual stress encountered these devices sagged and stuck to the substrate.

5.6 Chapter Summary

This chapter presented the experimental verification of two methods to determine device resonant frequencies. The first was the optical method. This approach leads to a good initial estimate of the device resonant frequency. The second used a network analyzer to measure the output over input transfer function. This method provides a more accurate measure of resonant frequency. Using the network analyzer a dependence of resonant frequency on bias voltage was observed along with the effects of testing devices in a vacuum. Both the optical method and the network analyzer methods were applied to experimental gyroscope designs. The resonant frequency of the experimental gyroscopes could not be identified using either method. Possible reasons for the difficulty in determining the device resonant frequency and suggested solutions are provided in Chapter 6.

VI. Conclusions and Recommendations

This chapter presents conclusions and recommendations based on the information in previous chapters. The conclusions drawn from this work are presented first followed by recommendations for future research in this area.

6.1 Conclusions

This thesis investigated the use of a commercial fabrication process to fabricate a micromachined gyroscope capable of being integrated into an INS / GPS system providing accurate position and velocity data. The advantages of the micromachined gyroscopes are the low cost and small size of the devices. Three different designs were investigated: the vibrating comb gyroscope, the vibrating ring gyroscope, and the planar gyroscope. Operational theory was developed, from first principals, for the vibrating comb and planar gyroscopes. The ring gyroscope theory was initially developed at the University of Michigan [7]. Modifications, however, had to be made for changes in the drive and sense mechanisms.

The commercial fabrication process available was MCNC's MUMPS process. Designs were submitted for four fabrication runs MUMPS 6-MUMPS 9. Of the returned test die, the MUMPS 6 and MUMPS 9 runs had the least number of fabrication errors and the lowest residual stresses. There was considerable variation in the parameters of each fabrication run, making it difficult to design devices for a specific resonant frequency. Stringers were found on both the MUMPS 7 and MUMPS 8 fabrication runs. The stringers presented a larger problem on the MUMPS 8 run, causing electrical shorts that resulted in destruction

of devices and probes. Before a commercial fabrication process may be used to create test devices or mass produce devices, it must be able to produce consistent reliable results. The MCNC process has not been able to meet these criteria.

Three methods were used in an attempt to evaluate device resonant frequency: optical detection, network analyzer measurements, and current monitoring. The current monitoring tests have not been completed and are left as an area for future research. The procedures used in optical detection and network analyzer measurements were verified through the use of a test comb drive resonator structure included on each die by MCNC. The procedures were then applied to the experimental gyroscope structures. The resonant frequencies for the vibrating comb gyroscope, the vibrating ring gyroscope, and the planar gyroscope could not be determined using either of the first two methods. There are several possible explanations for the inability to identify the resonant frequency. For the vibrating comb gyroscopes:

- The flexures may be too stiff; as a result too much energy is required to drive the device.
- The overlap of the fixed and free combs may be reduced enough by sag to increase the energy required beyond the capabilities of the equipment available.
- Stiction may be causing devices to stick to the substrate, making them unusable.

On the vibrating ring gyroscope, the flexures may be too thin, causing the device to sag, resulting in stiction or in moving the drive combs out of position, reducing the applied force. In addition, the drive force is applied over a larger arc length than on the devices developed at the University of Michigan. As a result, the effect of applying an equal force

is less on devices designed for this thesis. The following section provides recommendations for continuing research in this area.

6.2 Recommendations

This section provides a set of recommendations that may prove helpful in continuing research in this area.

1. Verify and attempt resonant frequency identification using the current monitoring method outlined in Chapter 4.
2. Investigate other possible fabrication sites.
3. Develop test structures investigating the maximum mass that can be suspended using a suspension identical to that of the comb gyroscope. The devices placed on the MUMPS 7 test die appear to be too stiff and devices on the MUMPS 8 and MUMPS 9 test die appear to be too loose, resulting in devices sagging.
4. Develop test structures investigating the effects of varying the support springs in the ring gyroscope. Attempt both thinner and thicker support flexures; observe the effects these changes have on the comb alignment.
5. Shorten the torsion bar length of the comb 3 - comb 6 gyroscopes. The device sag may be a result of too much mass suspended from these flexures.
6. The overetch of poly 2 is sufficient to make a poly 1, poly 2, poly 0 stacked structure. Create fixed combs from there three layers to maximize comb interface area and, as a result, maximize the applied force.

7. Alternative flexure designs should be investigated. Wander springs have been used with success in lateral resonators [37]. The effects of the output torque on this type of flexure should first be investigated.

8. Improvements may also be made to the comb drive mechanism. The comb drives as implemented result in a vertical as well as horizontal applied force. Methods have been developed to suppress the levitation effect and attain a pure horizontal force [30].

9. Attain access to high voltage dc supplies and ac oscillators to maximize the energy applied to the gyroscopes.

10. Initially it was thought the devices were suspended a sufficient height off the substrate. Tests have indicated this is not true and methods of preventing stiction must be implemented. Two methods have been used successfully on previous designs:

    (a) Place small depressions in the poly 2 structures using the dimple layer to minimize the area that results in stiction.

    (b) Place a large plane under the suspended structure at equal potential.

This thesis establishes a base for research in the micromachined gyroscope area using a commercial fabrication process. An overview of three device designs has been provided; in continuing this research, a narrower focus is necessary. Many opportunities exist to continue this research at all levels to include: Attempt to increase the mass of the planar gyroscope designs to increase output sensistivity, re-design of the flexure systems for the comb and ring gyroscopes, and alterations to the comb drive mechanisms. In addition

effort must be dedicated to developing low noise sense circuitry and a means of interfacing that circuitry with the test micromachined structure.

Appendix A. Vibrating Comb Gyroscope Output Derivations

In this appendix, generic equations will be derived for the compound accelerations and equations for output torque generated for Figure A.1 In Figure A.1, CML and CMR

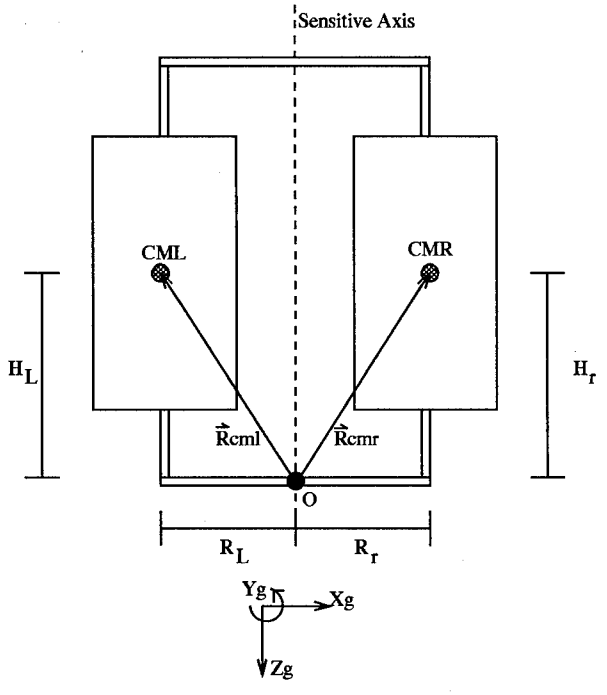

Figure A.1 Block diagram for generic torque derivations

represent the left and right centers of mass. Position vectors to CML and CMR are defined in Equations (A.1) and (A.2). The input rotation, ω_{in}, will be defined by Equation (A.3):

$$\vec{R}_L = -(r_L + \Omega sin(\omega t)\hat{x}_g + b_L\hat{y}_g - H_L\hat{z}_g \tag{A.1}$$

$$\vec{R}_r = -(r_r + \Omega sin(\omega t)\hat{x}_g + b_r\hat{y}_g - H_r\hat{z}_g \tag{A.2}$$

$$\omega_{in} = \begin{bmatrix} \omega_x \\ \omega_y \\ \omega_z \end{bmatrix} \tag{A.3}$$

The acceleration that results from an input rotation ω_{in} is calculated using the same method as in the Coriolis acceleration example. First the acceleration experienced by the left vibrating member is calculated. The calculation for the acceleration of the right vibrating member follows.

$$\vec{V}_L = \frac{^i d}{dt} R_L^g = \frac{^g d}{dt} R_L^g + \omega_{in} \times R_L^g \tag{A.4}$$

$$\begin{aligned}\vec{V}_L = {} & [-\dot{\Omega} sin(\omega t) - \Omega \omega cos(\omega t) - H_L \omega_y - b_L \omega_z]\hat{x}_g \\ & + [-H_L \omega_x + [r_L + \Omega sin(\omega t)]\omega_z]\hat{y}_g \\ & + [b_L \omega_x + [r_L + \Omega sin(\omega t)]\omega_y]\hat{z}_g \end{aligned} \tag{A.5}$$

$$\vec{A}_L = \frac{^i d}{dt} V_L^g = \frac{^g d}{dt} V_L^g + \omega_{in} \times V_L^g \tag{A.6}$$

$$\begin{aligned}\vec{A}_L = {} & [[-\ddot{\Omega} + [\omega^2 + \omega_y^2 - \omega_z^2]\Omega] sin(\omega t) - [2\dot{\Omega}\omega + \Omega\dot{\omega}] cos(\omega t) \\ & + [\omega_x \omega_y - \dot{\omega_z}] b_L + [\dot{\omega_y} - \omega_x \omega_z] H_L + [\omega_y^2 - \omega_z^2] r_L]\hat{x}_g \\ & + [[2\omega_z \dot{\Omega} + (\omega_x \omega_y + \dot{\omega_z})\Omega] sin(\omega t) + 2\Omega\omega_z \omega cos(\omega t) \\ & + [\omega_x^2 + \omega_z^2] b_L + [\omega_y \omega_z - \dot{\omega_x}] H_L + [\omega_x \omega_y + \dot{\omega_z}] r_L]\hat{y}_g \\ & + [[2\omega_y \dot{\Omega} + [\dot{\omega_y} + \omega_z \omega_x]\Omega] sin(\omega t) + 2\Omega\omega_y \omega cos(\omega t) \\ & + [\dot{\omega_x} + \omega_y \omega_z] b_L + [-\omega_x^2 + \omega_y^2] H_L + [\omega_x \omega_z + \dot{\omega_y}] r_L]\hat{z}_g \end{aligned} \tag{A.7}$$

The acceleration of the right member's center of mass is:

$$\vec{V}_r = \frac{^i d}{dt} R_r^g = \frac{^g d}{dt} R_r^g + \omega_{in} \times R_r^g \tag{A.8}$$

$$\vec{V}_r = [\dot{\Omega}sin(\omega t) + \Omega\omega cos(\omega t) - H_r\omega_y - b_r\omega_z]\hat{x}_g$$

$$+[-H_r\omega_x - [r_r + \Omega sin(\omega t)]\omega_z]\hat{y}_g$$

$$+[b_r\omega_x - [r_r + \Omega sin(\omega t)]\omega_y]\hat{z}_g \qquad \text{(A.9)}$$

$$\vec{A}_r = \frac{^i d}{dt}V_r^g = \frac{^g d}{dt}V_r^g + \omega_{in} \times V_r^g \qquad \text{(A.10)}$$

$$\vec{A}_r = [[\ddot{\Omega} + [-\omega^2 - \omega_y^2 + \omega_z^2]\Omega]sin(\omega t) + [2\dot{\Omega}\omega + \Omega\dot{\omega}]cos(\omega t)$$

$$+[\omega_x\omega_y - \dot{\omega}_z]b_r + [-\dot{\omega}_y + \omega_x\omega_z]H_r + [-\omega_y^2 + \omega_z^2]r_r]\hat{x}_g$$

$$+[-[2\omega_z\dot{\Omega} + (\omega_x\omega_y + \dot{\omega}_z)\Omega]sin(\omega t) - 2\Omega\omega_z\omega cos(\omega t)$$

$$+[\omega_x^2 + \omega_z^2]b_r + [\omega_y\omega_z - \dot{\omega}_x]H_r + [-\omega_x\omega_y - \dot{\omega}_z]r_r]\hat{y}_g$$

$$+[-[2\omega_y\dot{\Omega} + [\dot{\omega}_y + \omega_z\omega_x]\Omega]sin(\omega t) - 2\Omega\omega_y\omega cos(\omega t)$$

$$+[\dot{\omega}_x + \omega_y\omega_z]b_r + [-\omega_x^2 + \omega_y^2]H_r + [-\omega_x\omega_z - \dot{\omega}_y]r_r]\hat{z}_g \qquad \text{(A.11)}$$

The acceleration of the mass centers causes a net torque about the output axis. The definition of torque is repeated here:

$$\vec{T} = \vec{R} \times \vec{F} \qquad \text{(A.12)}$$

$$\vec{F} = m\vec{A} \qquad \text{(A.13)}$$

The torque from the left vibrating member is:

$$\vec{T_L^g} = \vec{R_L^g} \times \vec{F_L^g} \qquad \text{(A.14)}$$

$$\vec{T_L^g} = [b_L m_L[[2\omega_y\dot{\Omega} + [\dot{\omega}_y + \omega_z\omega_x]\Omega]sin(\omega t) + 2\Omega\omega_y\omega cos(\omega t)$$

$$+[\dot{\omega}_x + \omega_y\omega_z]b_L + [-\omega_x^2 + \omega_y^2]H_L + [\omega_x\omega_z + \dot{\omega}_y]r_L]$$

$$+H_L m_L[[2\omega_z\dot{\Omega} + (\omega_x\omega_y + \dot{\omega}_z)\Omega]sin(\omega t) + 2\Omega\omega_z\omega cos(\omega t)$$

$$+[\omega_x^2 + \omega_z^2]b_L + [\omega_y\omega_z - \dot{\omega}_x]H_L + [\omega_x\omega_y + \dot{\omega}_z]r_L]]\hat{x}_g$$

$$+[(r_L + \Omega sin(\omega t))m_L[-[2\omega_y\dot{\Omega} + [\dot{\omega}_y + \omega_z\omega_x]\Omega]sin(\omega t) - 2\Omega\omega_y\omega cos(\omega t)$$

$$-[\dot{\omega}_x + \omega_y\omega_z]b_L - [-\omega_x^2 + \omega_y^2]H_L - [\omega_x\omega_z + \dot{\omega}_y]r_L]$$

$$+H_L m_L[[-\ddot{\Omega} + [\omega^2 + \omega_y^2 - \omega_z^2]\Omega]sin(\omega t) - [2\dot{\Omega}\omega + \Omega\dot{\omega}]cos(\omega t)$$

$$+[\omega_x\omega_y - \dot{\omega}_z]b_L + [\dot{\omega}_y - \omega_x\omega_z]H_L + [\omega_y^2 - \omega_z^2]r_L]\hat{y}_g$$

$$+[(r_L + \Omega sin(\omega t))m_L[-[2\omega_z\dot{\Omega} + (\omega_x\omega_y + \dot{\omega}_z)\Omega]sin(\omega t) - 2\Omega\omega_z\omega cos(\omega t)$$

$$-[\omega_x^2 + \omega_z^2]b_L - [\omega_y\omega_z - \dot{\omega}_x]H_L - [\omega_x\omega_y + \dot{\omega}_z]r_L]$$

$$-b_L m_L[[-\ddot{\Omega} + [\omega^2 + \omega_y^2 - \omega_z^2]\Omega]sin(\omega t) - [2\dot{\Omega}\omega + \Omega\dot{\omega}]cos(\omega t)$$

$$+[\omega_x\omega_y - \dot{\omega}_z]b_L + [\dot{\omega}_y - \omega_x\omega_z]H_L + [\omega_y^2 - \omega_z^2]r_L]]\hat{z}_g \qquad \text{(A.15)}$$

The torque from the right vibrating member is:

$$\vec{T_r^g} = \vec{R_r^g} \times \vec{F_r^g} \qquad \text{(A.16)}$$

$$\vec{T_r^g} = [b_r m_r[-[2\omega_y\dot{\Omega} + [\dot{\omega}_y + \omega_z\omega_x]\Omega]sin(\omega t) - 2\Omega\omega_y\omega cos(\omega t)$$

$$+[\dot{\omega}_x + \omega_y\omega_z]b_r + [-\omega_x^2 + \omega_y^2]H_r + [-\omega_x\omega_z - \dot{\omega}_y]r_r]$$

$$+H_r m_r[-[2\omega_z\dot{\Omega} + (\omega_x\omega_y + \dot{\omega}_z)\Omega]sin(\omega t) - 2\Omega\omega_z\omega cos(\omega t)$$

$$+[\omega_x^2 + \omega_z^2]b_r + [\omega_y\omega_z - \dot{\omega}_x]H_r + [-\omega_x\omega_y - \dot{\omega}_z]r_r]]\hat{x}_g$$

$$+[[r_r + \Omega sin(\omega t)]m_r[-[2\omega_y\dot{\Omega} + [\dot{\omega}_y + \omega_z\omega_x]\Omega]sin(\omega t) - 2\Omega\omega_y\omega cos(\omega t)$$

$$+[\dot{\omega}_x + \omega_y\omega_z]b_r + [-\omega_x^2 + \omega_y^2]H_r + [-\omega_x\omega_z - \dot{\omega}_y]r_r]$$

$$+H_r m_r[[\ddot{\Omega} + [-\omega^2 - \omega_y^2 + \omega_z^2]\Omega]sin(\omega t) + [2\dot{\Omega}\omega + \Omega\dot{\omega}]cos(\omega t)$$

$$+[\omega_x\omega_y - \dot{\omega}_z]b_r + [-\dot{\omega}_y + \omega_x\omega_z]H_r + [-\omega_y^2 + \omega_z^2]r_r]\hat{y}_g$$

$$+[[r_r + \Omega sin(\omega t)]m_r[-[2\omega_z\dot{\Omega} + (\omega_x\omega_y + \dot{\omega}_z)\Omega]sin(\omega t) - 2\Omega\omega_z\omega cos(\omega t)$$

$$+[\omega_x^2 + \omega_z^2]b_r + [\omega_y\omega_z - \dot{\omega}_x]H_r + [-\omega_x\omega_y - \dot{\omega}_z]r_r]$$

$$-b_r m_r[[\ddot{\Omega} + [-\omega^2 - \omega_y^2 + \omega_z^2]\Omega]sin(\omega t) + [2\dot{\Omega}\omega + \Omega\dot{\omega}]cos(\omega t)$$

$$+[\omega_x\omega_y - \dot{\omega}_z]b_r + [-\dot{\omega}_y + \omega_x\omega_z]H_r + [-\omega_y^2 + \omega_z^2]r_r]]\hat{z}_g \qquad \text{(A.17)}$$

The net torque generated is given by:

$$\vec{T}_{tot}^{g} = \vec{T}_L^g + \vec{T}_r^g \qquad \text{(A.18)}$$

In the derivation of the torque generated, the mass centers were allowed to be different distances from the origin. The device was not symmetric about the x_g, y_g, or, z_g axes. With modern fabrication facilities and the ability to laser tune devices, the mass centers may be assumed to be located an equal distance from the origin, resulting in symmetry about the sensitive axis. In addition, the mass of the two members will be the same. Under these assumptions, the following simplifications may be made:

$$H_L = H_r = H \qquad \text{(A.19)}$$

$$r_L = r_r = r \qquad \text{(A.20)}$$

$$b_L = b_r = b \qquad \text{(A.21)}$$

$$m_L = m_r = m \tag{A.22}$$

The net torque $\vec{T}^g_{tot}$ is:

$$\begin{aligned}
\vec{T}^g_{tot} = 2m[[(\dot{\omega}_x + \omega_y\omega_z)b^2 + (\omega_y^2 + \omega_z^2)Hb + (\omega_y\omega_z - \dot{\omega}_x)H^2]\hat{x}_g \\
+[(r + \Omega sin(\omega t))[-[2\omega_y\dot{\Omega} + [\dot{\omega}_y + \omega_z\omega_x]\Omega]sin(\omega t) - 2\Omega\omega_y\omega cos(\omega t) \\
-[\omega_x\omega_z + \dot{\omega}_y]r] + [\omega_x\omega_y - \dot{\omega}_z]Hb]\hat{y}_g \\
+[(r + \Omega sin(\omega t))[-[2\omega_z\dot{\Omega} + (\omega_x\omega_y + \dot{\omega}_z)\Omega]sin(\omega t) - 2\Omega\omega_z\omega cos(\omega t)] \\
-[\omega_x\omega_y - \dot{\omega}_z]b^2]\hat{z}_g]
\end{aligned} \tag{A.23}$$

The above case allows for a displacement of the mass center of the system in the $\hat{y}_g$ direction. This equation may be further simplified by assuming a uniform mass distribution in the vibrating members. The result of this assumption is a zero displacement of the position vectors in the y_g direction and symmetry about a line joining the two mass centers. To account for this in the equations, let $b = 0$. The output torque then becomes:

$$\begin{aligned}
\vec{T}^g_{tot} = 2m[[(\omega_y\omega_z - \dot{\omega}_x)H^2]\hat{x}_g \\
+[(r + \Omega sin(\omega t))[-[2\omega_y\dot{\Omega} + [\dot{\omega}_y + \omega_z\omega_x]\Omega]sin(\omega t) \\
-2\Omega\omega_y\omega cos(\omega t) - [\omega_x\omega_z + \dot{\omega}_y]r]\hat{y}_g \\
+[(r + \Omega sin(\omega t))[-[2\omega_z\dot{\Omega} + (\omega_x\omega_y + \dot{\omega}_z)\Omega]sin(\omega t) \\
-2\Omega\omega_z\omega cos(\omega t) - [\omega_x\omega_y + \dot{\omega}_z]r]\hat{z}_g]
\end{aligned} \tag{A.24}$$

This is the final form for the output torque that will need to be implemented for arbitrary rotations. In order to verify the single axis rotation equation presented in Chapter 3, let the input rotation be only about the z_g axis, and let there be no change in the maximum amplitude of the sustained oscillation, so:

$$\omega_x = \omega_y = \dot{\Omega} = 0 \tag{A.25}$$

the output torque becomes:

$$\vec{T}^g_{tot} = 2m[(r + \Omega sin(\omega t))[-\dot{\omega}_z(r + \Omega sin(\omega t)) - 2\Omega\omega_z\omega cos(\omega t)]]\hat{z}_g \tag{A.26}$$

This is identical to the result from Chapter 3 for an input rotation rate of ω_o.

Appendix B. Planar Gyroscope Output Derivations

The full derivation of the planar gyroscope torque equations is presented for an arbitrary input rotation. The position vectors to the mass centers are shown in Figure B.1. The four position vectors R_1, R_2, R_3, and R_4 are defined by Equations (B.1-B.4).

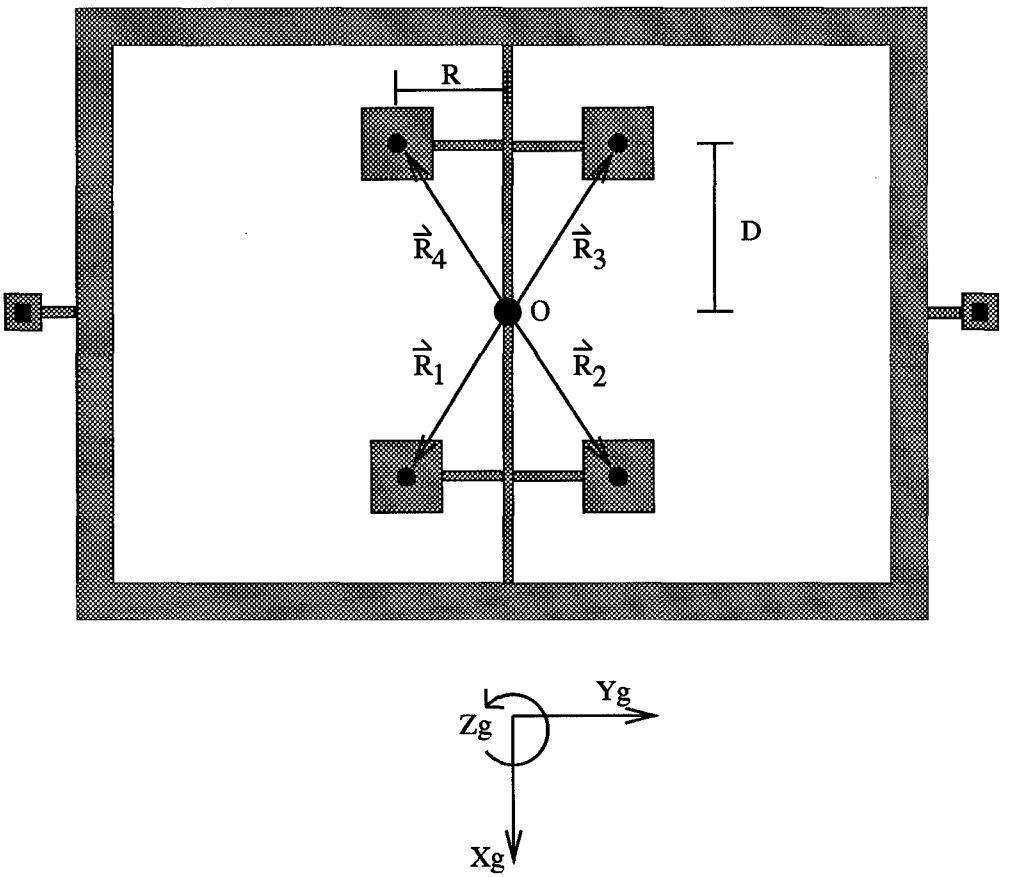

Figure B.1 Block diagram for generic torque derivations planar gyroscope.

$$R_1 = \begin{bmatrix} D \\ -R \\ 0 \end{bmatrix} \tag{B.1}$$

$$R_2 = \begin{bmatrix} D \\ R \\ 0 \end{bmatrix} \tag{B.2}$$

$$R_3 = \begin{bmatrix} -D \\ R \\ 0 \end{bmatrix} \tag{B.3}$$

$$R_4 = \begin{bmatrix} -D \\ -R \\ 0 \end{bmatrix} \tag{B.4}$$

The sustained oscillation is defined by Equation (B.5):

$$\Delta y = \Omega sin(\omega t)\hat{y}_g \tag{B.5}$$

Let the input rotation be defined by Equation (B.6):

$$\vec{\omega}_{in} = \begin{bmatrix} \omega_x \\ \omega_y \\ \omega_z \end{bmatrix} \tag{B.6}$$

This results in a net rotation rate with respect to inertial space given in Equation (B.7):

$$\vec{\omega} = \begin{bmatrix} \omega_x \\ \omega_y + \omega\Omega cos(\omega t) \\ \omega_z \end{bmatrix} \tag{B.7}$$

The inertial accelerations of each of the four position vectors are then calculated and shown in Equations (B.8-B.11):

$$\begin{aligned} A_1 = [R\dot{\omega}_z + (\omega_y + \omega\Omega cos(\omega t))(-R\omega_x - D\omega_y - D\omega\Omega cos(\omega t)) + D\omega_z^2]\hat{x}_g \\ +[-D\dot{\omega}_z - R\omega_x^2 - D\omega_x\omega_y - D\omega_x\omega\Omega cos(\omega t) - R\omega_z^2]\hat{y}_g \\ +[-R\dot{\omega}_x - D\dot{\omega}_y - D\dot{\omega}\Omega cos(\omega t) + D\omega^2\Omega sin(\omega t) - D\omega_x\omega_z - R\omega_z\omega_y \\ -R\omega_z\omega\Omega cos(\omega t)]\hat{z}_g \end{aligned} \tag{B.8}$$

$$\begin{aligned} A_2 = [-R\dot{\omega}_z + (\omega_y + \omega\Omega cos(\omega t))(R\omega_x - D\omega_y - D\omega\Omega cos(\omega t)) + D\omega_z^2]\hat{x}_g \\ +[-D\dot{\omega}_z + R\omega_x^2 - D\omega_x\omega_y - D\omega_x\omega\Omega cos(\omega t) + R\omega_z^2]\hat{y}_g \\ +[R\dot{\omega}_x - D\dot{\omega}_y - D\dot{\omega}\Omega cos(\omega t) + D\omega^2\Omega sin(\omega t) - D\omega_x\omega_z + R\omega_z\omega_y \\ +R\omega_z\omega\Omega cos(\omega t)]\hat{z}_g \end{aligned} \tag{B.9}$$

$$\begin{aligned} A_3 = [-R\dot{\omega}_z + (\omega_y + \omega\Omega cos(\omega t))(R\omega_x + D\omega_y + D\omega\Omega cos(\omega t)) - D\omega_z^2]\hat{x}_g \\ +[D\dot{\omega}_z + R\omega_x^2 + D\omega_x\omega_y + D\omega_x\omega\Omega cos(\omega t) + R\omega_z^2]\hat{y}_g \\ +[R\dot{\omega}_x + D\dot{\omega}_y + D\dot{\omega}\Omega cos(\omega t) - D\omega^2\Omega sin(\omega t) + D\omega_x\omega_z + R\omega_z\omega_y \\ +R\omega_z\omega\Omega cos(\omega t)]\hat{z}_g \end{aligned} \tag{B.10}$$

$$\begin{aligned} A_4 = [R\dot{\omega}_z + (\omega_y + \omega\Omega cos(\omega t))(-R\omega_x + D\omega_y + D\omega\Omega cos(\omega t)) - D\omega_z^2]\hat{x}_g \\ +[D\dot{\omega}_z - R\omega_x^2 + D\omega_x\omega_y + D\omega_x\omega\Omega cos(\omega t) - R\omega_z^2]\hat{y}_g \end{aligned}$$

$$+[-R\dot{\omega}_x + D\dot{\omega}_y + D\dot{\omega}\Omega cos(\omega t) - D\omega^2\Omega sin(\omega t) + D\omega_x\omega_z - R\omega_z\omega_y$$

$$-R\omega_z\omega\Omega cos(\omega t)]\hat{z}_g \qquad \text{(B.11)}$$

Using the derived accelerations and the definition of torque, the torques generated by each of the mass centers are calculated and given in Equations (B.12-B.15):

$$\begin{aligned}
T_1 = m[&[R^2\dot{\omega}_x + DR\dot{\omega}_y + DR\dot{\omega}\Omega cos(\omega t) - DR\omega^2\Omega sin(\omega t) \\
&+DR\omega_x\omega_z + R^2\omega_y\omega_z + R^2\omega_z\omega\Omega cos(\omega t)]\hat{x}_g \\
&+[-RD\dot{\omega}_x - D^2\dot{\omega}_y - D^2\dot{\omega}\Omega cos(\omega t) + D^2\omega^2\Omega sin(\omega t) \\
&-D^2\omega_x\omega_z - DR\omega_y\omega_z - DR\omega_z\omega\Omega cos(\omega t)]\hat{y}_g \\
&+[-D^2\dot{\omega}_z - DR\omega_x^2 - D^2\omega_x\omega_y - D^2\omega_x\omega\Omega cos(\omega t) + R^2\dot{\omega}_z \\
&+(\omega_y + \omega\Omega cos(\omega t)(-R^2\omega_x - DR\omega_y - DR\omega\Omega cos(\omega t))]\hat{z}_g]
\end{aligned} \qquad \text{(B.12)}$$

$$\begin{aligned}
T_2 = m[&[R^2\dot{\omega}_x - DR\dot{\omega}_y - DR\dot{\omega}\Omega cos(\omega t) + DR\omega^2\Omega sin(\omega t) \\
&-DR\omega_x\omega_z + R^2\omega_y\omega_z + R^2\omega_z\omega\Omega cos(\omega t)]\hat{x}_g \\
&+[RD\dot{\omega}_x - D^2\dot{\omega}_y - D^2\dot{\omega}\Omega cos(\omega t) + D^2\omega^2\Omega sin(\omega t) \\
&-D^2\omega_x\omega_z + DR\omega_y\omega_z + DR\omega_z\omega\Omega cos(\omega t)]\hat{y}_g \\
&+[-D^2\dot{\omega}_z + DR\omega_x^2 - D^2\omega_x\omega_y - D^2\omega_x\omega\Omega cos(\omega t) + R^2\dot{\omega}_z \\
&+(\omega_y + \omega\Omega cos(\omega t)(-R^2\omega_x + DR\omega_y + DR\omega\Omega cos(\omega t))]\hat{z}_g]
\end{aligned} \qquad \text{(B.13)}$$

$$\begin{aligned}
T_3 = m[&[R^2\dot{\omega}_x + DR\dot{\omega}_y + DR\dot{\omega}\Omega cos(\omega t) - DR\omega^2\Omega sin(\omega t) \\
&+DR\omega_x\omega_z + R^2\omega_y\omega_z + R^2\omega_z\omega\Omega cos(\omega t)]\hat{x}_g \\
&+[-RD\dot{\omega}_x - D^2\dot{\omega}_y - D^2\dot{\omega}\Omega cos(\omega t) + D^2\omega^2\Omega sin(\omega t)
\end{aligned}$$

$$-D^2\omega_x\omega_z - DR\omega_y\omega_z - DR\omega_z\omega\Omega cos(\omega t)]\hat{y}_g$$

$$+[-D^2\dot{\omega}_z - DR\omega_x^2 - D^2\omega_x\omega_y - D^2\omega_x\omega\Omega cos(\omega t) + R^2\dot{\omega}_z$$

$$+(\omega_y + \omega\Omega cos(\omega t)(-R^2\omega_x - DR\omega_y - DR\omega\Omega cos(\omega t))]\hat{z}_g] \quad \text{(B.14)}$$

$$T_4 = m[[R^2\dot{\omega}_x - DR\dot{\omega}_y - DR\dot{\omega}\Omega cos(\omega t) + DR\omega^2\Omega sin(\omega t)$$

$$-DR\omega_x\omega_z + R^2\omega_y\omega_z + R^2\omega_z\omega\Omega cos(\omega t)]\hat{x}_g$$

$$+[RD\dot{\omega}_x - D^2\dot{\omega}_y - D^2\dot{\omega}\Omega cos(\omega t) + D^2\omega^2\Omega sin(\omega t)$$

$$-D^2\omega_x\omega_z + DR\omega_y\omega_z + DR\omega_z\omega\Omega cos(\omega t)]\hat{y}_g$$

$$+[-D^2\dot{\omega}_z + DR\omega_x^2 - D^2\omega_x\omega_y - D^2\omega_x\omega\Omega cos(\omega t) + R^2\dot{\omega}_z$$

$$+(\omega_y + \omega\Omega cos(\omega t)(-R^2\omega_x + DR\omega_y + DR\omega\Omega cos(\omega t))]\hat{z}_g] \quad \text{(B.15)}$$

The total torque is the sum of the torques generated from each of the mass centers. The resulting net torque is given by Equation(B.16):

$$T = 4m[[R^2(\dot{\omega}_x + \omega_y\omega_z + \omega_z\omega\Omega cos(\omega t))]\hat{x}_g$$

$$+[D^2(-\dot{\omega}_y - \omega_x\omega_z - \dot{\omega}\Omega cos(\omega t) + \omega^2\Omega sin(\omega t))]\hat{y}_g$$

$$+[\dot{\omega}_z(R^2 - D^2) - D^2\omega_x\omega_y - D^2\omega_x\omega\Omega cos(\omega t)$$

$$-R^2\omega_x\omega_y - R^2\omega_x\omega\Omega cos(\omega t)]\hat{z}_g \quad \text{(B.16)}$$

The net torque simplifies to Equation (B.17); this is identical to the result derived in Chapter 3.

$$T = 4m[[R^2\omega_z\omega\Omega cos(\omega t)]\hat{x}_g$$

$$+[-D^2\dot{\omega}\Omega cos(\omega t) + D^2\omega^2\Omega sin(\omega t))]\hat{y}_g$$

$$+[-D^2\dot{\omega}_z + R^2\dot{\omega}_z]\hat{z}_g \qquad \text{(B.17)}$$

Appendix C. Ksys Matlab Script File

```
E=160e6;
rho=2330;
num_brace=4;
wfinger=2e-6;
scale=.3714;
lplate=50e-6;
wplate=100e-6;
sigr=input('residual stress of layer : ');
sigr=sigr*1e6;
thick=input('Layer Thickness in microns :');
thick=thick*1e-6;
wsup=input('Support Width in microns :');
wsup=wsup*1e-6;
lsup=input('Support Length in microns :');
lsup=lsup*1e-6;
lfing=input('Finger Length in microns :');
lfing=lfing*1e-6;
numfingers=input('Number of Fingers :');
k1=(wsup*thick)*sigr/lsup;
k2=(E*thick*(wsup)^3)/(lsup^3);
ksys=num_brace*(k1+k2);
Mp=wplate*lplate*thick*rho;
Mf=numfingers*(lfing*thick*wfinger);
M=Mp+Mf;
Msup=wsup*thick*lsup*rho;
Fr=(1/(2*pi))*(ksys/(M+scale*(Msup)))^.5;
file=fopen('freq','a');
fprintf(file,'Output for Tunning Fork Gyroscope \n');
fprintf(file,'Youngs modulus: %10.3e \n', E);
fprintf(file,'Rho used: %10.3e \n', rho);
fprintf(file,'number of braces: %10.3e \n', num_brace);
fprintf(file,'finger length: %10.3e \n', lfing);
fprintf(file,'Support length: %10.3e \n', lsup);
fprintf(file,'Support width: %10.3e \n', wsup);
fprintf(file,'Layer Thickness: %10.3e \n', thick);
fprintf(file,'scale factor for spring constants: %10.4e \n', scale);
fprintf(file,'k1          k2        ksys       Mp        Mf
        M        Msup      Fr \n');
fprintf(file,'%5.3e %5.3e %5.3e %5.3e %5.3e %5.3e %8.3e %5.3e\n\n\n\n'
       , k1,k2,ksys,Mp,Mf,M,Msup,Fr);
fclose('all');
```

Bibliography

1. L. Ristic, ed., *Sensor Technology and Devices*, Ch. 3: Bulk Micromachinig Technology. Artech House, 1984.
2. B. Bryzek, K. Petersen, and W. McCulley, "Micromachines on the march," *IEEE Spectrum*, pp. 20–31, May 1984.
3. D. Tazartes and J. Mark, "Integration of GPS receivers into existing inertial navigation systems," *NAVIGATION: Journal of the Institute of Navigation*, vol. 35, no. 1, pp. 105–118, Spring 1988.
4. D. Cox, "Integration of GPS with inertial navigation systems," *Global Positioning System: papers published in navigation*, vol. I, pp. 144–153, 1980.
5. D. Buechler and M. Foss, "Integration of GPS and strapdown inertial subsystems into a single unit," *NAVIGATION: Journal of the Institute of Navigation*, vol. 34, no. 2, pp. 140–159, Summer 1987.
6. R. Gray, "An integrated GPS/INS/BARO and radar altimeter system for aircraft precision approach landings," Master's thesis, School of Engineering, Air Force Institute of Technology (AU), 1994.
7. M. Putty and K. Najafi, "A micromachined vibrating ring gyroscope," in *Solid State Sensors and Actuators Workshop*, TFC INC., 1994, pp. 213–220.
8. J. Bernstein, "A micromachined comb-drive tuning fork gyroscope," in *Digest IEEE/ASME Micro ElectroMechanical Systems (MEMS) Workshop*, Ft. Lauderdale, FL, Feb. 1993, pp. 143–148.
9. A. Boxenhorn and P. Greiff, "A vibratory micromechanical gyroscope," in *AIAA Guidance, Navigation, and Control Conference*, Minneapolis, Minnesota, Aug. 1988, pp. 1033–1040. AIAA Rep. 88-4177.
10. M. Putty, *A Micromachined Vibrating Ring Gyroscope*. PhD thesis, Department of Electrical Engineering and Computer Schience, University of Michigan at Ann Arbor, Mar. 1995.
11. W. Stripling and J. Baskett, "Hemispherical resonator gyro: principle, design, and performance," in *AGARD Conference Proceedings 525 Integrated and Multi-Function Navigation*, Ottawa, Canada, May 1992, pp. 1–6.
12. A. Lawrence, *Modern Inertial Technology Navigation Guidance and Control*. New York: Springer-Verlag, 1993.
13. J. Burdess and T. Wren, "The theory of a piezoelectric disc gyroscope," *IEEE Transactions on Aerospace and Electronic Systems*, vol. AES-22 NO.4, pp. 410–418, Jul. 1986.
14. J. Scarborough, *The Gyroscope: Theory and Applications*. New York: Interscience Publishers, INC., 1958.
15. J. Lyman, "Gyrotron angular rate tachometer," *Aeronotical Engineering Review*, pp. 24–36, Nov. 1958.

16. T. Poth and J. Elwell, "Progress on micromechanical inertial guidance system," in *AIAA, Aerospace Design Conferance*, Irvine, California, Feb. 1992, pp. 1–7. AIAA Rep. 92-1119.

17. J. Elwell, "Progress on micromechanical inertial instruments," in *AIAA Guidance, Navigation, and Control Conference*, New Orleans, Louisiana, Aug. 1991, pp. 1482–1485. AIAA Rep. 91-2765.

18. J. Sitomer and J. Connelly, "Micromechanical inertial measurement units (MMIMU)," in *AIAA Guidance, Navigation, and Control Conference*, Monterey, California, Aug. 1993, pp. 1749–1752. AIAA Rep. 93-3799.

19. D. Wood, G. Cooper, J. Burdess, A. Harris, and J. Cruickshank, "A silicon membrane gyroscope with electrostatic actuation and sensing," in *Micromachined Devices and Components*, Austin, Texas, Oct. 1995, pp. 74–83. SPIE vol. 2642.

20. G. Bryan, "On a revolving cylinder or bell," *Proceedings of the Royal Society (London)*, vol. 47, 1890.

21. B. Korites, *Microsensors.* Kern Inc, 1987.

22. R. Pierret, *Semiconductor Fundamentals.* New York: Addison-Wesley, 1988.

23. S. Jacobsen, *JTEC Panel Report on Microelectro Mechanical Systems in Japan*, Ch. 6: Packaging, Assembly and Testing. Sep. 1994.

24. N. Swart and A. Nathan, "Reliability study of micro hotplates," in *Solid State Sensors and Actuators Workshop*, TFC INC., 1994, pp. 119–126.

25. L. Ristic, ed., *Sensor Technology and Devices*, Ch. 4: Surface Micromachinig Technology. Artech House, 1984.

26. A. Lee, P. Ljung, and A. Pisano, "Vibromotors," *IEEE Transactions on Micro Electro Mechanical Systems*, pp. 177–182, 1992.

27. W. Tang, T. Nguyen, and R. Howe, "Laterally driven polysilicon resonant microstructures," *Sensors and Actuators*, vol. 20, pp. 25–32, Aug. 1989.

28. MCNC, "Multi user mems process (mumps)," *North Carolina's Microelectronics, Computing and Networking Center*, 1994.

29. MCNC, "Mcnc world wide web page," *Located at: http://www.mcnc.org/HTML/ETD /MEMS/mems.html*, 1994.

30. R. Howe, A. Pisano, and B. Boser, *Monolithic Surface Micromachined Inertial Sensors Corse Notes.* San Francisco: UC Berkely, 1994.

31. P. Kundu, *Fluid Mechanics.* New York: Academic Press, INC., 1984.

32. P. Likins, *Elements of Engineering Mechanics.* New York: McGraw - Hill, 1973.

33. W. Young, *Roark's Formulas for Stress and Strain.* New York: McGraw-Hill, 1989.

34. M. Petyt, *Introduction to finite element vibration analysis.* Cambridge: Cambridge University Press, 1990.

35. H. Packard, *Operation Manual Model 4195A Network / Spectrum Analyzer.* Tokyo: Yokogawa-Hewlett-Packard, LTD., 1987.

36. D. Sene, "Design, fabrication and characterization of micro opto electro-mechanical systems," Master's thesis, School of Engineering, Air Force Institute of Technology (AU), To Be Published.

37. G. Fedder and K. Clark, "Modelling and simulation of microresonators with meander suspensions," in *Simulation and Design of Microsystems and Microstructures*, Boston, Massachusettes, Oct. 1995, pp. 175–183.

Vita

Lt Richard M. Kuhns [redacted] He graduated from Park High school in 1990 and entered undergraduate studies Purdue University in West Lafayette, Indiana. He graduated with a Bachelor of Science degree in Electrical Engineering in May of 1994. He received his commission on 13 May 1994. In May 1994 he entered the school of Electrical Engineering, Air Force Institute of Technology.

[redacted]

REPORT DOCUMENTATION PAGE

Form Approved
OMB No. 0704-0188

1. AGENCY USE ONLY *(Leave blank)*	2. REPORT DATE	3. REPORT TYPE AND DATES COVERED
	December 1995	Master's Thesis

4. TITLE AND SUBTITLE
DESIGN AND FABRICATION OF A MICROMECHANICAL GYROSCOPE

5. FUNDING NUMBERS

6. AUTHOR(S)
Richard M. Kuhns

7. PERFORMING ORGANIZATION NAME(S) AND ADDRESS(ES)
Air Force Institute of Technology, WPAFB OH 45433-6583

8. PERFORMING ORGANIZATION REPORT NUMBER
AFIT/GE/ENG/95D-10

9. SPONSORING / MONITORING AGENCY NAME(S) AND ADDRESS(ES)
Richard Strawser
WL/ELE
2185 Avionics Circle
Wright-Patterson AFB, OH 45433

10. SPONSORING / MONITORING AGENCY REPORT NUMBER

11. SUPPLEMENTARY NOTES

12a. DISTRIBUTION / AVAILABILITY STATEMENT
Approved for public release; distribution unlimited

12b. DISTRIBUTION CODE

13. ABSTRACT *(Maximum 200 words)*

Both size and cost of mechanical and optical inertial navigation systems (INS) have prevented their use in many applications. By developing a micromachined gyroscope and combining it with existing micromachined accelerometer designs to form a low sensitivity INS, the cost would be reduced by a factor of 10 or more. The lower per unit cost would open new areas for INS use. A second advantage of the micromachined INS would be its size. A micromachined INS would weigh only a few ounces and take significantly less space, allowing more room for electronics and the weight reduction would lead to longer mission times. In this thesis three micromachined gyroscopes were developed and fabricated: a micromachined comb-drive vibrating gyroscope, a planar gimballed gyroscope, and a vibrating ring gyroscope. The micromachined gyroscopes were fabricated using the Multi User MEMS (Micro Electro Mechanical Systems) Process (MUMPS). These devices were then tested in AFIT's microelectronics laboratories.

14. SUBJECT TERMS	15. NUMBER OF PAGES
...	147
	16. PRICE CODE

17. SECURITY CLASSIFICATION OF REPORT	18. SECURITY CLASSIFICATION OF THIS PAGE	19. SECURITY CLASSIFICATION OF ABSTRACT	20. LIMITATION OF ABSTRACT
UNCLASSIFIED	UNCLASSIFIED	UNCLASSIFIED	UL

GENERAL INSTRUCTIONS FOR COMPLETING SF 298

The Report Documentation Page (RDP) is used in announcing and cataloging reports. It is important that this information be consistent with the rest of the report, particularly the cover and title page. Instructions for filling in each block of the form follow. It is important to ***stay within the lines*** to meet ***optical scanning requirements.***

Block 1. Agency Use Only *(Leave blank)*.

Block 2. Report Date. Full publication date including day, month, and year, if available (e.g. 1 Jan 88). Must cite at least the year.

Block 3. Type of Report and Dates Covered. State whether report is interim, final, etc. If applicable, enter inclusive report dates (e.g. 10 Jun 87 - 30 Jun 88).

Block 4. Title and Subtitle. A title is taken from the part of the report that provides the most meaningful and complete information. When a report is prepared in more than one volume, repeat the primary title, add volume number, and include subtitle for the specific volume. On classified documents enter the title classification in parentheses.

Block 5. Funding Numbers. To include contract and grant numbers; may include program element number(s), project number(s), task number(s), and work unit number(s). Use the following labels:

C	- Contract	**PR**	- Project
G	- Grant	**TA**	- Task
PE	- Program Element	**WU**	- Work Unit Accession No.

Block 6. Author(s). Name(s) of person(s) responsible for writing the report, performing the research, or credited with the content of the report. If editor or compiler, this should follow the name(s).

Block 7. Performing Organization Name(s) and Address(es). Self-explanatory.

Block 8. Performing Organization Report Number. Enter the unique alphanumeric report number(s) assigned by the organization performing the report.

Block 9. Sponsoring/Monitoring Agency Name(s) and Address(es). Self-explanatory.

Block 10. Sponsoring/Monitoring Agency Report Number. *(If known)*

Block 11. Supplementary Notes. Enter information not included elsewhere such as: Prepared in cooperation with...; Trans. of...; To be published in.... When a report is revised, include a statement whether the new report supersedes or supplements the older report.

Block 12a. Distribution/Availability Statement. Denotes public availability or limitations. Cite any availability to the public. Enter additional limitations or special markings in all capitals (e.g. NOFORN, REL, ITAR).

- **DOD** - See DoDD 5230.24, "Distribution Statements on Technical Documents."
- **DOE** - See authorities.
- **NASA** - See Handbook NHB 2200.2.
- **NTIS** - Leave blank.

Block 12b. Distribution Code.

- **DOD** - Leave blank.
- **DOE** - Enter DOE distribution categories from the Standard Distribution for Unclassified Scientific and Technical Reports.
- **NASA** - Leave blank.
- **NTIS** - Leave blank.

Block 13. Abstract. Include a brief *(Maximum 200 words)* factual summary of the most significant information contained in the report.

Block 14. Subject Terms. Keywords or phrases identifying major subjects in the report.

Block 15. Number of Pages. Enter the total number of pages.

Block 16. Price Code. Enter appropriate price code *(NTIS only)*.

Blocks 17. - 19. Security Classifications. Self-explanatory. Enter U.S. Security Classification in accordance with U.S. Security Regulations (i.e., UNCLASSIFIED). If form contains classified information, stamp classification on the top and bottom of the page.

Block 20. Limitation of Abstract. This block must be completed to assign a limitation to the abstract. Enter either UL (unlimited) or SAR (same as report). An entry in this block is necessary if the abstract is to be limited. If blank, the abstract is assumed to be unlimited.